UNIVERSIDAD POLITÉCNICA DE VALENCIA

Instituto de Tecnología Química U.P.V.-C.S.I.C.

Inelastic Neutron Scattering study of Brønsted acidity in LTA zeolite

TESIS DOCTORAL

Presentada por:

Tetiana Lemishko

Dirigida por:

Dr. Germán Sastre Navarro

Dr. Mónica Jiménez-Ruiz

Valencia, Marzo 2019

UNIVERSIDAD POLITÉCNICA DE VALENCIA

Instituto de Tecnología Química U.P.V.-C.S.I.C.

Inelastic Neutron Scattering study of Brønsted acidity in LTA zeolite

TESIS DOCTORAL

Presentada por:

Tetiana Lemishko

Dirigida por:

Dr. Germán Sastre Navarro

Dr. Mónica Jiménez-Ruiz

Valencia, Marzo 2019

Preamble

This thesis was part of the PhD program of the Instituto de Tecnología Química (ITQ) U.P.V.-C.S.I.C. Universidad Politecnica de Valencia in Spain jointly with the Institut Laue-Langevin (ILL) in Grenoble, France. The work was supervised by by Dr. Mónica Jiménez-Ruiz at the ILL and Dr. Germán Sastre Navarro in ITQ.

Acknowledgements

I would like to thank to Institut Laue-Langevin and Consejo Superior de Investigaciones Científicas (CSIC) for funding this PhD thesis research).

Abstract

This thesis is dedicated to the study of acidity of LTA zeolites with Si/Al ratios 5 and 40 by using the technique of inelastic neutron scattering (INS) in combination with other techniques such as computational modeling and nuclear magnetic resonance (NMR) spectroscopy.

Zeolites are crystalline and microporous aluminosilicates which form one of the most important groups of functional materials. Zeolites are widely used as solid acid catalysts for the wide range of important processes regarding organic molecules. The most important are cracking, isomerization reaction and synthesis of hydrocarbons.

The catalytic properties of a zeolite depend strongly on its acidity, and this in turns depends on: the total number of acid sites, their individual strength, and their individual location. These three factors are strongly correlated. Geometric parameters that are defined by the location of the acid site (i.e., bond angles and lengths around the acid site) make a remarkable contribution to the acid strength.

There are several studies, found in literatures, typically done by Infrared (IR) or Nuclear magnetic resonance (NMR) technique and dedicated to acidity of zeolites. However, the hydrogen bending modes (200-1200 cm^{-1}), which are found to be more sensitive to local environment, cannot be observed by this technique, since these bands overlap with strong bands of the vibrations of zeolitic framework (300-1800 cm^{-1}).

INS technique used in this study allows to detect the bands of vibrations of hydrogen atoms in zeolites (including bending modes).

Moreover, this study shows that the combination of an extremely high quality of the samples and the sensitivity of the instrument allows to detect with high precision the

acid sites of both high-silica and low-silica zeolites and obtain information about their position. This in its turn gives us the possibility to obtain the aluminium location in zeolites. In order to fully understand the INS spectra we performed *ab-initio* calculations that allow to interpret the experimental bands and choose a structural model that reproduces the probable location of acid sites in the sample.

Resumen

En esta tesis se realiza un estudio de acidez de zeolita LTA con la relación Si/Al 5 y 40 utilizando la técnica de dispersión inelástica de neutrones (INS) en combinación con otras tecnicas como la modelización computacional y la espectroscopía de resonancia magnética nuclear (RMN).

Las zeolitas son aluminosilicatos altamente cristalinos que forman parte de un grupo importante de los materiales funcionales. Las zeolitas son extremadamente útiles como catalizadores para muchas reacciones importantes con moléculas orgánicas. Las más importantes son craqueo, isomerización y síntesis de hidrocarburos.

Las propiedades catalíticas de una zeolita dependen principalmente de su acidez y ésta depende de tres factores: el número totál de los sitios ácidos, sus fuerzas individuales y su localización individual, estando estos tres factores relacionados. Los parámetros geométricos definidos por localización de los sitios ácidos (es decir, la longitud y los ángulos de enlaces entre los átomos alrededor del sitio ácido) contribuyen de una manera importante a la fuerza ácida.

En la literatura hay muchos trabajos de estudios de acidez en zeolita utilizando la espectrometría infrarroja (IR), sin embargo, con esta técnica es imposible medir las vibraciones de flexión (bending modes, 200-1200 cm^{-1}), las bandas más sensibles al entorno local de los centros ácidos, ya que estas bandas se superponen con las bandas de vibración de la red de zeolite (300-1800 cm^{-1}).

En esta tesis se realiza un estudio de acidez utilizando la tecnica de INS, que nos permite medir principalmente los modos de vibración de los átomos de H y también nos permite medir todas las bandas de vibración (incluido el bending).

Este estudio muestra que la combinación de la alta calidad de las muestras y la sensibilidad del instrumento utilizado permite detectar con alta precisión los sitios ácidos y obtener la información sobre su posición que a su vez nos perimte obtener la posición de los átomos de Al. Con el fin de interpretar los espectros INS se ha realizado un estudio computacional (cálculos ab-initio) con el objetivo de comparar los espectros cálculados con los resultados experimentales y definir el modelo que reproduce la posición mas probable de los centros ácidos en la muestra.

Resum

En aquesta tesi es realitza un estudi d'acidesa de zeolita LTA amb la relació Si / Al 5 i 40 utilitzant la tècnica de dispersió inelastica de neutrons (INS) en combinació d'altres tècniques com la modelització computacional i la espectroscòpia de ressonància magnètica nuclear (RMN).

Les zeolites són aluminosilicats altament cristal·lins que formen part d'un grup important dels materials funcionals. Les zeolites són extremadament útils com a catalitzadors per a moltes reaccions importants amb molècules orgàniques. Les més importants són craqueig, isomerització i síntesi d'hidrocarburs.

Les propietats catalítiques d'una zeolita depenen principalment de la seva acidesa i aquesta depèn de tres factors: el nombre total dels llocs àcids, les seves forces individuals i la seva localització individual, estant aquests tres factors relacionats. Els paràmetres geomètrics definits per localització dels llocs àcids (és a dir, la longitud i els angles d'enllaços entre els àtoms al voltant del lloc àcid) contribueixen d'una manera important a la força àcida.

En literatura hi ha molts treballs d'estudis d'acidesa en zeolita utilitzant l'espectrometria infraroja (IR), però és impossible mesurar les vibracions de flexió (bending modes, 200-1200 cm^{-1}) amb aquesta tècnica ja que aquestes bandes es superposen amb les bandes de vibració de la xarxa de zeolita (300-1800 cm^{-1}).

La tècnica de dispersió inelastica de neutrons (Inelastic neutron scattering) ha estat utilitzada per estudiar l'acidesa de la zeolita LTA amb diferents relacions Si / Al (per tant diferents c.ontinguts de H en la zeolita).

En aquesta tesi es realitza un estudi d'acidesa utilitzant la tècnica de INS, que ens permet mesurar principalment els modes de vibració dels àtoms d'H i també ens permet mesurar totes les bandes de vibració (inclòs el bending).

Aquest estudi mostra que la combinació de l'alta qualitat de les mostres i la sensibilitat del instrument utilitzat permet detectar amb alta precisió els llocs àcids i obtenir la informació sobre la seva posició que en el seu lloc ens perimte obtenir la posició d'Al. Per tal de interpretar els espectres INS s'ha realitzat un estudi computacional (càlculs ab-initio) amb la comparació dels espectres calculats amb els resultats experimentals.

Contents

Chapter 1. Introduction……..……...17

1.1 Zeolites: history, variety, structure, properties…...……...17
1.2 Applications of zeolites..……...…….22
1.3 Acidity ……...……25
1.3.1 Brønsted acidity in zeolites…….……25
1.3.2 Location of Brønsted acid sites. Distribution of aluminium and hydrogen atoms. Characterization methods…….……26
1.3.3 Acidity strengths of Brønsted acid sites. Characterization methods……....33

1.4 Why should we use neutrons to measure Brønsted acidity in zeolites?……39

Chapter 2. Methods and materials…….....47

2.1 Introduction to neutron scattering ……..47
2.1.1 Properties of neutron ……...47
2.1.2 Basis of neutron scattering ……50
2.1.3 Coherent and incoherent scattering ……54
2.1.4 Energy and momentum conservation laws …….....57
2.1.5 Inelastic neutron scattering ……60
2.1.5.1 Kinematic range of INS instruments. Spectrometers with direct and indirect geometry.……60
2.1.5.2 IN1-Lagrange instrument.……62
2.1.5.3 Incoherent approximation……65
2.1.5.4 Scattering law……66
2.1.5.5 INS spectrum……67
2.2 Computational methods…….....71
2.2.1 Normal modes analysis of molecular vibrations …….....71
2.2.2 Schrödinger equation ……...74
2.2.3 Basic theorem and equation in Density Functional Theory …76
2.2.4 Exchange-correlation functionals ……....78
2.2.5 DFT codes ……...81
2.2.6 Selection of calculation parameters ……83

2.2.7 Mantid and aCLIMAX software ……84
2.3 Nuclear Magnetic Resonance Spectroscopy ……..86
2.3.1 Basic principles of NMR ……86
2.3.2 Magic Angle Spinning ……....90
2.3.3 Cross polarization (CP) method ……....90
2.3.4 NMR in study of zeolites ……..…...91
2.3.5 Experimental details of NMR experiments ……....94
2.4 Preparation of samples ……...……94
2.4.1 Synthesis of LTA-40 ……..……..95
2.4.2 Synthesis of LTA-5 ……..…97

Chapter 3. Inelastic Neutron Scattering Study on the Location of Brønsted Acid Sites in High Silica LTA Zeolite……...99

3.1 Computational models of LTA-40 …….....101
3.2 Comparison between experimental INS and theoretical DFT results……103
3.3 Frequency analysis of the vibrational bands ……..…105
3.4 Multiphonon analysis ……..…….....107
3.5 Periodic DFT energies ……...……..110
3.6 ^{29}Si NMR and Infrared characterization of high silica LTA (LTA-40) ….....112
3.7 Comparison of the calculated OH-stretching frequencies with experimental Infrared results …….…….....114
3.8 Additional CASTEP/PBEsol study of possible crystallographic positions of the acid sites LTA-40 ……..……...116
3.9 Conclusions to the Inelastic Neutron Scattering Study on the Location of Brønsted Acid Sites in High Silica LTA Zeolite …….....119

Chapter 4. Inelastic Neutron Scattering Study of the Aluminum and Brønsted Site Location in Aluminosilicate LTA Zeolites……....121

4.1 ^{29}Si MAS NMR Characterization of LTA-5 ……...…….123
4.2 Computational models of Al/H distributions in LTA-5 ……..126
4.3 Comparison between experimental INS and theoretical DFT results ……...134

4.4 Multiphonon analysis ……..……140
4.5 Frequency analysis of the vibrational bands in stable Al distribution of LTA-5…….....143
4.6 Analysis of the Al and H distributions in models d1-d9 of LTA-5……..144
4.6.1 Aluminium in double-four rings ……144
4.6.2 Proton content of 8T-rings ……145
4.6.3 Aluminum content of 6T-rings …….……....146
4.6.4 Al-Al and H-H close distance…….147
4.7 Mathematical comparison of experimental and calculated INS spectra 149
4.8 Is the calculated INS spectrum method-dependent? CASTEP vs. DMol3……...152
4.9 Conclusions to the Inelastic Neutron Scattering Study of the Aluminum and Brønsted Site Location in Aluminosilicate LTA Zeolites ……161
Chapter 5. General conclusions……163
Bibliography……167

Chapter 1
Introduction

1.1 Zeolites: history, variety, structure, properties

Zeolites are microporous aluminosilicates with similar structural features and properties which form a large important group of functional materials.

The study of zeolites has been of a great interest for scientist for more than 200 years. The term ‘zeolite’ first was introduces in 1756 by Swedish mineralogist and chemist Axel Fredrik Crondstedt [1, 2] after he observed that while heating a natural solid zeolite mineral, the bubbles and steam have been emitted. Cronstedt combined the Greek words ‘*zeo*’ (to boil) and ‘*lithos*’ (rock) to form the word ‘zeolite’. After Cronstedt’s discovery was made, natural zeolites have been the only samples available for study for most of the two centuries. Moreover, natural zeolites, at the time, were considered as rare minerals, found mostly as large isolated crystals in basaltic rocks, but never in large deposits of relatively pure materials.

The structure of zeolites, like for most of the silicates is based on TO_4 tetrahedra, where T is either aluminium or silicon atom. The neighboring tetrahedra are connected between each other via oxygen atoms in such a way that all of their corners are shared, this results in low density microporous materials with broad 3-dimensional networks. Depending on the number of T atoms, there can be formed T-membered rings of different size in the

framework of zeolite. These rings usually contain from 4 to 16 T atoms. In T-membered rings the T atom of the TO_4 tetrahedron is located at each of the corners, and the oxygens are located towards the mid-points of the lines joining each T atom.

Furthermore, a TO_4 unit may develop in three different structural variations [3]: single unit structure (a), chain like structures (b), sheet like structures (c) and framework structures (d) (see **Figure 1**).

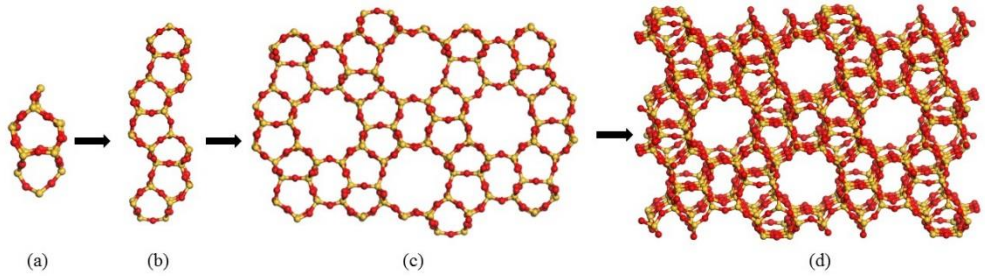

Figure 1. The structure of ZSM-5 (FMI) zeolite built up by: (a) single unit; (b) chains of interlinked single units; (c) layers of these chains; and d) framework unit cell

The framework of zeolites is represented as the three-dimensional network containing pores, channels and cavities of molecular dimensions. For instance, according to the size of their pores, which can be estimated by the number of Si or Al atoms in the ring, zeolites can be divided in several groups (see **Figure 2**). The structure of first type of zeolites contains rings that are formed by no more than 8 Si or Al atoms, which diameter is around 3.5 ÷ 4.5 Å, such as LTA zeolite. Zeolites that contain 10-ring with a diameter of 4.5 ÷ 6.0 Å belong to the second group, such as FMI zeolite. And finally, those with 12-ring with a diameter of 6.0 ÷ 8.0 Å, like faujasite, belong to the third type of zeolites.

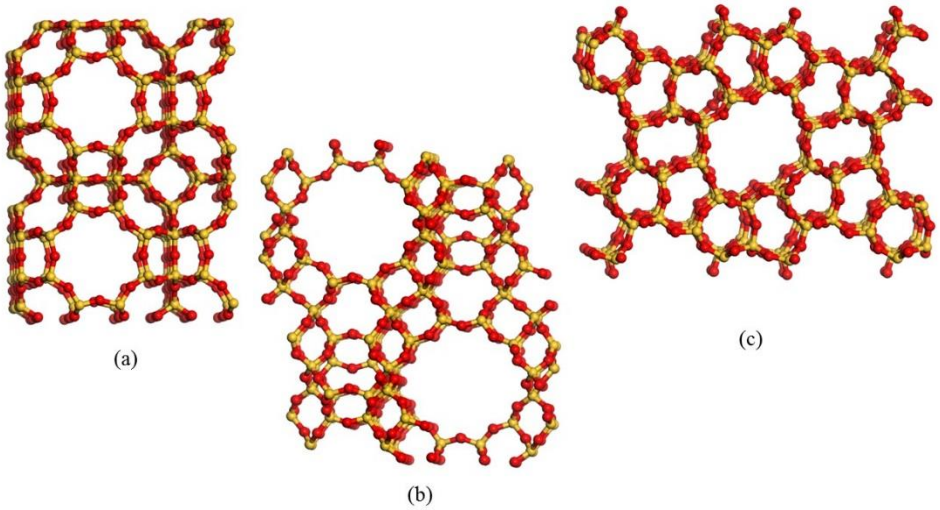

Figure 2. The frameworks of (a) LTA; (b) FMI; (c) faujasite zeolites

Besides, the framework type of zeolite is defined by the way of how the primary building tetrahedra are connected in the framework. In order to simplify the identification of zeolites it has been proposed by the Structure Commission of the International Zeolite Association (IZA-CS) [4] to classify zeolites by framework type and assign each of them to its specific 'structure code' (as of December 2017, 236 unique zeolite frameworks have been identified, and over 40 naturally occurring zeolite frameworks are known), such as, for example, LTA, MFI, FAU, MOR etc.

The first synthesis of zeolite was done by Henry Etienne Sainte-Claire Deville, who synthesized levynite in 1862 [5]. Due to their adsorption and ion-exchange properties zeolites can be used to soften water in application for which they are used to this day since 1905 [6] when Robert Gans first used zeolites to soften water on a commercial scale. Then, the Permutit-Filter company launched the first synthetic zeolites on the

American market as water softeners with an effectiveness greater than that of natural zeolites [7].

Until mid-1950s a commercial use of zeolites had been in adsorption and separation applications such as the removal of water from natural gas, refrigerants, and of hydrocarbons streams. In consequence zeolites found their application as acid catalysts.

As it was already mentioned above, zeolites can be found in nature or synthesized. Zeolites in nature are usually formed as crystals in small cavities of basaltic rocks over the years or as volcanic tuffs. These natural zeolites are formed in different geological environments such as alkaline deserts, lake sediments, ash ponds and marine sediments at relatively low temperature, under natural conditions. They also get crystallized in geologically young metamorphic rocks in mountainous regions. The most general formula of natural zeolites is [8]:

$$(Li, Na, K)_x\ (Mg, Ca, Sr, Ba)_y\ [Al_{(x+2y)}Si_{n-(x+2y)}O_{2n}) \cdot mH_2O,$$

where, x is the number of monovalent cations, y is the number of divalent cations, n is the half of the number of oxygen atom and m is the number of crystalized water molecules. Natural zeolites such as clinoptilolite and chabazite have applications in various fields such as water treatment and fertilizer application for soils.

Synthetic zeolites can be obtained by a chemical processes, resulting in more uniform and purer state as compared to the natural zeolites in terms of their lattice structures, sizes of pores and cages in their frameworks. The reactants used in synthesis of zeolites can be pure chemicals in silica and alumina, natural minerals or industrial chemical compounds.

The type of formed zeolite depends on several conditions of synthesis such as temperature, pressure, concentration of the reagent solutions, pH, SiO_2 and Al_2O_3 contents of the reactants. Depending on the Si/Al ratio there can be produced the following types of zeolites [9]: 'low silica zeolites' (with Si/Al ≤ 2) such as sodalite, 'intermediate silica zeolites' (with Si/Al = 2÷5) such as chabazite, faujasite and mordenite and 'high silica zeolites' (with Si/Al > 5) such as ZSM-5. The increase of Si/Al ratio significantly modifies the properties of zeolite such as acidity, resistivity, hydrophobicity, etc.).

Zeolites usually gain cations (Na^+, K^+, and NH_4^+) during the synthesis process or by interaction with the surrounding medium as a result of their ion exchange or adsorption characteristics. In fact, the cations are accommodated to balance the negative charge occurring on the surface of pores in zeolites. This can be attributed to the replacement of silicon atom by aluminium atom in some of the SiO_4^{4-} tetrahedra and its conversion into the AlO_4^{5-} tetrahedron which is linked to other SiO_4^{4-} .

The heavy metal cations such as Rb, Cs, Ag, Cd, Pb, Zn, Ba, Sr, Cu, Hg, Co and Cr have affinity towards zeolites, although, their exchange selectivity by the zeolites depends on the hydrated molecular size of the cations, their concentration in the reactants and Si/Al ratio of zeolite [10].

The application of zeolites follows from both: their specific structure and properties.

1.2 Applications of zeolites

Nowadays, zeolites are widely used in a variety of different fields and uses of zeolites derive from their specific properties. In the late 1930's Richard M. Barrer initiated the research on the synthesis and adsorption properties of zeolites and patented the use of zeolites in the fractionation of the mixture of hydrocarbons in 1942 [11, 12], revealing that the pore of zeolites of the certain size would adsorb molecules of an appropriate size, but exclude the molecules of other size. Then, following the findings of Barrer the researchers at Union Carbide (one of the biggest worldwide known chemical companies) developed procedures for preparation of the first synthetic zeolites (e. g. zeolites A, X and Y) that would find the industrial application [13].

Overall, zeolites are used to adsorb a variety of materials. The porous structure of zeolites can be used to "sieve" molecules having certain dimensions and allow them to enter the pores. As a result, Margeta et al. showed that natural zeolites can be efficiently used in water treatment [14]. Furthermore, due to their specific properties, zeolites are also able to adsorb and separate gases, this can be used for industrial applications. The most common gases that can be adsorbed by zeolites are CO (carbon monoxide), CO_2 (carbon dioxide), SO_2 (sulfur dioxide), H_2S (hydrogen sulfide), NH_3 (ammonia), Ar, O_2, N_2, H_2O, He, H_2, Kr, Xe, etc [15]. Jia and Murad used the method of molecular dynamics to examine gas separation efficiency of three zeolite membranes: Faujasite, MFI and Chabazite [16].

Hydrated cations within the zeolite pores are bound loosely to the zeolite framework, and can readily exchange with other cations in aqueous media. Applications of this can be seen in water softening devices [17], and the use of zeolites in detergents and soaps [18]. It is also known that more than 500 000 tons of zeolites were dumped via helicopter on the damaged reactor of Chernobyl nuclear power plant in order to absorb radioactive isotopes that were released during the disaster. In addition to that, zeolites were used to help keep radioactive ions out of milk, and also zeolites were baked into cookies and biscuits (for children) and encapsulated into pills (for adults) to help minimize the contamination in humans affected by the disaster [19]. Since then, zeolites have been integrated into use at other nuclear plants, for instance, they have been used in order to adsorb radioactive cesium that was released as a result of the 2011 Fukushima nuclear disaster [20].

Zeolites have been used in agriculture for soil treatment for the last decades. Thus, natural zeolites are used extensively in Japan as amendments for sandy, clay-poor soils. In addition to this, zeolites are also used in medicine. For instance, it has been found, that natural zeolite phillipsite and certain synthetic zeolites can be used as filters to remove NH_4^+ from the dialysate of kidney patients during hemodialysis [19].

Nowadays the main field of application of zeolites is catalysis. Due to its role in many important industrial chemical processes, catalysis became one of the key elements of our industrialized society and thus it has a direct impact on the global economy. As a result of their high surface area, zeolites contain a high density of the active sites (in the most of the cases those are Brønsted acid sites) that are directly involved in the reaction at the molecular level. These characteristics result in a high catalytic activity and thus effectivity of zeolites in catalytic processes.

Thus, zeolites are extremely useful as catalysts for several important reactions involving organic molecules, which are cracking [21], isomerization [22] and hydrocarbon

synthesis [23]. Sharikova et al. [21] have studied the mechanism of catalytic cracking of hydrocarbons on zeolites and metal-zeolite catalysts. It has been shown that the addition to zeolite catalyst the metals of VIII group of Periodic table increases its cracking activity while it doesn't change the activity in hydrogen re-distribution. Another study has been done in order to investigate the role of zeolites as catalysts in hydrocracking [24]. The process of hydrocracking of heavy gasoil, vacuum gasoil and gasoil from coke is performed in order to convert the heavier fractions into mixtures of hydrocarbons of lesser number of carbons for their consumption as transportation fuels. Beecher et al. [22] studied the isomerization of hexane on mordenite zeolite. Within this study the isomerizing properties of synthetic mordenite have been characterized, and a kinetic model of hexane isomerization was developed from the resulting data. Furthermore, it has been shown the possibility of application of zeolite catalyst for conversion of CO_2 into gasoline fuel [23].

Zeolites can also promote a diverse range of catalytic reactions including acid-base metal induced reactions [25].

Moreover, in chemical industry the examples of zeolite-catalyzed processes that are currently in use include hydroxylation (e. g. production of phenol, known as the precursor to many materials and useful compounds) [26], alkylation (e.g. production of ethylbenzene which is important compound in the petrochemical industry as an intermediate in the production of styrene, the precursor to polystyrene, a common plastic material) [27], oximation (e. g. production of cyclohexanone oxime, which in consequence is widely used as an intermediate chain in production the widely used polymers) [28] and epoxidation (e.g. propylene oxide, which major application is its use for the production of polyether polyols for use in making polyurethane plastics) [29], etc.

1.3 Acidity

1.3.1 Brønsted acidity in zeolites

According to the theory of Brønsted and Lowry, which describes acid-base interactions in terms of proton transfer between chemical species, acid is defined as a substance that can donate a proton H^+. Brønsted acid sites are observed in zeolites. A silicon atom in zeolite framework can be substituted by an aluminium atom, in this case a hydrogen atoms should be added in order to compensate an occurring negative charge of the system, forming acid site.

Thus, the Brønsted acidic site consists of a hydrogen atom bonded to the oxygen atom that connects the tetrahedrally coordinated cations, which form the zeolitic framework.

Protons can be incorporated into the framework of zeolite by different ways:

1) ion exchange in acid medium if the zeolite is stable under these conditions, in this conditions only high silica zeolite can be formed;
2) exchange with ammonium ions forming Brønsted acid site in zeolite framework and amonia : $Z^- + NH_4^+ \rightarrow Z\text{-}H + NH_3$;
3) dehydration of multivalent cation exchanged zeolites including hydrolysis of the cations (for example: $M_{x/n}(Al\ O_2)_x \times (Si\ O_2)_y \times\ zH_2O \rightarrow H_x(Al\ O_2)_x \times (Si\ O_2)_y \times\ (z\text{-}n)\ H_2O + M(OH)_n$, where M is cation, n is its valence, x and y are the numbers of Al and Si atoms in the zeolitic framework correspondingly, x is a number of crystalized water molecules.

Acidity of zeolites depends not only on the total number of the acid sites, but it also depends on their individual location and strengths. These 3 factors are strongly correlated. Characterization of acidity of zeolites is a major field of investigation of zeolites due to the fact that catalytic activity of zeolites is defined by their acidity. There is a large number of different methods that have been applied in studies of acidity of zeolites for the last several decades. Those characterization methods are mainly dedicated to description of either location of acids sites or their strengths.

1.3.2 Location of Brønsted acid sites. Distribution of aluminium and hydrogen atoms. Characterization methods

The location of the acid sites can be defined by distribution of either hydrogen or aluminium atoms in the framework of zeolite. In low-silica zeolites in which the content of aluminium atoms is high, the distribution of hydrogen atoms is mainly defined by the location of a corresponding aluminium atom. The distribution of aluminium atoms over the framework of zeolite in turns obeys the Lowensteins rule, according to which **Al-O-Al** linkages in zeolitic frameworks are forbidden. As a result, all aluminate tetrahedra must be linked to four silicate tetrahedral.

The factors that have mayor influence on the acidity of a given acid site are usually the chemical environment (presence of other neighboring acid sites) and crystallographic type of oxygen (depending on the zeolite topology) to which the proton is attached. Thus there is a number of techniques that can be used to define the location of the acid sites.

The correlation between OH-stretching vibrations and the size of the cavities in which these OH groups are placed was found by Jacobs and Mortier [30] by using Infrared (IR) technique. The vibrational frequencies were measured for OH groups placed in the cavities of different sizes: either formed by the ring larger than eight-membered ring (in this case OH group are unperturbed by electron cloud of other atoms in the cavity) or in

the cavities formed by 6- or 8-membered rings (in this case the vibrational movement of a H atoms is affected by presence of other atoms in the cavity). It has been found different O-H stretching frequencies of acid sites depending on the size of the cavity (see **Table 1**).

By analyzing the data presented in Table 1, it has been possible to define the general correlation between the IR data and location of the acid sites. There have been observed two frequencies attributed to two different O-H stretching vibrations: one found at 3650 cm^{-1} that corresponds to the hydrogen atoms in large cavities and another at 3550 cm^{-1}, attributed to the hydrogen atoms vibrating in small cavities. The disadvantage of this method is that it only distinguishes acid sites that are located in the cavities of particular size, and it can't be applicable as a general method (for instance, it doesn't work for the frameworks that don't contain cavities larger than those formed by eight ring). Furthermore, this method doesn't give the exact location and so local environment of the acid sites.

Table 1. Hydroxyl stretching frequencies in hydrogen-zeolites and their assignment

Zeolite	OH frequency (cm^{-1})	Assignment
FAU	3659	O_1-H in supercages
	3584	O_3-H in sodalite cages (6-membered ring)
HEU	3620	Crystal terminating, influenced by sample composition
	3560	In 8-membered rings (pores)
CHA	3630	8-membered ring
	3540	6-membered ring
STI	3650	Amorphous phase with STI composition
	3620	Crystal terminating, influenced by sample composition
	3575	8-membered rings
ERI	3612	8-membered rings
	3563	6-membered rings
MOR	3720	SiOH of unidentified nature
	3650	Occluded impurities
	3610	In pores
MFI	3720	Extra-lattice Si-OH
	3601	In pore intersections
MEL	3720	Extra-lattice Si-OH
	3605	In pore intersections
MAZ	3624	In pores
LTL	3630	In pores
FER	3612	In pores (10-membered rings)
OFF	3618	In pores
RHO	3612	In pores (8-membered rings)

taken from [30]

Sastre et al. [31] tested the correlation between the size of the cavity where the acid site is placed and the frequency of its OH stretching vibration by means of computational chemistry. The results are shown in **Figure 3**, where '∇' and 'Δ' correspond to the results obtained for SAPO-17 and offretite correspondingly, which are distinguished from those marked as 'O' and corresponding to other aluminosilicates and aluminophosphates (which include: SSZ-13, SSZ-24, faujasite, mordenite, erionite, OFF, SAPO-5, SAPO-

34, SAPO-37, SAPO-18, SAPO-35). It has been shown that the cavity size alone cannot be responsible for the relative position of the value of the stretching frequency as wide range of the OH stretching vibrational frequencies found to be attributed to the OH groups placed in the similar-sized cavities (see **Figure 3.**), which is in contrast of findings of Jacobs and Mortier.

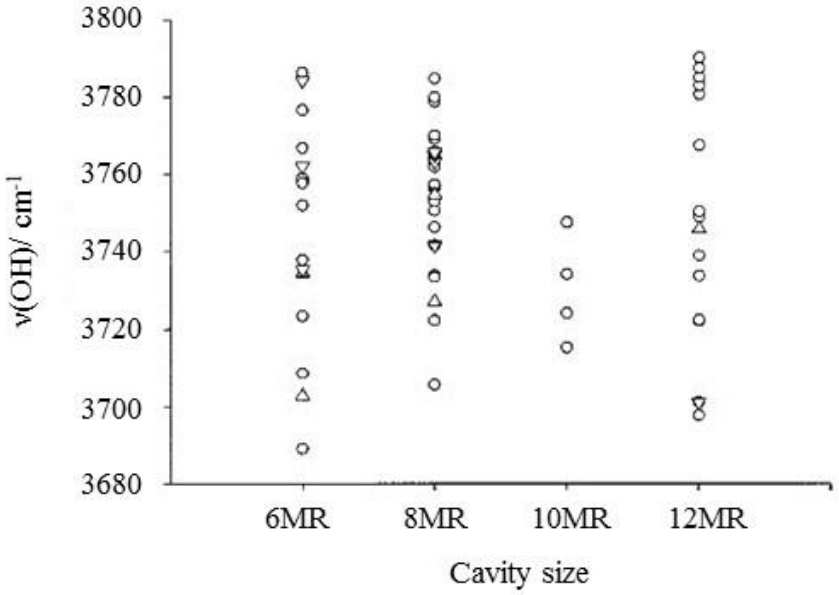

taken from [31]

Figure 3. Calculated vibrational frequencies and cavity size (MR is defined as member ring) for isolated Brønsted acid sites. All data are presented as open circles whilst highlighted are the values for alluminosilicate SAPO-17 (Δ) and offretite (∇) which clearly show that cavity size alone cannot account for the relative position of n(O–H)

Moreover, another study was done, using the same approach on X and Y zeolites [32]. It has been shown, that the band found at 3650 cm^{-1} is assigned to the stretching of the

hydrogen atoms located at large cavities and it is bonded to O1 crystallographic type of oxygen while the band at 3550 cm^{-1} is attributed to the vibrations of hydrogen atoms located at small cavities and this hydrogens can be attached to either O2, O3, or O4. This study revealed that even though it is possible to predict the crystallographic position of the hydrogens placed in a big cavities, it cannot be done for the hydrogen atoms placed in a big cavities. Hence, this approach cannot be considered as a general procedure of finding the exact position of the acid sites in the framework.

Different spectroscopic parameters can be also calculated by means of computational chemistry in order to define location of the acids sites. For instance, the influence of aluminium content and framework structure on the acidity in faujasite zeolite has been studied by Sauer et al. [33]. Within this study several characteristic parameters have been calculated such as deprotonation energies, O−H stretching vibrational frequencies, and ^{1}H NMR chemical shifts. It was shown that, deprotonation energy depends on the number of Al atoms in the neighboring coordination sphere of each Si atom, while ^{1}H NMR chemical shifts and vibrational frequencies of O-H stretching vibrations depend on the crystallographic position of the acid sites (O1H vs. O3H location). This study does not deal with acidity itself, but rather with the possibility to establish a general procedure to determine proton locations and so the acidity in zeolites.

Furthermore, the solid state ^{1}H MAS NMR (magic angle spinning nuclear magnetic resonance) spectroscopy also allows to distinguish acid sites located in the cavities of different size [34]. The spectrum of H-Y zeolite gives two chemical shifts that correspond to two different types of hydrogen atoms. One type represents the hydrogen atoms that are pointing into the large cavities, another type of hydrogen atoms includes those that are pointing into 6T-rings. In addition, it has been calculated the relative ratio of this two different types OH groups present in investigated zeolite by analyzing the relative areas of the corresponding peaks. Thus, by using this method, it is possible to obtain the information similar to those presented by IR.

In contrast to the case of zeolites with high Si/Al ratio where aluminium atoms are far from each other and hence the neighbors of silicon atom are only Si (4 Si) or Si (3 Si and 1 Al), in the case of low silica zeolites the main factor that defines acidy is a distribution of aluminium atoms, which in turn subsequently defines the possible locations of the acid sites in the framework. Nowadays, the main technique that is used to define the distribution of aluminium atoms in zeolitic frameworks is ^{29}Si MAS NMR technique. One of the essential studies was performed by Lippmaa and Engelhardt [35]. In this work results of high-resolution ^{29}Si NMR studies of synthetic zeolites A, X, Y and of a series of natural zeolite minerals with different structures and Si/Al ratios revealed that generally the ^{29}Si NMR spectra of simple zeolites may show a maximum of 5 peaks with a good resolution that correspond to the five different types of silicon atoms presented in the framework of a zeolite.

Figure 4. Schematic representation of the Si atoms in the framework of zeolite which are bonded to 4 other T atoms (Si or

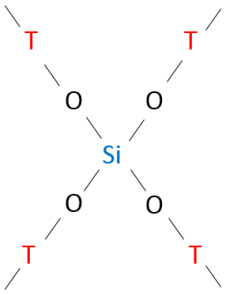

If we imagine every silicon atoms in the framework of zeolite as the one presented in **Figure 4**, the first type indicated as Q_0 would correspond to the silicon atom that contains 4 aluminum and 0 Si atoms in its neighboring coordination sphere, Q_1 indicates the silicon atom bonded to 1 silicon and 3 aluminum atoms, and then up to Q_4 corresponding to the silicon atom with 0 aluminum atoms in its neighboring sphere. The range of the chemical shifts at which these 5 peaks corresponding to 5 different types of Si atoms is presented by **Figure 5**.

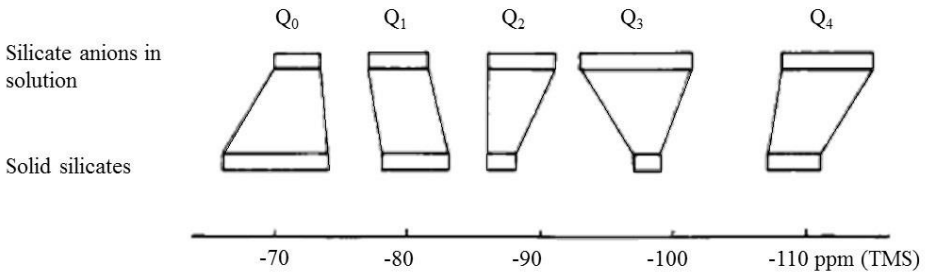

taken from [35]

Figure 5. Ranges of ^{29}Si NMR chemical shifts of different structural units of silicate anions in solid silicates and silicate solutions, where TMS is thetramethylsilan, which signal is attributed to 0 ppm

Therefore, with this type of analysis it is possible to describe the local environment of each silicon atom in further combination with the numerical methods or computational modeling, and it is possible to provide rough representation of the distribution of aluminium atoms in the framework of zeolites.

For instance, ^{29}Si NMR data obtained for H-ZSM zeolite showed that silicon atoms can be almost randomly substituted by aluminium atoms and this means that there is no clear information about the distribution of Al atoms in H-ZSM zeolite. Furthermore, it has been shown that ^{29}Si NMR spectra can be used to describe the Si/Al distribution in simple zeolitic framework such as faujasite, it has been proposed a possible scheme of arrangement of aluminium atoms over the framework of zeolite, however it was mentioned that other ordering schemes can also fit the obtained NMR data [36].

Thus, despite all the information that can be obtained with NMR spectroscopy, this technique does not allow to fully define the distribution of aluminum atoms in zeolitic crystals.

The acidity of zeolites not only depends on the location of the acid sites, but also geometric parameters such as TOT angles and bond lengths make a remarkable contribution to the acid strength. Hence, a computational study of Sastre et al. on Brønsted acidity of faujasite zeolite has been performed in order to detect the correlation between the structural parameters that define the location of the acid sites with their OH-stretching frequencies [37]. The calculated O-H stretching vibrational frequencies have been compared with experimental IR data obtained for commercial samples of faujasite. In this study no correlation has been found between the O-H stretching frequency of a given acid site with such other parameters that define the location of the acid sites as SiO(H)Al angle, AlO distance, oxygen type, or aluminum distribution.

On top of that, O'Malley et al. have done a theoretical study using *ab initio* molecular orbital calculations to monitor the effect of the increasing of SiOAl angle of the acid site on the acidic properties of this particular acid site [38]. It has been shown that the increasing of SiOAl angle gives rise to the decrease in the frequency of OH stretching vibration which means that ionicity of OH bond is decreased. The decrease in ionicity of OH bond in its turn indicates that increasing of the SiOAl angle causes the decrease in acidity. Nevertheless, this method can be used as a complementary to other methods, as the obtained information is not able to fully describe the location of the acid site.

1.3.3 Acid strengths of Brønsted acid sites. Characterization methods

The strengths of the Brønsted acid sites is one of the main factors that determines the catalytic activity of zeolites, therefore, it is of a great importance to have a reliable method to measure relative acidity, which would help to increase the understanding and

optimize the performance of zeolites as catalysts. Quantifying the strength of solid acids can be a difficult task to perform.

Titration in aqueous medium was commonly used in early studies in order to measure the acid strengths of zeolites [39], nevertheless, this approach was not useful due to the fact that acidity of zeolites changes in presence of water. However, titration can provide very useful information of the acidity on the surface in non-aqueous solutions [40].

Nowadays the titration method is rarely used to define the acid strengths of zeolite due to the fact that there are a number of limitations that occur while investigating the reaction $HX + Ind \leftrightarrow IndH^+ + X^-$, being one of them the inaccuracy of visual determination of the color change of the indicator. Apart from that there is a limited choice of indicators that may access the acid sites.

Temperature programmed desorption (TPD) of base molecules is more progressive method of measuring the strengths of acid sites in zeolites. It is based on the fact that different molecules may desorb from the zeolitic surface when the temperature is increased. Desorption occurs easier and so at lower temperatures on weaker acid sites. Thus, the relative acid strengths can be estimated using the heat of adsorption which is defined an enthalpy change of desorption reaction. The adsorbents that are usually used in TPD are different amines such as NH_3, pyridine, *n*-butylamine, quinolone etc. [41].

Hence, the TPD experiments have been done on protonated forms of the zeolites FAU, FER, MFI and MOR using ammonia as the adsorbed base gas [42]. This investigation has been carried out in order to study the acid strengths dependence on the location of OH groups. It has been shown that in FAU zeolite the stronger acid sites are mostly located in supercages, while weaker acid sites are located in sodalite cages.

Sodalite cage has both 4-membered and 6-membered rings in its structure. The cage has an internal diameter of approximately 6Å, thus, only small molecules can enter into cages of such type, while a supercage formed by larger number of T atoms can encapsulate both molecules of big and small size. In contrast to the finding presented above, in MOR, FER and MFI zeolite the acid strength of the acid sites in different regions are found to be equal. However, this method has several disadvantages. For instance, ammonia can be adsorbed on the non-acidic part of a surface, in this case TPD does not show the acid strength directly.

Besides, TPD data has been obtained by means of computational modeling by Sauer et al. [43] within a study of the influence of the type of framework of zeolite and crystallographic position of the acid sites on acidity. There have been considered the models of FAU, CHA, MOR and MFI (ZSM-5) zeolites with protons located at O1 in FAU, O1 in CHA, O2 in MOR and O17 in MFI correspondingly. The adsorption of NH_3 has been considered. The calculated heats of NH_3 adsorption have given the following sequence in the acid strengths: MOR > CHA ≈ FAU > MFI. When ammonia is adsorbed on the acid site the deprotonation and formation of NH_4^+ cation may occur. Thus, another parameter, the heat of deprotonation, has been considered. In contrast to the assumption derived from the values of heat of adsorption, the calculated deprotonation energies suggest the following sequence in acid strengths: FAU > CHA > MOR > MFI. This result reveals that TPD method is not able to fully define the strengths of the acid sites as in some case it can be controversial, this means that some other complementary methods should be used in order to justify the obtained results.

Microcalorimentry is another method of the measuring of enthalpies of the acid base interactions. During such experiment the aliquots of reference base are dosing onto the zeolite at a given temperature. The enthalpy of a current adsorption process is recorded and integrated. The experiment continues until saturation coverage is achieved. The resulting data are represented as plot of enthalpy of adsorption as the function of the

coverage. The study of Parrillo et al. [44] describes the used microcalorimetry to measure the heats of adsorption of a series of alkylamines and a series of substituted pyridines in H-ZSM-5 and H-MOR. Thus, for instance, plot of enthalpy of adsorption as the function of the coverage for the adsorption of 2-fluoropyridine (circles), 2-methylpyridine (triangles), and 2,6-dimethylpyridine (squares) on H-Mordenite (H-M) zeolite at 470 K is presented in **Figure 6**.

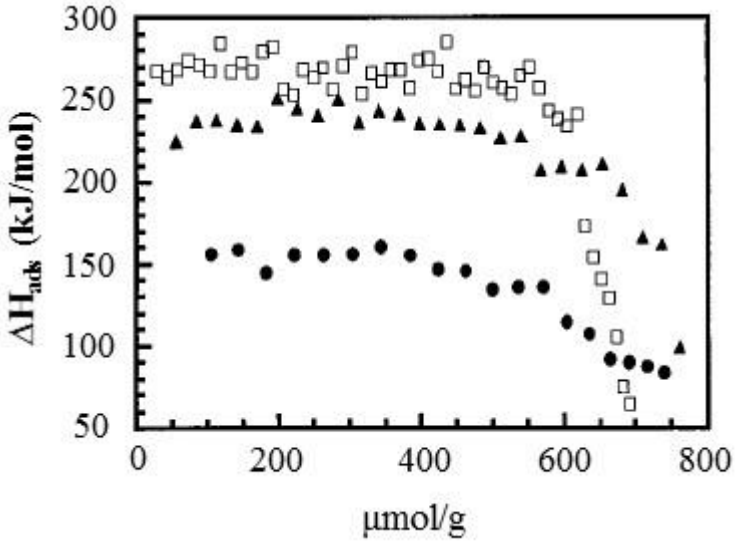

taken from [44]

Figure 6. Differential heats of adsorption of 2-fluoropyridine (circles), 2-methylpyridine (triangles), and 2,6-dimethylpyridine (squares) on H-M at 470 K

By analyzing the plots obtained for the adsorption of different alkylamines and pyridines at different temperatures, it has been concluded that the scale of acid strengths cannot be obtained from heats of adsorption of ammonia or pyridine or any other single reference base and the calorimetric study should be combined with another spectroscopic methods.

Consequently, a combined Infrared and calorimetric study of H-Y zeolite have been done [45]. Within this study heats of adsorption of different bases on H–Y zeolite have been measured at 473 K. There are two different OH sites found in H-Y zeolite, which stretching vibrational frequencies have been found at 3640 and 3550 cm^{-1} respectively.

In case of pyridine, the heat of adsorption were larger on OH sites at 3640 cm^{-1} than 3550 cm^{-1}, which means that the sites vibrating at 3640 cm^{-1} has stronger acid strengths. However, another tendency has been found in case of adsorption of ammonia and piperidine. This can be explained by positional difference between the two OH sites (some of them are supposed to be situated in small and others in big cavities), molecular size of the adsorbed bases and differences in proton mobility caused by different strength of the bases being adsorbed.

Computational modeling can be also applied in order to estimate the acid strengths of Brønsted sites. The factors that contributes to the acidity of seven high-silica zeolites have been studied by means of computational chemistry methods [46]. ^{1}H, ^{15}N and ^{13}C NMR chemical shift parameters have been calculated in order to characterize the strengths and accessibility of Bronsted acid sites in several zeolite samples (CHA, FAU, FER, MFI, MOR, MTW and TON). Acetonitrile has been used as a base probe molecule. It was calculated that in the absence of any adsorbed base molecule the sequence in order of decreasing of the acid strengths is the following: MFI > MOR > MTW > CHA > FER > TON > FAU. In this case the calculated frequencies of OH stretching vibrations and the gradient norm of the electronic potential at the proton site have been considered. Then, the adsorbed acetonitrile was introduced using Monte Carlo method. Acidity was defined as the strengths of O-H---N hydrogen bond, which was characterized by several geometrical parameters and by adsorption energy, all the magnitudes have been calculated using DFT calculations. It was estimated the following sequence in order of decreasing of the strength of the hydrogen bond: MFI > FAU > MOR > MTW > CHA > FER > TON. However, these results can be questioned if the work of Sauer et al.

discussed above [33] is taken into account as there was found no correlation between the O-H stretching vibrational frequencies and deprotonation energy and it has been concluded that there is possibly a dependence of the O-H stretching frequency of the acid sites, not only on the local environment (the number of the Al atoms in the closest neighborhood and crystallographic position) but also on the overall composition of the lattice framework.

Another study has been done by Sauer [47] on the relative acidity of zeolitic Brønsted sites in thin films and in bulk materials with the ammonia and pyridine molecules adsorbed. Calculated deprotonation energies indicate a much higher intrinsic acidity for Brønsted sites in two-dimensional aluminosilicates than in bulk zeolites, whereas the energy of ammonia adsorption shows hardly any difference. This is due to the interaction of the NH_4^+ cation formed on protonation of NH_3 with the negatively charged surface site.

Moreover, a computational study has been done by Senchenya et al. [48]. In this study the interaction of carbon monoxide (CO) molecule with both OH groups of zeolite acid sites has been studied by means of SCF (Self-Consistent Field) and MP2 (second-order Møller–Plesset theory) calculations. The interaction has been considered on minimal-size clusters with the structure formula H_3SiOH for the silanols and $H_3SiOHAl\ H_3$ for the acid sites, respectively through both C and O ends of CO molecule. It has been found that the complexes CO-zeolite complexes (via C atom) formed on the acid sites are more stable than OC-zeolite complexes (via H atom). It also has been seen that not only O-H stretching vibrations are sensitive to the formation of such complexes, but also in-plane and out-of-plane OH-bending vibrations shift when the complexes are formed, this confirms that the vibrational region in which bending modes are found is of an investigation interest.

Another factors such as Si/Al ratio and the presence of cations in the framework of zeolite have a great impact on zeolite acidity. Datka and Mortier [49] have studied the influence these factors on the framework characteristics of zeolites by both IR spectroscopy and ab initio quantum chemical calculations. It has been found that the increase of electronegativity of the system caused by increase of presence of Al (and so acid sites) and cations increases the bond strengths. Furthermore, the values of O-H dissociation energies for different kinds of acid sites that are present in NaHX and NaHY zeolites have been derived from IR spectra [50]. They have been also calculated by means of computational modeling. According to both experimental and computational results, the increase in the number of Al atoms close to the acid site decreases the acid strengths of this acid site. Then, Grajciar et al. [51] have done a periodic DFT study on the models of H-FER zeolite with different Si/Al ratios in order to investigate the effect of aluminium content on the zeolite acidity. It has been found that some types of acid sites are formed only when the Si/Al ratio is relatively high, furthermore, the relative stability of the acid sites was found to be dependent on the Si/Al ratio.

Another work of Datka et al. [52] has been dedicated to the investigation of acidity of NaH-MOR zeolite by means of IR studies of ammonia adsorption. It has been shown that the O-H stretching frequencies vary with the change in the Na/H exchange degree which suggests the variation of the acid strength.

1.4 Why should we use neutrons to measure Brønsted acidity in zeolites?

As it can be seen from the section discussed above, there is a number of techniques that have been used until nowadays for characterization of zeolites including: computational modeling, infrared and nuclear magnetic resonance spectroscopy, etc. However, none of

these methods itself is able to fully describe the factors that influence the Brønsted acidity of zeolites. For instance, until the present moment finding the distribution of aluminum atoms in a zeolitic framework remains a challenging task since the information obtained by NMR is incomplete. In addition to that, silicon and aluminium atoms are not accurately distinguishable by usual X-ray techniques due to small difference between their atomic numbers. The neutron powder diffraction has been performed on the deuterated acid form of zeolite ERS-7 in order to predict the occupancies and positions of the acid deuterons. It has been shown that acid deuterons were located approximately 1 Å from oxygens O3, O5, and O7, with occupancy factors of 0.16, 0.16, and 0.18 [53]. Nevertheless the information obtained by this technique does not give directly the location of the acid sites in zeolites.

Even though Inelastic Neutron Scattering (INS) is not frequently used for the study of zeolites, it could be used in future as a powerful tool in description of vibrations in zeolite framework. INS provides information about all vibrational movements in the systems containing hydrogen atoms and the intensities of the peaks are defined by individual atomic displacements of the atoms in the investigated system. While in case of other vibrational techniques the incident beam interacts with electrons, neutrons interact with the nuclei and so there are no selection rules for such interaction and vibrational intensities can be obtained straightforward from the atomic movement.

Furthermore, the use of neutron techniques has several advantages in contrast to other spectroscopic techniques. First, neutron has zero charge therefore when neutrons interact with the matter of investigated sample there is no Colomb barrier to be overcome. Second, when acidity of zeolites is estimated the most important advantage of neutron scattering in comparison to other methods is that the hydrogen atom has large scattering cross-section ($\sigma_H = 80 >> \sigma_{Si}, \sigma_{Al}, \sigma_O$). This magnitude is at least 100 times larger for hydrogen atom in comparison to other atoms that may be presented in the framework of zeolites such as Al, Si and O. This means that INS is very sensitive to presence of hydrogen atoms (see 2.1).

As it was described above, among all the vibrational techniques, IR technique is one of the most common spectroscopic techniques used in zeolite study and it describes the O-H stretching movements. However, in-plane and out-of-plane bending modes cannot be directly measured by IR, due to the fact that the spectral region where these modes are situated is dominated by intense vibrations of the zeolitic framework [54-56]. In-plane OH bending modes have been derived from overtones and combination bands by diffuse reflectance spectroscopy, taking into account anharmonicity [57] and it has been shown that the bending modes are more sensitive to the structure and composition of the zeolites than the stretching modes.

In its turn INS can be applied in order to study bending vibrations of the hydrogen atoms in zeolites. Hence, the first application of INS technique in study of zeolites was done by Wax et al. [58], within this study the bonding of framework hydrogen to faujasite zeolite Rho has been examined. The peaks found at 1060 and 1150 cm^{-1} were assigned to OH-bending modes, however a large peak at 360 cm^{-1} was not taken into account, it was later suggested that this peak also corresponds to the OH bending vibration [59]. Then, another early INS study of zeolite was done in combination with Fourier transform infrared spectroscopy (FTI) in order to study the influence of the Si/Al ratio on the OH stretching and vibrations of the acid sites in Y zeolite [60]. Within this study out-of-plane

and in-plane bending modes have been detected at 419 cm^{-1} and 1089 cm^{-1} correspondingly. In addition to that, the FTI has been applied to study the influence of composition and structure of zeolite on the in-plane bending modes, as it has been shown that the exchange with deuterium gas (D_2) converts the Brønsted acid sites of these materials into their deuterated analogous [61]. Unlike the in-plane bendings of the acid sites, these modes of the OD-sites are found in the region from 850 to 900 cm^{-1}. The frequency of these modes shifts to higher wavenumbers with the increase of the Si/Al content. Then, Jobic et al. performed the INS study on HNa-Y zeolite in order to compare the findings with the existing IR results [62]. This study describes fundamental bending vibrations of OH groups (see **Figure 7**).

The vibrational bands presented by **Figure 7** has not been fully interpreted, nevertheless, it can be suggested, that the framework vibrations also appear in the region from 700 to 1000 cm^{-1}, as the hydrogen atoms is involved in such vibrational movement (for instance, the oxygen atom is bonded to the hydrogen atom, the Si (Al) – O stretching vibration will cause the O-H riding and the intensity of the INS peak corresponding to this mode will be relatively high).

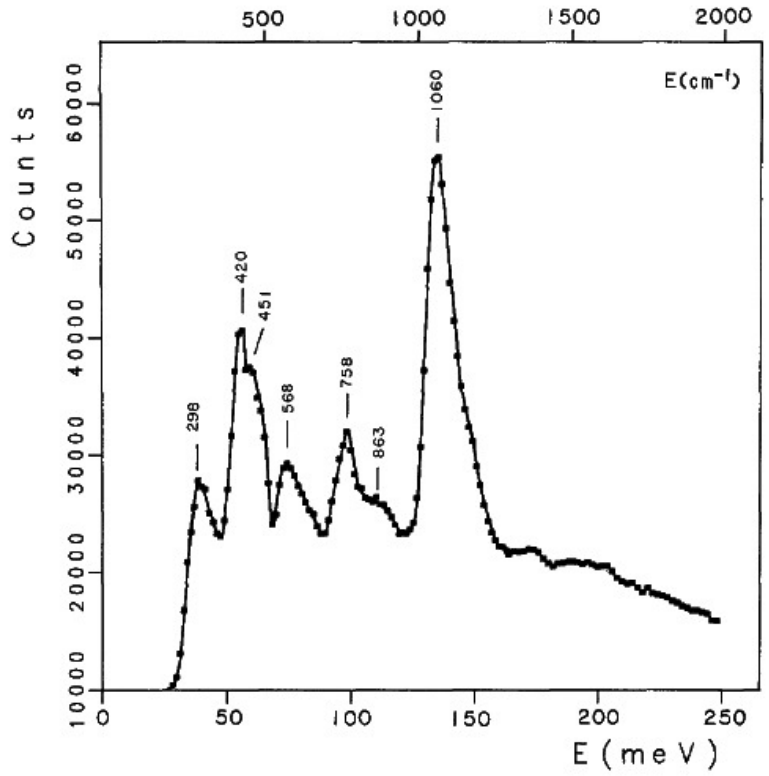

taken from [62]

Figure 7. INS spectrum of HNa-Y zeolite measured at 20 K

The study Jobic et al. revealed that INS can be applied in combination with computational modeling in study of zeolites. The INS spectra of zeolites X and Y, Na-ZSM and silicate were measured on the BeF spectrometer at the Institut Laue-Langevin (ILL) in the frequency range in which the SiOH bending modes are found [63]. The experimental results were compared with corresponding calculated spectra obtained by means of Molecular Dynamics and a good agreement was found (see **Figure 8**).

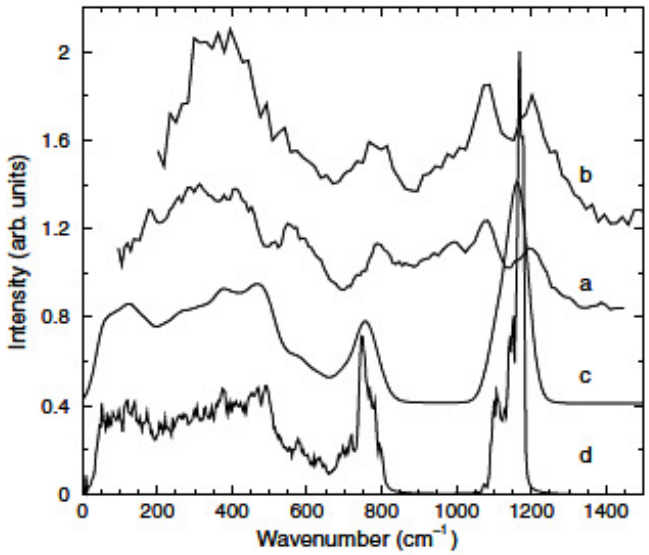

taken from [63]

Figure 8. Experimental INS spectra of silicate (a), Na-ZSM-5 zeolite (b), and calculated INS spectrum after (c) and before (d) correction for the resolution of INS spectrometer

This finding showed that consequently the computational modeling can be used in order to interpret the INS results. Nevertheless, Jobic did not obtained any structural information from his findings, because of the limitations caused by relatively low resolution of the spectra measured on BeF spectrometer and samples with high degree of heterogeneity and impurities.

The goal of the present work is to show that INS in combination with other techniques such as computational modeling and NMR spectroscopy is able to define the majority of the factors that influence the Brønsted acidity of zeolites (such as location of the acid sites, distribution of aluminium atoms in the framework of zeolites). The INS spectra of high quality measured by IN1-Lagrange spectrometer and samples of high purity

synthesized at ITQ enable this approach to be sensitive enough to even describe the acidic properties of zeolites with low content of hydrogen atoms (down to ½ H atom per unit cell). Finally, the present work is going to show that the use of INS opens new possibilities for acid characterization of zeolite catalysts largely employed in industrial chemical processes.

Chapter 2

Methods and materials

This chapter will present the methods that were used in this thesis work. This study is based on a combination of three methods: Inelastic Neutron Scattering, Density Functional Theory (DFT) computational modeling and Nuclear Magnetic Resonance (NMR) spectroscopy. Neutron scattering is a main experimental technique used in this study, the basis theory of this method is presented in the following subsection.

2.1 Introduction to neutron scattering

This subsection will give a short overview of the neutron scattering theory and will be mainly concentrated on INS.

2.1.1 Properties of neutron

Neutron Scattering is a spectroscopic technique in which the neutron is used to probe the dynamics of atoms in solids and their relative position. A nuclear physicist J. Chadwick discovered the neutron in 1932 [64] and in 1935 he received a Nobel Prize for his discovery. It appeared that neutron has no charge and so their electric dipole moment is considered as zero, and due to this fact neutrons can penetrate matter better than charged particles. Furthermore, the neutron's wavelength ($\lambda_n \sim 1 - 5$ Å) is close to interatomic distances and its energy is comparable with those of many excitations in condensed

matter, which means that neutron scattering also has a spectroscopic function [65]. In 1994 Brockhouse and Shull were honored with the Nobel Prize in physics for developing neutron scattering techniques for studying condensed matter [66]. As neutron interacts with matter rather via nuclear than electric forces, the interaction cross-section would depend on the internal structure of the nuclei of the investigated sample and not on the mass or electric charge of the atoms. Due to this fact neutron can be sensitive to both heavy and light atoms [67].

Nowadays, neutrons can be produced by both nuclear reactors and spallation sources. Nuclear reactors use a fission process to produce neutrons, while spallation process implies high-energy protons striking a solid target. The primary fission processes produce most of their neutrons at energies of a few MeV. This is a far too high energy to be useful for most of the neutron scattering techniques. Therefore, most of the neutron scattering facilities contain special neutron moderators arranged around the primary source in order to slow down the neutrons to useful energies.Materials used for moderation are chosen as they have a very specific set of properties. A moderator cannot absorb neutrons itself, however, it should be able to slow down neutrons to an acceptable speed. Different types of moderator materials are used to produce neutrons with different range of speed. Graphite moderators at 2000 K moderate hot neutrons with the energy range from 100 to 1000 meV. The use of deuterated water (D_2O) moderator at 300 K results in thermal neutrons with low speed and kinetic energy of about 25 meV which corresponds to the average energy of the particles of the ambient materials. Due to their properties thermal neutrons are usually used in investigation of properties of crystalline solids. Deuterium moderators (D_2) at 15-25 K give cold neutrons which energy is lower than 25 meV [68]. **Figure 9** shows the energy distribution of different types of neutrons produced by different moderators [69].

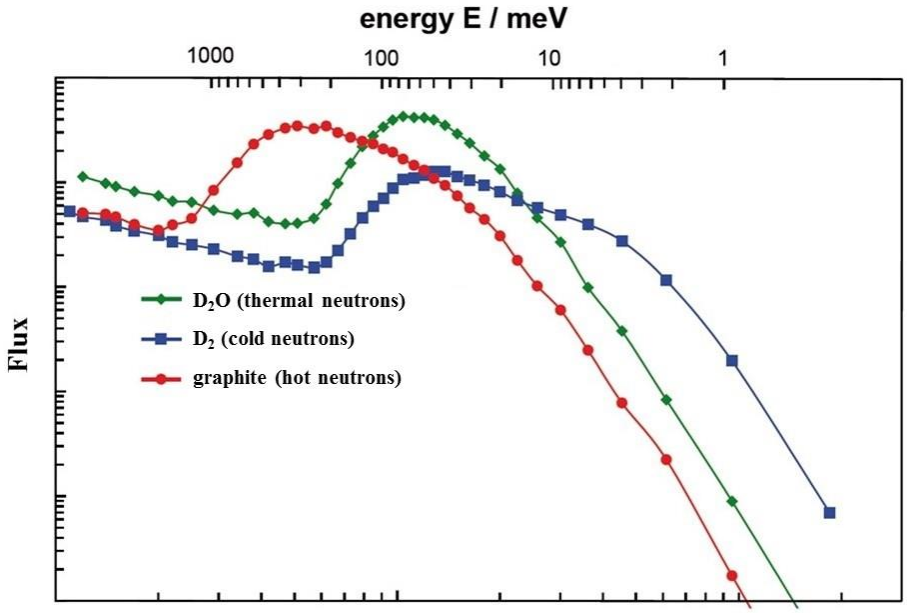

taken from [69]

Figure 9. Energy distribution of different types of neutrons produced by different moderators

The velocity spectrum of thermal neutrons is suitable for the majority of the neutron scattering experiments, however, in some experiments the velocities required for the incident neutrons are of the low energy range of the thermal spectrum, while in other experiments neutrons on the high-energy side are required. In order to perform scientific studies, it should be also known the connection between the values of velocity, energy and wavelengths of neutrons. The velocity spectrum of neutrons can be described by Boltzman distribution (where T is the temperature of moderator) and taking into account

the fact that neutron can behave as both particle and wave, the expression for neutron energy at temperature T can be presented by:

$$E \approx k_B T = \frac{1}{2} m v^2 = \frac{h^2}{2m\lambda^2} = \frac{\hbar^2 \mathbf{k^2}}{2m} \qquad \textbf{Equation 1}$$

In **Equation 1** m is the mass of a neutron, v is its speed, **k** and λ are neutron's momentum vector and wavelength correspondingly. k_B and $\hbar$ are Boltzman and Plank constants.

In order to describe the application of neutrons in neutron scattering experiments the basis of neutron scattering theory should be introduced.

2.1.2 Basis of neutron scattering

For instance, there is a beam of neutrons having the same incident energy E_i on a target (scattering system), which can be a crystal consisting of atoms. In such system E_f is the final energy of the neutron.

The result of the interaction between neutron and scattering system can be estimated by a quantity called cross-section. **Figure 10** shows the representation of a single neutron scattering event.

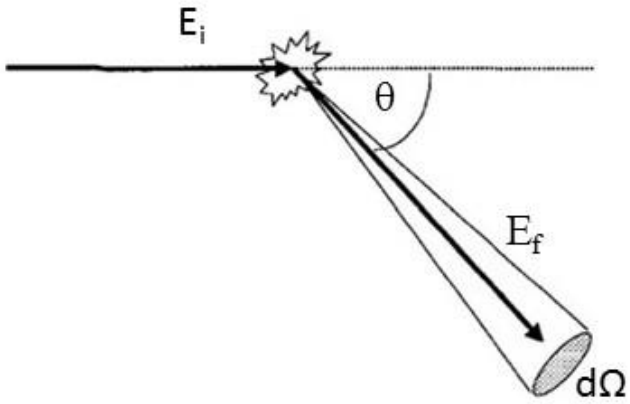

taken from [72]

Figure 10. A representation of a simple scattering event: the incident neutrons collide with the sample and some neutrons are scattered through an angle θ onto the detector of area dΩ

The angle θ is called a scattering angle and it can be defined as an angle of the neutron beam scattered by the sample onto a detector of area dΩ, which forms a solid angle. When the energy of the scattered neutron is not analyzed, then the cross-section can be represented by the differential cross-section $\frac{d\sigma}{d\Omega}$, which is defined as the magnitude that represents the sum of all processes in which the state of the scattering system changes from the initial wavevector β_i to final wavevector β_f, and the wavevector of the neutron changes from $\mathbf{k_i}$ to $\mathbf{k_f}$. This value is taken over all values of $\mathbf{k_f}$ that lie in the solid angle dΩ. The double-differential cross-section $\frac{d^2\sigma}{d\Omega dE_f}$ represents the specific transition of the scattering system from one of its quantum state to another and it is defined as the ratio of the number of particles scattered per unit time per unit solid angle, divided by incident flux. For instance, if the scattering system consists of N nuclei and $\mathbf{R_j}(\mathbf{t})$ is the coordinate

vector of the j[th] nucleus (j=1…..N) at time t, **r** is the coordinate vector of neutron, hence, the expression for $\frac{d\sigma}{d\Omega}$ can be represented by [70]:

$$\frac{d\sigma}{d\Omega} = \frac{\mathbf{k_f}}{\mathbf{k_i}} \left(\frac{m}{2\pi\hbar^2}\right)^2 |\langle \beta_f, \mathbf{k_f}|V|\beta_i, \mathbf{k_i}\rangle|^2 \qquad \textbf{Equation 2}$$

Where m is the mass of neutron and $|\langle \beta_f, \mathbf{k_f}|V|\beta_i, \mathbf{k_i}\rangle|$ is the matrix element of the interaction potential V, which can be defined as the sum of the potentials of the neutron due do the j[th] nucleus:

Equation 3

$$V = \sum_j V_j (\mathbf{r} - \mathbf{R_j})$$

The square of the matrix element gives the probability of the transition from the state $|\beta_i, \mathbf{k_i}\rangle$ to the state $\langle \beta_f, \mathbf{k_f}|$.

Let's consider all neutrons having the same energy, determined by conservation energy and $E_i + E_{\beta_i} = E_f + E_{\beta_f}$ (where E_{β_i} and E_{β_f} are the initial and final energies of the scattering system). In mathematical terms the energy distribution of the scattered neutrons is a $\delta(E_{\beta_i} - E_{\beta_f} + E_i - E_f)$ (Dirac delta-function).

By using a fundamental statement of quantum mechanics known as Fermi's golden rule, the expression of the double-differential cross-section can be represented as the following:

$$\frac{d^2\sigma}{d\Omega dE_f} = \frac{\mathbf{k_f}}{\mathbf{k_i}} \frac{m^2}{4\pi^2\hbar^4} |\langle \beta_f, \mathbf{k_f}|V|\beta_i, \mathbf{k_i}\rangle|^2 \delta(E_{\beta_i} - E_{\beta_f} + E_i - E_f) \qquad \textbf{Equation 4}$$

This expression is called the master equation of scattering and it is based on the first Born approximation. Neutrons are scattered by the nucleus due to the strong nuclear force, which has an interaction range much smaller than the neutron wavelength. In this context, Born approximation allows to use only the first term in the expansion of the wave function (taken into account the interaction potential V), which describes a single scattering process of the incident wave, and the following terms describe scattering processes of higher order known as multiple scattering. The Born approximation assumes that both the incident and scattered neutrons can be described as plane waves, with only one single scattering event of the incident wave from the interaction potential [71]. The interaction potential V represents the interactions of neutrons with the j^{th} nucleus of the sample and can be described by the Fermi pseudo-potential [70]:

Equation 5

$$V_j\left(\mathbf{r}-\mathbf{R_j}\right)=\frac{2\pi\hbar^2}{m}b_j\delta\left(\mathbf{r}-\mathbf{R_j}\right)$$

In this expression the term b_j is called the nuclear scattering length of the j^{th} nucleus. The scattering length of an element depends on the type of its isotopes and, if present, on the direction of its nuclear spin with respect to the spin of the incident neutron. Moreover, from the **Equation 5**, it can be concluded that the interaction potential (V) is a sum of contributions of the interaction potentials of the individual scattering centers and that those individual interaction potentials are of a short-range end can be represented by a Dirac delta function. For a fixed $\mathbf{k_i}$ and $\mathbf{k_f}$ the Fourier transform V(**Q**) of the potential for the scattering system is given as:

Equation 6

$$V(\mathbf{Q})=\sum_j\frac{2\pi\hbar^2}{m}b_j e^{i\mathbf{Q}\,\mathbf{R_j}}$$

Now, the **Equation 4** can be also rewritten as [71]:

$$\frac{d^2\sigma}{d\Omega dE_f} = \frac{\mathbf{k_f}}{\mathbf{k_i}} \frac{1}{2\pi\hbar} \sum_{j,j'}^{N} \overline{b_j b_{j'}} \int_{-\infty}^{\infty} \langle e^{-i\mathbf{Q}\,\mathbf{R}_{j'}(\mathbf{0})} e^{i\mathbf{Q}\,\mathbf{R}_j(t)} \rangle\, e^{-i\omega t} dt \qquad \textbf{Equation 7}$$

where N is the number of nuclei in the scattering system, **Q** is the momentum transfer ($\mathbf{k_i} - \mathbf{k_f}$), ω is the energy transfer ($E_i - E_f$)/$\hbar$, the sum is over pairs of nuclei j and j' and that the nucleus labeled j is at position $\mathbf{R_j}(t)$ at time t and nucleus labeled j' is at position $\mathbf{R}_{j'}(\mathbf{0})$ at time 0. The $\langle ... \rangle$ stand for the average over all possible thermodynamic states of the scattering system. It should be taken into account that $\mathbf{R_j}$ is a quantum mechanical operator, nevertheless we treat the equation (7) as it describes the system from the point of view of classical mechanics because such an approach clarifies the physical meaning of the equation.

2.1.3 Coherent and incoherent scattering

In this subsection we will discuss a specific aspect in the neutron scattering, which is the distinction of coherent and incoherent neutron scattering. Considering a scattering system consisting of a single element where the scattering length varies from one nucleus to another owing to the presence of nuclear isotope or spin, we can define that the coherent scattering is a type of scattering, which would be given by the same system if all the scattering lengths were equal to their mean value. While the incoherent scattering comes from the deviations of the scattering lengths of the actual system from their mean value. Assuming that the scattering system contains a large number of scattering centers and every possible nuclear isotope and spin orientation exists with the random distribution, the **Equation 4** can be reformulated as the following:

$$\frac{d^2\sigma}{d\Omega dE_f} = \left(\frac{d^2\sigma}{d\Omega dE_f}\right)_{coh} + \left(\frac{d^2\sigma}{d\Omega dE_f}\right)_{inc} \qquad \textbf{Equation 8}$$

Equation 8 includes coherent and incoherent partial differential cross section. In case of the scattering systems consist on 1 element these terms can be separated in two equations:

• When $j \neq j'$, the coherent partial differential cross section can be defined by:

$$\left(\frac{d^2\sigma}{d\Omega dE_f}\right)_{coh} = \frac{\mathbf{k_f}}{\mathbf{k_i}} \frac{1}{2\pi\hbar} \frac{\sigma_{coh}}{4\pi} \sum_{\substack{j,j' \\ j \neq j'}}^{N} \int_{-\infty}^{\infty} \langle e^{-i\mathbf{Q}\,\mathbf{R}_{j'}(\mathbf{0})} e^{i\mathbf{Q}\,\mathbf{R}_j(t)} \rangle\, e^{-i\omega t} dt \qquad \textbf{Equation 9}$$

where σ_{coh} stands for the coherent cross-section. If we take into account that when $j \neq j'$, $\overline{b_j b_{j'}} = (\bar{b})^2$, $\bar{b_j} = \sum_i \rho_j^i b_j^i$, where ρ_j^i is a probability that the scattering lengths of the element at position $\mathbf{R_j}$ has the value b_j^i and if the scattering systems consist on 1 element the coherent cross-sections would have the following values [70]:

$$\sigma_{coh} = 4\pi(\overline{b})^2 \qquad \textbf{Equation 10}$$

Equations 9 and **10** show that coherent scattering of the crystal depends on the correlation between the positions of the same nucleus at different times and (in general) of different nuclei at different times and thus results in interference effects.

• On the other hand, when $j = j'$, incoherent partial differential cross section can be defined by:

$$\left(\frac{d^2\sigma}{d\Omega dE_f}\right)_{inc} = \frac{\mathbf{k_f}}{\mathbf{k_i}}\frac{1}{2\pi\hbar}\frac{\sigma_{inc}}{4\pi}\sum_{j,j'}^{N}\int_{-\infty}^{\infty}\langle e^{-i\mathbf{Q}\,\mathbf{R}_j(\mathbf{0})}e^{i\mathbf{Q}\,\mathbf{R}_j(t)}\rangle e^{-i\omega t}dt \qquad \textbf{Equation 11}$$

where σ_{inc} is incoherent cross-section.

If we take into account that when $j = j'$, $\overline{b_j b_{j'}} = \overline{b^2}$, $\overline{b_j^2} = \sum_i \rho_j^i (b_j^i)^2$ and a scattering systems consist on 1 element the incoherent cross-sections would have the following values [70]:

$$\sigma_{inc} = 4\pi\left[\overline{b^2} - (\overline{b})^2\right] \qquad \textbf{Equation 12}$$

The Equations 11 and 12 show that incoherent scattering depends only on the correlation between the positions of the same nucleus at different times and thus contains information about processes in which atoms diffuse.

Experimentally obtained values for σ_{coh} and σ_{inc} and so the values of corresponding scattering lengths for all common isotopes can be found in the literature, some of them are presented in Table 2.

Table 2. Scattering cross sections of the elements (the values are taken from [72])

Element	σ_{coh}	σ_{inc}	σ_{tot}
H	1.7568	80.26	82.02
C	5.551	0.001	5.552
N	11.01	0.5	11.51
O	4.232	0.0008	4.232
Si	2.163	0.004	2.167
Al	1.495	0.0082	1.503
S	1.0186	0.007	1.026

the values are taken from [72]

For most isotopes $\sigma_{coh} >> \sigma_{inc}$. However, in case of a hydrogen atom σ_{inc} is much bigger than σ_{coh} and much bigger than the value of σ_{inc} of all other isotopes. Hence, incoherent neutron scattering is a powerful tool to investigate the dynamics in hydrogen containing systems.

2.1.4 Energy and momentum conservation laws

A scattering process can be described by scattering triangle (see **Figure 11** a) and b)). It shows that the magnitude and direction of momentum transfer vector **Q** is determined by the magnitudes of the wave vectors for the incident and scattered neutrons and the angle 2θ by which the incident neutron is scattered during the scattering process. The angle 2θ is called the scattering angle [73].

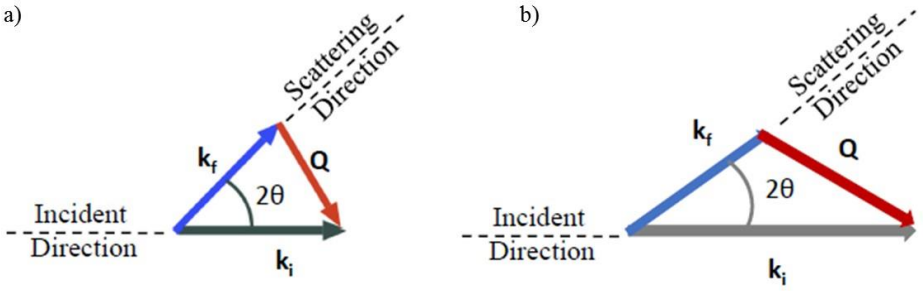

Figure 11. Scattering triangles for: a) an inelastic scattering event ($k_i = k_f$), b) an inelastic scattering event ($k_i \neq k_f$).

The scattering process can undergo via 2 ways: the incident neutron conserves its energy (**Figure 11 a)**) or neutron can loose and gain energy, i.e. the nucleus gains the energy lost by the neutron or nucleus gives its energy to the neutron (**Figure 11 b)**). The process in which the neutron's energy and therefore its momentum remains unchanged ($E_i = E_f$ and $\mathbf{k_i} = \mathbf{k_f}$) is called elastic neutron scattering and the process during which the neutron loses or gains energy is called inelastic neutron scattering ($E_i \neq E_f$ and $\mathbf{k_i} \neq \mathbf{k_f}$) correspondingly.

For elastic scattering the modulus of momentum vectors are equal $|k_i| = |k_f| = k$ and energy transfer is zero. The modulus of $|Q|$can be derived from the trigonometric rules.

For inelastic scattering the modulus of momentum vectors are not equal $|k_i| \neq |k_f|$. As $\mathbf{Q} = \mathbf{k_i} - \mathbf{k_f}$, the modulus of vector **Q** can be calculated by using trigonometric rules for the difference between two vectors, so

$$|Q|^2 = |k_i|^2 + |k_f|^2 - 2\cos|k_i||k_f| \qquad \textbf{Equation 13}$$

Usually in a collision of particles the total energy and momentum are conserved. When the neutron is scattered by a sample, the energy lost by the neutron ($E_{total} = \hbar\omega$) is equal to the energy gained by the sample. This is called energy conservation law and it is can be expressed by:

$$E_i - E_f = \frac{1}{2}mv_i^2 - \frac{1}{2}mv_f^2$$ **Equation 14**

Taking into account that $\frac{1}{2}mv^2 = \frac{\hbar^2\mathbf{k^2}}{2m}$ (see **Equation 1**)

$$E_i - E_f = \frac{\hbar^2 k_i^2}{2m} - \frac{\hbar^2 k_f^2}{2m} = \hbar\omega$$ **Equation 15**

Q is the momentum transfer and it can be expressed in vector form by:

$$\mathbf{Q = k_i - k_f}$$ **Equation 16**

In neutron scattering studies there are two aspects that define the choice of the instrument. First, it should be defined if the goal of the experiment is to describe the dynamics or the structure of the systems. This should be known since different kind of instruments either diffractometer or spectrometer are used for these two different purposes. Second, in case of the measurements where spectrometer is used the kind of spectrometer and the kind of neutrons given by different moderators, thermal, hot or cold, (see **Figure 9**) will define the energy and momentum transfer range of the particular instrument, which is called 'kinematic range'. Below it will be shortly introduced a kinematic range of INS instruments.

2.1.5 Inelastic neutron scattering

2.1.5.1 Kinematic range of INS instruments. Spectrometers with direct and indirect geometry

Inelastic neutron scattering (INS) is a method for investigating the atomic dynamics in the sample. The aim of all the neutron scattering measurements is to find the scattering function S (**Q**, ω). In order to do this it should be known the range of momentum and energy transfer that can be reached with by the instrument used in the experiment. It can be obtained from the conservation laws for the momentum and energy transfer of a given inelastic neutron scattering spectrometer from the **Equations 14** and **15**.

From these equations we can define the correlation between momentum and energy transfer:

$$\frac{\hbar^2\mathbf{Q^2}}{2\mathrm{m}} = 2\mathrm{E_i} - \hbar\omega - 2\sqrt{\mathrm{E_i}(\mathrm{E_i} - \hbar\omega)}\cos 2\theta \qquad \textbf{Equation 17}$$

Equation 17 is called kinematic range and it determines the range of (**Q**, **ω**) space that can be covered in a scattering experiment. There are two types of spectrometers that are used in inelastic neutron scattering experiments: spectrometers of direct and indirect geometry.

When the spectrometers with direct geometry are used the incident neutron energy $\mathrm{E_i}$ is fixed, so the energy transfer is obtained by changing the final energy $\mathrm{E_f}$. For instance, if the incident energy is taken as $\mathrm{E_i} = 100$ meV, then for different scattering angles (2θ), the accessible range of (**Q**, **ω**) space would be the following (see **Figure 12**).

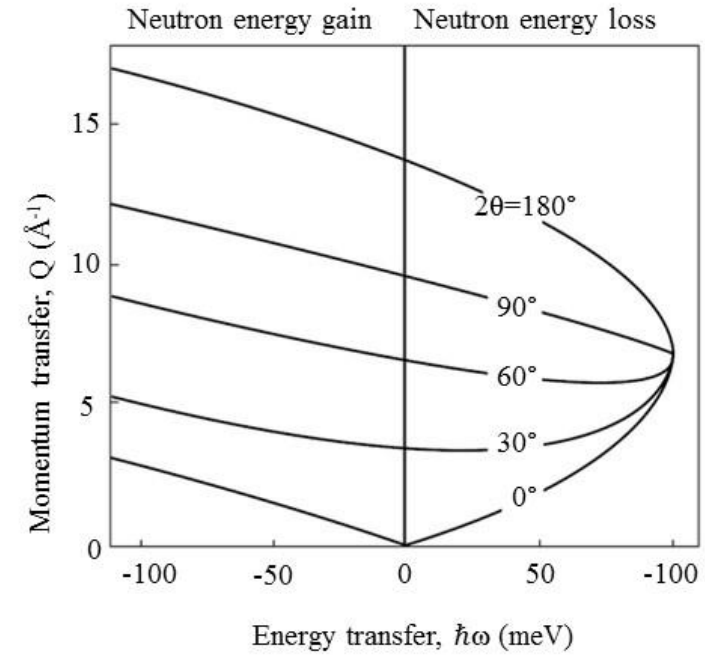

taken from [72]

Figure 12. The region of (Q, ω) space accessible with the direct-geometry spectrometer at fixed incident energy $E_i = 100$ meV and different scattering angles (2θ)

In case of experiments with indirect-geometry spectrometers the final energy E_f is fixed and the initial energy $E_i$varies. The **Equation 17** takes the following form:

$$\frac{\hbar^2 \mathbf{Q^2}}{2m} = 2E_f + \hbar\omega - 2\sqrt{E_i(E_f + \hbar\omega)}\cos 2\theta \qquad \textbf{Equation 18}$$

For instance, for the IN1 (Lagrange) spectrometer which has a fixed final energy $E_f = 4.5$ meV and the incident energy varies from 5 to 500 meV the kinematic range for

different scattering angles would be presented as those shown by **Figure 13**. The important point is that a given configuration of the spectrometer corresponds to a single point in $(\mathbf{Q}, \boldsymbol{\omega})$ space, therefore there is no Q-dependence. Unlike indirect-geometry spectrometers, spectrometers with direct geometry can access any point of the $(\mathbf{Q}, \boldsymbol{\omega})$ space for a determined energy transfer (see **Figure 12**)

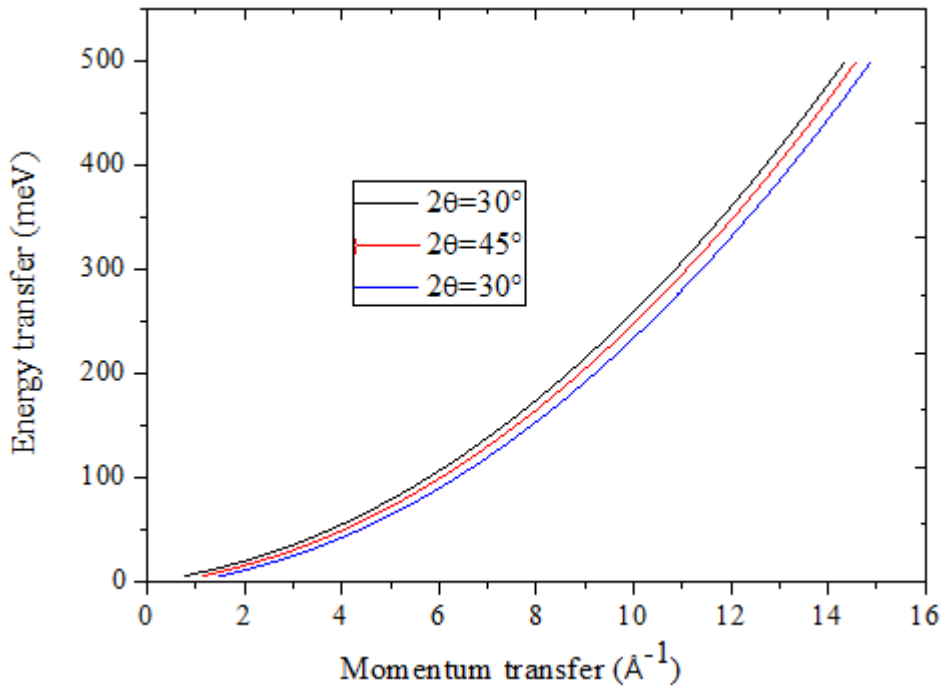

Figure 13. The region of $(\mathbf{Q}, \boldsymbol{\omega})$ space accessible with the direct-geometry spectrometer at fixed final energy $\mathbf{E_f = 4.5}$ meV and different scattering angles $(2\boldsymbol{\theta})$

2.1.5.2 IN1-Lagrange instrument

The first INS spectrometer was a triple axis spectrometer (TAS), which allows to determine the energy transfer by analysis of the wavelength. This type of instrument, which nowadays remains in wide use [74] employs monochromators to fix both $\mathbf{k_i}$ and

$\mathbf{k_f}$, thus it can access a big range of momentum and energy transfer (**Q** and ω). The efficiency of such spectrometer can be increase by fixing either $\mathbf{k_i}$ or $\mathbf{k_f}$ (spectrometers with direct and indirect geometry respectively).

IN1-Lagrange (LArge Graphite ANalyser for Genuine Excitations) is a spectrometer with indirect geometry. It is installed at the hot neutron source of the high flux ILL reactor. This instrument can be applicable as a powerful tool in study of a wide range of different systems, such as zeolites and metallic catalysts, hydrides of metals and intermetallic compounds, nano-crystalline materials, geochemistry matters etc. [75]. The design of Lagrange is presented by **Figure 14** [76].

First, the incident neutron beam is monocromatized by one of the monochromators installed in Lagrange, which are: Cu220 with the incident energy range 27 ÷ 500 meV (or 220 ÷ 4000 cm^{-1}); Si111 with the incident energy range 4.5 ÷ 20 meV (or 36 ÷ 160 cm^{-1}) and Si311 with the incident energy range 16.5 ÷ 200 meV (or 133 ÷ 1613 cm^{-1}) and Cu331 with the incident energy range 67 ÷ 500 meV (or 540 ÷ 1613 cm^{-1}) respectively. Second, the monochromatic beam of the incident energy $\mathbf{k_i}$ interacts with the sample.

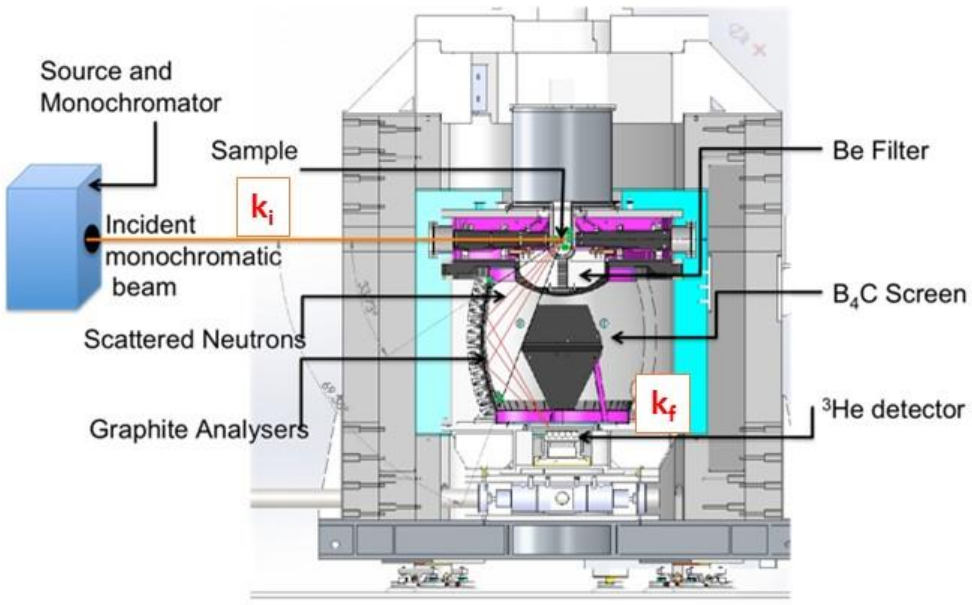

taken from [76]

Figure 14. The vertical cut of the Lagrange design

Then, the Beryllium filter, installed right after the sample, removes scattered neutrons with energies higher than 5.2 meV in such a way that the high-order harmonics are excluded from the analyzer reflections. The scattered neutrons are reflected by the focusing reflecting surface of 1 m^2, which is built around the vertical sample detector axis from pyrolytic graphite crystals set to reflect neutrons with the fixed average energy ($\mathbf{k_f}$) of 4.5 meV. This surface is presented as a segment of the sphere with the large solid angle (up to 2.5 steradian). The scattered neutrons are registered with a small single counter (^{3}He detector). The INS spectra obtained within our study were recorded at 5 K using Cu220 monochromator that allows to access the incident energy from 200 to 2400 cm^{-1} with an energy resolution ≈ 2 %.

2.1.5.3 Incoherent approximation

Lagrange is an indirect-geometry spectrometer with low fixed final energy therefore the trajectory through (**Q**, **ω**) space is also fixed. This simplifies the operation of the instrument and provides high resolution of the spectra. For most energy transfers $\mathbf{k_i}$ is much larger than $\mathbf{k_f}$, so the momentum transfer **Q** is large in comparison to $\mathbf{k_f}$ and almost equal to $\mathbf{k_i}$. The scattering triangle of such a process is shown in **Figure 15.**

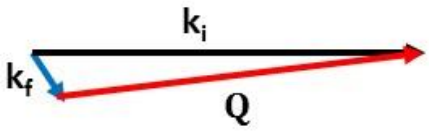

Figure 15. Scattering triangle for the case where $k_i \gg k_f$

In the neutron scattering experiments the measured quantity is proportional to S(**Q**, **ω**) and it contains the information about the excitations and so vibrations in the investigated sample. The interference of the scattered neutron waves occurs when the nuclei are fixed in their equilibrium position in the lattice, in this case the diffraction patterns can be obtained. As in real molecules atoms are not fixed in a certain position, the internal thermal energy makes them oscillate around their equilibrium position (lattice or framework position). As the magnitude of the momentum transfer vector **Q** increases, the strength of elastic scattering decreases and most scattering occurs with an exchange of energy. When this value overcomes the values of the order of the atomic excitations (such as vibrations, rotations etc.) and so the wavelengths of these neutrons is higher than interatomic distances, diffraction pattern no longer can be obtained. In this case dynamic response can be calculated simply by treating this scattering as if it were

incoherent. This assumption is called incoherent approximation. And this is the case for the Lagrange spectrometer.

In the following subsections a short introduction of the representation of INS measurements will be presented.

2.1.5.4 Scattering law

The neutron spectroscopic data are usually represented via scattering law, which describes all the molecular vibrations occurring in the investigated system in a straightforward way. The scattering law can be summarized into the scattering function S (**Q**, ω), which is directly related to the observed intensities when those summed over all the atoms in a sample. That is why the scattering law can be determined as the natural meeting point of experimental data and the dynamical models that have been developed for its understanding.

$$S(Q, \omega_j)_i^n \sim \sigma_i \frac{(Q\ U_i)^{2n}}{n!} \exp[-Q\ U_{tot}]^2 \qquad \textbf{Equation 19}$$

The scattering function S (**Q**, ω) emphasizes the dynamics of each individual atom in the sample related to the density of states and it is dependent on the momentum and energy transfer, **Q** and ω correspondently, U_i is an atomic displacement for a given atom i, U_{tot} is a sum of atomic displacements of all the atoms the system and σ_i is a total scattering cross-section of a given atom [72]. From the expression of the scattering law, it can be concluded that it gives the relative intensities of the each j^{th} mode determined at a momentum transfer Q and energy transfer ω_j for the each atom i with the cross section σ_i, and finally, n is the excitation state. In case of hydrogenous systems the total cross-section stands for the total bound scattering cross section of each atom and the dynamics are always treated as incoherent, irrespective of the momentum transferred. Furthermore,

as incoherent cross-section of the ^{1}H is around 80.3 barn, while that value of most of the other elements is lower than 5 barn (see **Table 2**), in the hydrogenous materials the scattering is dominated by that of the hydrogen atoms. This fact makes INS an efficient tool in the study of the vibrational movement associated with the hydrogen atoms.

As it was already mentioned, the Scattering law contains the information about all the vibrational movements of the atoms in the system observed by neutron experiments, it also can be defined as theoretical representation of the generalized density of states (GDOS ~ S (Q, n*ω_i)), which is defined as the probability of the finding the atom in the particular position at the given moment of time.

The theoretical representation of the experimental generalized density of states is used in order to compare experimental and computationally calculated data. The calculated spectra are represented by theoretical vibrational density of states VDOS, which has been obtained from the normal mode analysis, and this procedure will be described in the following subchapter 2.2.1. VDOS ($g(\omega)$) is defined as sum of the individual atomic contribution to the vibrational density of states and it can be represented by the following expression VDOS(ω)=$\sum_i n_i\, g_i\,(\omega)$, where n_i is a quantity of the atoms of type *i* (in case of zeolites, H, Si, Al and O) in the system and $g_i\,(\omega)$ is their corresponding partial density of states. As the in zeolites the incoherent cross-section of the H atom is very high in comparison to those values of Al, Si and O atoms, the main contribution to the VDOS would be caused by the vibrational movement of H atoms and the expression for the vibrational density of states can be approximated as VDOS ~ $g_H(\omega)$, where $g_H(\omega)$ is the hydrogen partial density of states.

2.1.5.5 INS spectrum

As it was mentioned in the subsection 2.1.5.4, GDOS can be directly extracted from the data obtained by Lagrange spectrometer. By using INS it is possible to measure all the

vibrational modes as the INS spectrum can be obtained in the wide range of energies which comes from the kinematic range of spectrometer and this is equivalent to the energy transfer in the region from 0 to 4000 cm^{-1}, therefore, the spectra can access bands that are inactive when using other spectroscopic techniques. **Figure 16** compares the INS, Raman and IR spectra of N-phenylsuccinimide (its molecular structure is also presented in the **Figure 16**) [77].

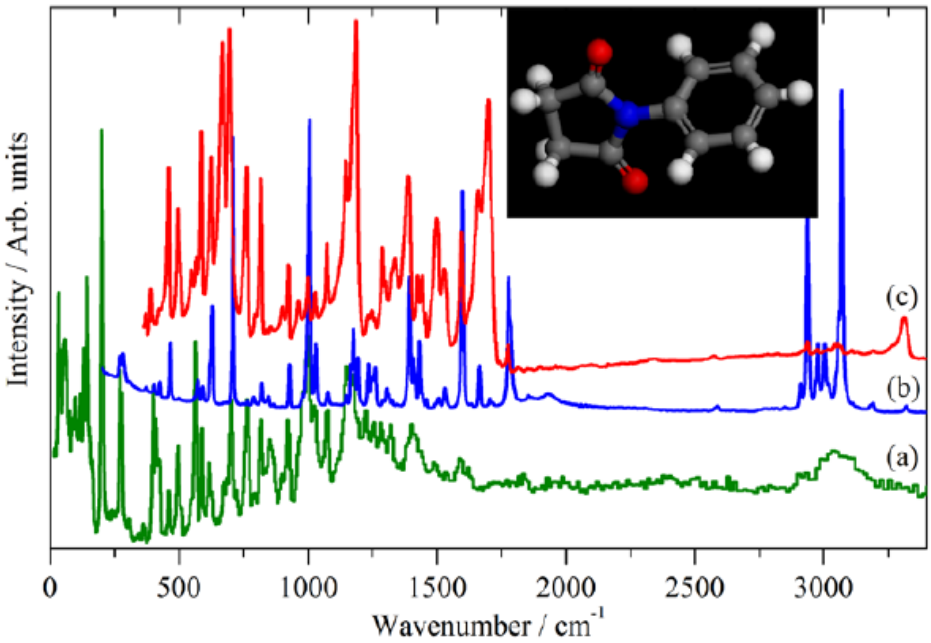

taken from [77]

Figure 16. Vibrational spectra of N -phenylsuccinimide: (a) INS, (b) Raman and (c) IR

For instance, the peak found at 407 cm^{-1} that corresponds to the out-of-plane bending is strong in the INS and week in Raman and absent IR spectra.

If we recall the expression of the Scattering law the INS spectra can be defined as GDOS $\sim S(Q, \omega_j)_i^n \sim \sigma_i \frac{(Q\ U_i)^{2n}}{n!} \exp[-Q\ U_{tot}]^2$.

This equation consists of 2 main terms: the pre-exponential and exponential factors.

• The first term depends on the momentum transfer and individual atomic displacements. Due to the fact that the momentum transfer is constant for all the atoms, this term allows to extract the eigenvectors of each of the atomic displacements.

• The second term is called the Debye-Waller factor [78]. It depends on the sum of the atomic displacements of all the atoms in the system and on the momentum transfer. The influence of the Debye-Waller factor should be reduced as it cases difficulties in the interpretation of the vibrational spectra. It can be achieved by reducing one of the variables, either Q or U. The value of U characterizes the thermal motion of the atoms in the investigated system. Thus samples should always be studied at cryogenic temperatures as it decreases the thermal movement of the atoms. Another term that contributes to the value of the Debye-Waller factor is the momentum transfer **Q**. Since in case of Lagrange spectrometer this value is high (see **Figure 13**), the vibrational bands in the high energy region are overlapped. Thus, **Figure 17** shows the diagrammatic representation of the value of the scattering law function S depending on the momentum transfer. As it can be seen, when **Q** is high the value of S is low and, therefore, the intensity of INS peaks is also low. At the same time with the increase of **Q** the influence of the Debye-Waller factor also increases.

This results in decrease of resolution of the peaks at high-frequency region of the spectrum. The interpretation of the INS spectra (assignment of the peaks) requires the application of additional techniques. One of the most frequent method is computational modeling. This method will be introduced in 2.2.

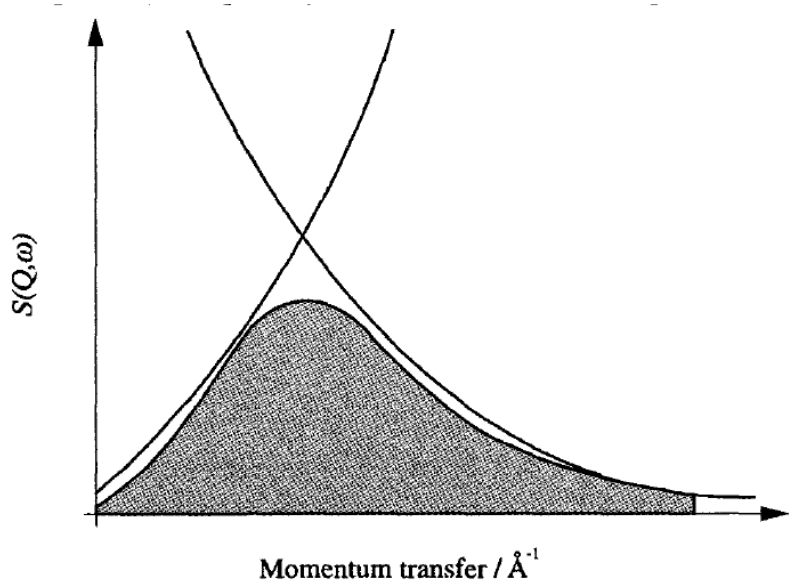

taken from [72]

Figure 17. Diagrammatic representation of the value of the scattering law function S, as it varies with momentum transfer Q, for a given vibrational mode, *v,* at an energy transfer of *a.* At low momentum values the intensity increase is driven by the pre-exponential factor but at high values of momentum the intensity is suppressed by the Debye-Waller factor

2.2 Computational methods

By using computational methods it is possible to calculate accurately both frequencies and intensities of INS spectra. In consequence this information can be used to assign the peaks of the experimental spectra which in its turn can be used in chemical and structural interpretations. The vibrations of a molecule (or crystal) are given by its normal modes and each peak in a vibrational spectrum corresponds to a normal mode. Thus, this subsection will give a short introduction to normal modes analysis and how it can be performed by a computational modeling. DFT and its relation with experimental vibrational methods will be also discussed, as well as programs that are used to proceed the computational outputs into a theoretical vibrational spectra.

2.2.1 Normal modes analysis of molecular vibrations

Crystals and molecules consist of atoms that are held together by interatomic forces. These atoms are permanently deviating from their equilibrium position, due to the consistent vibration induced by thermal energy.

For instance, there is a crystal that consists of N atoms. These atoms, before they bond, can move in three perpendicular, energy independent directions (represented by Cartesian coordinates x, y, z). The number of total degrees of freedom in such system is therefore 3N. This includes vibrational, translational and rotational degrees of freedom. In a non-linear molecule (or crystal) there are 3 rotational degrees of freedom around the x, y, z axes and 3 degrees of freedom corresponding to the translational motion of the center of the mass of the molecule along the x, y, z axes. The remaining 3N – 6 degrees of freedom are the internal vibrations of this atomic system. These vibrations define the total number of vibrational modes, or normal modes.

The superposition of normal modes can represent all possible atomic motions in the molecule or crystal and each peak in the fundamental vibrational spectrum corresponds to the certain normal mode. Both the classical and quantum chemical approaches can be applied in order to calculate the normal modes of the atomic system.

In the classical approach the Newton's equations of motion [79] is used. The motion of atoms in such systems can be calculated by using a simple harmonic approximation. In this case, the normal mode can be defined as a vibrational state in which atoms move in a simple harmonic motion around their equilibrium position and each mode acts like simple harmonic oscillator.

The motion of a single atom represented as a simple harmonic oscillator (one normal mode) is presented in **Figure 18**.

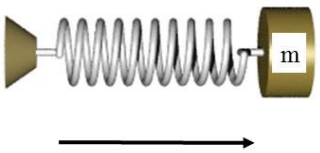

Figure 18. Schematic representation of the simple oscillator

Consider the mass m, which is supported on a spring with the force constant k. The equation of such a motion is described by Hook's law, which can be considered as a partial case of Newton's equation of motion. F= -kx, where x is displacement of the equilibrium position of m. The potential energy Hook's law is obtained by integrating

the following expression $-\frac{dV}{dx} = -kx$, so the value of the potential energy will be $V = \frac{1}{2} k x^2$. The value force constant k is not known, however it can be calculated from the expression of the second derivative of the potential energy:

$$k = \frac{d^2V}{dx^2}$$ **Equation 20**

If there is a system of N atoms, each of the vibrational movements of these atoms can be considered as a simple harmonic oscillator. Each atom can be move in 3 different directions (along the 3 coordinates x, y or z).

All of such atomic displacements has its own equation of motion and so its characteristic force constant. So in total there are 3Nx3N equations of motions and force constants correspondingly. For instance, $\frac{d^2V}{dx_1{}^2} = k_{xx}^{11}$ is the force constant which characterizes the change of the force on atom 1 in the x-direction, when the atom 1 is moved in the x-direction; and $\frac{d^2V}{dx_1 dy_2} = k_{xy}^{12}$ is the change of the force on atom 1 in the x-direction when the atom 2 is moved in the y-directions, etc.

The complete list of these force constants is called the Heissian matrix and its dimension is 3Nx3N, and its expression can be written as the following [80, 81]:

$$H = \begin{pmatrix} k_{xx}^{11} & k_{xy}^{11} & k_{xz}^{11} & k_{xx}^{12} & k_{xy}^{12} & \cdots & k_{xz}^{1N} \\ k_{yx}^{11} & k_{yy}^{11} & k_{yz}^{11} & k_{yx}^{12} & k_{yy}^{12} & \cdots & k_{yz}^{1N} \\ \vdots & & & & & & \\ k_{xx}^{21} & k_{xy}^{21} & k_{xz}^{21} & k_{xx}^{22} & k_{xy}^{22} & \cdots & k_{xz}^{2N} \\ \vdots & & & & & & \\ k_{zx}^{N1} & k_{zy}^{N1} & k_{zz}^{N1} & k_{zx}^{N2} & k_{zy}^{N2} & \cdots & k_{xz}^{NN} \end{pmatrix}$$ **Equation 21**

Or in terms of potential energy:

$$H = \begin{pmatrix} \frac{d^2V}{dx_1^2} & \frac{d^2V}{dx_1 dy_2} & \dots\dots\dots & \frac{d^2V}{dx_1 dz_N} \\ \frac{d^2V}{dy_1 dx_1} & \frac{d^2V}{dy_1^2} & \dots\dots\dots & \frac{d^2V}{dy_1 dz_N} \\ . & . & & . \\ . & . & & . \\ . & . & & . \\ \frac{d^2V}{dz_N dx_1} & \frac{d^2V}{dz_N dy_1} & \dots\dots\dots & \frac{d^2V}{dz_N^2} \end{pmatrix} \quad \textbf{Equation 22}$$

The diagonalization of the Heissian matrix gives 6 eigenvalues that correspond to translations and rotations of the center of mass and 3N-6 eigenvalues that correspond to vibrational modes.

In the quantum mechanical representation of the **Equation 22**, the argument that corresponds to the potential energy V is substituted by the corresponding wavefunction. Hence, the resulting Heissian matrix would define the Hamiltonian operator $\hat{H}$, which corresponds to the total energy of the atomic system and it can be calculated by quantum chemical methods. The following subsection is devoted to Schrödinger equation which is the basis of quantum mechanics.

2.2.2 Schrödinger equation

The goal of most approaches in quantum chemistry is the solution of the time-independent, non-relativistic Schrödinger equation. As it is impossible to find the exact solution of this equation, in quantum chemistry exist different approximations (methods) of this equation which can be solved numerically. This section is dedicated to Density Functional Theory (DFT) method, as the theoretical results of this thesis have been obtained by this method.

The Schrödinger equation for a system that contains M nuclei and N electrons can be written as the following [82]:

$$\hat{H}\Psi_i(\mathbf{x_1}, \mathbf{x_2}, ..., \mathbf{x_N}, \mathbf{R_1}, \mathbf{R_2}, \ldots, \mathbf{R_M}) = E_i\Psi_i(\mathbf{x_1}, \mathbf{x_2}, ..., \mathbf{x_N}, \mathbf{R_1}, \mathbf{R_2}, \ldots, \mathbf{R_M}),$$

Equation 23

Where Ψ_i is a wavefunction, a fundamental concept of quantum chemistry and it fully describes the state of the system at the current moment of time or the probability of finding the particle in the particular point of space at the given moment of time.

The Hamiltonian operator ($\hat{H}$), corresponding to the total energy is defined by the following:

$$\hat{H} = -E_e - E_n - V_{e\,n} + V_{e\,e} + V_{n\,n}$$

Equation 24

In this expression the first two terms describe the kinetic energy of the electrons and nuclei. The other three terms represent the attractive electrostatic interaction between the

nuclei and the electrons and potential energy of the repulsive electrostatic electron-electron and nucleus-nucleus interactions respectively.

2.2.3 Basic theorem and equation in Density Functional Theory

The Schrödinger equation contains a wavefunction as the central quantity, since it represents the full information of the investigated system. However, wavefunction is a very complicated quantity and it cannot be measured experimentally and it depends on a high number of variables: $3*N_{(electrons)}$ spatial and 1*N spin coordinates. This, in the systems that contain many atoms and many more electrons, becomes a very complicated problem. DFT is another approach that is able to define properties of the electronic system without solving the Schrödinger equation. The main advantage of DFT is that it is not necessary to know the wavefunction of each electron, all the properties of the system are defined by the density of probability of finding electron in the particular point of space. This magnitude is called, electron density ($\rho(r)$) and it is a central quantity of DFT method and, unlike wavefunction, electron density is a function of only 3 coordinates. Furthermore, DFT is one of the most successful and promising approaches to compute electronic structure of matter and it can predict a great variety of molecular properties such as molecular structures, vibrational frequencies, atomization energies, ionization energies, electric and magnetic properties, reaction paths, etc. The electron density is defined as the integral over the spin coordinates of all electrons and over all but one of the spatial variables. The position and spin of the electron can be combined in one vector $\mathbf{x}(\mathbf{r_i}; \sigma_i)$, where $\mathbf{r_i}$ is the position and σ_i is the spin of a given electron i correspondingly.

The relation between the electron density and the many-electron wavefunction can be represented as the following [83]:

$$\rho(r) = N \int \dots \int |\psi(\mathbf{x_1}, \mathbf{x_2}, \dots, \mathbf{x_N})|^2 \, d\sigma_1 \, d\mathbf{x_2} \dots d\mathbf{x_N}$$ **Equation 25**

In 1964 Hohenberg and Kohn have published a work dedicated to DFT [84]. The publication introduced two theorems that now represent the major theoretical basis of DFT. The first theorem states that the electron density of any system determines all ground-state properties of the system. The second theorem states that the total energy of the ground state of the system is a functional of the ground state electron density. A functional is defined as an object that acts on a function to produce a scalar.

The equation of motion in DFT is called Kohn – Sham equation and it can be represented as the effective one-electron-type Schrödinger equation:

$$E[\rho] = T_s[\rho] + \int d\boldsymbol{r}\, v_{ext}(\boldsymbol{r})\, \rho(\boldsymbol{r}) + E_H[\rho] + E_{xc}[\rho]$$ **Equation 26**

In **Equation 26** the term $E[\rho]$ represents a total energy of the system in ground state and it is a functional of electron density. Similar to the many-body Schrödinger equation, Kohn – Sham equation contains the first term that represents the kinetic energy of the electronic movement, the second term states for the nuclei-electron interaction, $E_H[\rho]$ is a Colomb energy attributed to the electron repulsion and the last term is exchange correlation energy and it describes the exchange and correlation effects of the system. It is possible to calculate first 3 terms of the Kohn – Sham equation, however it is not possible to find the exact value of the exchange correlation energy.

2.2.4 Exchange-correlation functionals

The approximate value of the exchange correlation energy can be calculated by using one of the approximations, which are called exchange-correlation functionals.

Exchange correlation energy contains both terms: the energy of exchange and the energy of correlation effects in the electronic system, and it can be described by the following expression:

$$E_{xc}[\rho] = E_x[\rho(\mathbf{r})] + E_c[\rho(\mathbf{r})] \quad \textbf{Equation 27}$$

Electronic correlation can be defined as the interaction between electrons in the electronic structure of a quantum system. The correlation energy ($E_c[\rho(r)]$) is a measure of how much the movement of one electron is influenced by the presence of all other electrons.

The exchange energy ($E_x[\rho(r)]$), is the energy released when two or more electrons with the same spin exchange their positions in the orbitals of the same energy level.

The basic approximation that has been done by Kohn and Sham is a Local Density Approximation (LDA) [85]. This approximation is based on the assumption that electrons are distributed along the system in a homogeneous way, so the value of the electron density does not change in any point of the system. In this case the expression of the exchange-correlation energy can be written as the following:

$$E_{xc}^{LDA}[\rho] = \int \rho(\mathbf{r})(\varepsilon_x[\rho(\mathbf{r})] + \varepsilon_c[\rho(\mathbf{r})])d\mathbf{r} \quad \textbf{Equation 28}$$

In **Equation 28** the term $\rho(\mathbf{r})$ represents the electron density (electrons per unit of volume), $\varepsilon_x[\rho(\mathbf{r})]$ and $\varepsilon_c[\rho(\mathbf{r})]$ are exchange and correlation energy density (energy per electron).

Local density approximation includes the set of different functionals that use different approach to calculate $\varepsilon_x[\rho(\mathbf{r})]$ and $\varepsilon_c[\rho(\mathbf{r})]$. For instance, one of the LDA functionals, Vosko, Wilk and Nusair (VWN) functional calculates the value of $\varepsilon_c[\rho(\mathbf{r})]$ analytically by using specific fitting parameters [86].

Nowadays, most of the systems studied computationally are not homogeneous, therefore the electron density in such materials is not homogeneous and these systems can't be described by LDA with enough precision. Hence, functionals with another dependence for the electron density are required.

In order to take into account the non-homogeneity of real electron density, the term $\rho(\mathbf{r})$ that describes the information about the electron density in the particular point of space **r** should be substituted by the term that gives the information about the gradient of the electron density. Such approach is called Generalized Density Approximation (GGA) and it has been introduced in studies of Hohenberg and Kohn [84] and Kohn and Sham [85].

The expression for the exchange-correlation energy in GGA can be presented as the following:

$$E_{xc}^{GGA}[\rho_\alpha, \rho_\beta] = \int f(\rho_\alpha(\mathbf{r}), \rho_\beta(\mathbf{r}), \nabla\rho_\alpha(\mathbf{r}), \nabla\rho_\beta(\mathbf{r}))$$ **Equation 29**

Usually, the typical GAA functionals are based on a set of fitting parameters, which usually belong to two different types of fitting parameters: the first one satisfies known properties of exchange correlation energy, the second type of parameters fits the exchange-correlation energy to a large data set of the investigated systems (such as exactly known binding energies of atoms and molecules, etc.).

The choice of the convenient functional can be challenging, and, it's usually based on the previous experience of the scientist working with the particular type of systems.

The exchange-correlation functional, typically used in study of zeolites is PBE, has been introduced by Perdew, Burke and Erzenhof [87, 88]. PBE functional is the algorithm for calculation the exchange-correlation energy on base of certain physical constrains of the investigated system and does not contain adjustable parameters. PBE was designed to replace the PW91 functional. For most purposes, it should yield energies very close to those of PW91. Nevertheless, the derivation and analytic form have been simplified, and some spurious wiggles in the exchange-correlation potential have been eliminated [89]. PBE functional is known for its general applicability and gives rather accurate results for a wide range of systems. In particular, there is a number of studies of zeolite performed with PBE, some of them have been already mentioned above [47, 51].

PBEsol functional is intended to improve PBE for equilibrium properties such as bond lengths and lattice parameters, but typically is worse for dissociation or cohesive energies [90]. This functional was created for solid state and surface systems. It is based on a gradient expansion of the exchange energy and a final fit of the exchange-correlation energy to that of surface uniform electron gas. It takes into account the interaction of fluctuating charge distributions in one particle with those in an adjacent particle. This allows to obtain accurate exchange energy and cell parameters. In our study we also included dispersion corrections throughout the TS scheme, which was introduced by

Tkatchenko and Scheffler [91]. It employs a pairwise dispersion correction method introduced by Al-Saidi et al. [92]. The DFT/PBEsol with dispersion correction method has been recently used in the study of microporous non-ionic silicate crystals [93]. It has been shown an excellent prediction of the lattice parameters which are found to be in a good agreement with experimental data.

In our study we also applied another type of GGA functional, called HCTH [94]. Within this approximation the calculation of the exchange-correlation energy is based on a set of different experimental data used as fitting parameters. These data includes, for instance, total energies of atoms and atomization energies, ionization potentials, electron affinities and dissociation energies measured for a number of molecules and ions [95]. The fitting is based on the Becke's procedure [96], which uses only one fitting parameter that allows to find the accurate contribution of the exchange effects, also energy gradient and exchange-correlation potentials included in the data. This in terns helps to generate the accurate structures.

The result of a quantum-chemical calculations is a total energy of the atomic system. This magnitude defines the Hessian matrix presented by **Equation 22**, which in its turn is used to obtain the normal modes of the system.

2.2.5 DFT codes

Several codes can be applied in order to perform a DFT calculation. In this study we used two different DFT codes: DMol3 and CASTEP implemented into MaterialsStudio software [97].

DMol3 is a modelling program that uses DFT to simulate different chemical systems and processes [98]. Initially designed for molecules, its application has been extended for

crystals by idealizing to solid for perfect translation symmetry with respect to the unit cell. DMol3 achieves its speed and accuracy by using localized numerical orbitals as a set of atomic basis functions. This atomic basis functions are obtained by solving DFT equations for individual atoms. In DMol3 the electron density is presented by multipolar, atomic-centered partial densities. This allows to achieve compact and yet accurate representation of the electron density. The main advantage of DMol3 is its speed, as an efficient geometry optimization algorithm lets you predict minimum energy structures rapidly.

CASTEP is a DFT code designed for performing quantum mechanical calculations based on using plane-wave pseudopotential approach [99] in order to solve a set of one-electron Kohn-Sham equations. In this case the periodic boundary conditions are defined by Bloch's theorem, which states that each electronic wavefunction can be represented by a set of plane-wave functions. The electron–ion potential is described by means of ab initio pseudopotentials within either norm-conserving [100] or ultrasoft [101] formulations. CASTEP can be used to simulate a wide range of different materials from molecules and liquids to surfaces and crystalline solids. Moreover, it is able to predict a variety of different properties of any material such as phonon density of states, IR and Raman spectra, etc. The only limitation of such calculation is finite speed and memory of the computers being used.

One of the disadvantages of DMol3 over CASTEP is that it provides inefficient cell optimization procedure which consists in a set of parallel optimization processes requiring high computational cost. Therefore, DMol3 is efficient in studies of the systems which initial models have cell parameters similar to experimental, in this case the calculations can be performed without cell optimization procedure. Otherwise, CASTEP program should be used.

2.2.6 Selection of calculation parameters

The basis functions (or basis set is a set of functions mentioned above) are used to represent the electronic wave function in DFT in order to turn the partial differential equations of the model into algebraic equations suitable for efficient implementation on a computer.

Within this thesis, the double numerical plus-d-function basis set (DND (all-electrons basis) used in DMol3 module have been applied for the study of LTA-40. The DND basis set includes one numerical function for each occupied atomic orbital and a second set of functions for valence atomic orbitals, plus a polarization d-function on all atoms.

CASTEP code have been used for the study of LTA-5. In CASTEP the basis set is defined by the energy cutoff value which is one of the most important parameters that determine the accuracy (and the cost) of a CASTEP calculation. In our calculations this value has been set to 500 eV.

In this work the electronic properties were calculated for the Gamma-point (the point of the highest symmetry in the Brillouin zone) in order to lower a computational cost of the calculations.

Finally, in case of both DMol3 and CASTEP calculations, the overall procedure can be presented as consisting in the following two steps: 1) as the result of the geometry optimization the equilibrium geometry was obtained; 2) vibrational calculations were subsequently performed to obtain the frequencies of the normal modes of the system by diagonalization of the Hessian dynamical matrix already discussed above. These data is obtained in a computational output. In order to obtain the theoretical GDOS (see ‘the sections ‘Scattering law’ and ‘INS spectrum’) the specific software should be applied.

2.2.7 Mantid and aCLIMAX software

Mantid [102] and aCLIMAX [103] are the programs that are usually used in order to obtain the theoretical GDOS (and, therefore, the graphical representation of the calculated INS spectra) from the output obtained by quantum-chemical frequency calculations.

The intensities of the calculated INS spectra can be calculated from the Scattering law represented by the equation (18). In this expression the value of n represents the order of the excitation of the nucleus by the energy given by the scattered neutron. The n=1 corresponds to the intensity of the fundamental transition. In INS not only fundamentaltransitions are observed, the excitations of a higher are also present, such as the excitations of the same vibration. For instance, the n=2 corresponds to the first overtone, this peak is found at the double frequency of the corresponding peak of fundamental vibration and its intensity is lower than those of fundamental. The n=3 corresponds to the second overtone, the n=4 to the third and so on. When the single excitation of more than one vibration occurs, such excitations are called combinations. Finally, the vibrations that correspond to the excitations of the external vibrational modes (lattice vibrations) with the internal vibrational modes are called phonon wings. They are always present in the spectra and their strengths depend on many different factors [104]. As the nature of phonon wings is complicated, within this work we will not take them into account in INS spectral analysis.

In order to interpret experimental INS spectra aCLIMAX requires the output of the computational modeling frequency calculations, which provides the eigenvalues (frequencies) and corresponding eigenvectors (atomic displacements) of the investigated system. In this thesis it has been used an output obtained by DMol3 calculations (with extension .outmol) which is compatible with aCLIMAX software. Within the study of

LTA-40, aCLIMAX has been used to produce the theoretical INS spectra, including fundamental vibrations and first overtone.

In case of Mantid, the program used is 'Abins', which allows to calculate the theoretical INS spectra. Abins requires a file with the ab initio phonon data to perform INS analysis. In this thesis it has been used CASTEP output files (with extension .phonon) for the study of LTA-5. It has been generated a total theoretical spectrum for the whole considered system which is a sum over all considered quantum events for that atom, which may include fundamental vibrations (event 1), first overtone with fundamentals and second order combinations (event 2), first and second overtones with fundamentals and second and third order combinations (event 3), etc.

2.3 Nuclear Magnetic Resonance Spectroscopy

Solid state NMR spectroscopy is a very powerful technique for obtaining structural information in study of zeolites. Moreover, the use of 'in situ' methods allows to determine physical and chemical properties of reaction intermediates in heterogeneous processes catalyzed by solids.

This method was used in this study as a complementary in order to interpret the INS experimental and DFT computational results.

2.3.1 Basic principles of NMR

The effect of NMR can be described by a simple classical model. In this case an atomic nucleus is represented as the rotating positively charged ball with the circular orbit (see **Figure 19**) [105].

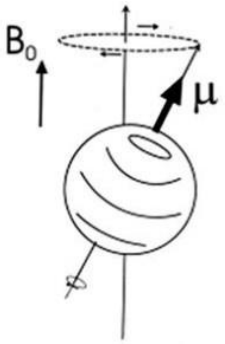

taken form [105]

Figure 19. Atomic nucleus represented as a rotating ball with circular orbit

Such a movement induces a circular electric current, which in turns induces magnetic field, then, this nucleus can be considered as microscopic magnet, which has its own characteristic angular momentum of spin (**P**) and nuclear magnetic moment (**μ**) and it is directed along the axis of rotation. The angular momentum is proportional to the magnetic moment, this relation is represented by the following $\boldsymbol{\mu} = \gamma \mathbf{P}$, where γ is a constant of proportionality called gyromagnetic ratio. This magnitude is characteristic for each type of nuclei, for instance, it is $2.675 * 10^{-8}$ $rad \cdot s^{-1} \cdot T^{-1}$ for ^{1}H and $0.673 * 10^{-8}$ $rad \cdot s^{-1} \cdot T^{-1}$ for ^{13}C nuclei [106].

The angular momentum and magnetic moment are quantized. That means that this magnitude may only have particular values. The allowed values of the projection of the angular momentum P_z on the axis of the turning movement can be calculated as:

$$P_z = \frac{h}{2\pi} m_I \qquad \textbf{Equation 30}$$

Where m_I is the quantum magnetic number and h is the Planck constant.

M_I can be of the following values: I, I-1; … -I, i.e. it can be one of the 2I-1 spins states, where I is the spin quantum number and it is a characteristic property of a nucleus.

If I=1/2 then there are 2 possible spin states (+1/2 and -1/2);

If I=1 then there are 3 possible spin states (-1, 0, 1);

If I=3/2 then there are 4 possible spin states (-3/2, -1/2, +1/2, +3/2).

All the nuclei with the odd mass numbers and nuclei which has odd numbers of protons and neutrons has the magnetic moment ($I \neq 0$). In the first case I has half-integer value (i.e. ½, 3/2, 5/2…) and in the second case it has integer values (1, 2, 3…).

For instance, nuclei such as ^{1}H, ^{13}C, ^{19}F, ^{31}P, ^{15}N has a spin number equal ½. The nuclei ^{11}B, ^{35}Cl, ^{79}Br, and ^{81}Br have a spin number -3/2 [106].

In the absence of an external magnetic field spin states are degenerated in energy. When the nucleus is subjected to an external magnetic field with strength B_0, the degeneration is eliminated. The nuclei with magnetic moments directed along and contrary the external magnetic have different energy and the transition from one energy level to another energy level may occur (see **Figure 20**), when it is related with the frequency

such that $\gamma = \nu / B_0$, where ν is a frequency of photon absorbed by nucleus and γ is gyromagnetic ratio of such nucleus.

This process can be described as follows: a nucleus in the lower energy state absorbs a photon and ends up in the upper energy state. The energy of this photon must exactly match the energy difference between the two states. The energy, E, of a photon is related to its frequency, ν, by Planck's constant $E = h \nu$.

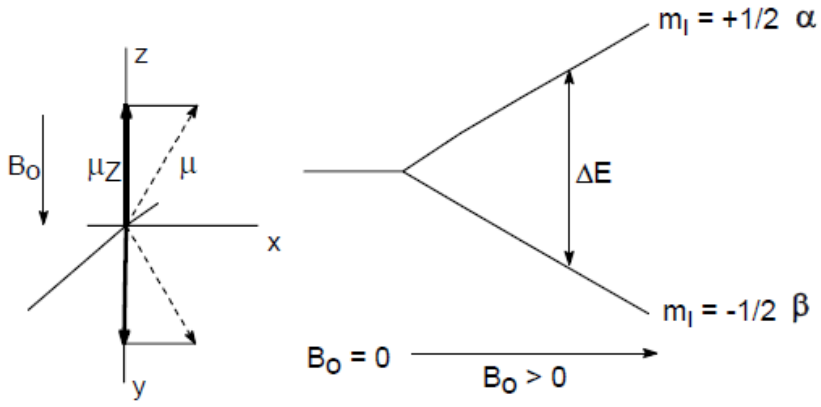

taken from [105]

Figure 20. Splitting of the energy levels of nucleus in the external magnetic field

This transition is the physical origin of the Nuclear Magnetic Resonance spectroscopy which is based on the absorption of the magnetic radiation by the nuclei of the sample introduced into the magnetic field. Thus, the simple representation of a NMR experiment is the following: a sample is introduced into the magnetic field and it is irradiated with the electromagnetic radiation with the frequency ν that depends on B_0. The nuclei of the

investigating sample are precessing (i.e. changing the orientation of their rotational axis) with frequency ν_0. The absorption of energy is observed at when $\nu=\nu_0$. Then, by applying Fourier transform the signal that appears after such a transition is converted to NMR peak.

As it was mentioned above, the gyromagnetic ratio of the nucleus is a constant magnitude. In ideal case while registering the NMR spectrum of a given type of nucleus, the unique signal is observed. Nevertheless, in real molecules the nuclei undergo not only the impact of the external magnetic field but also the electromagnetic field of the nuclei in its closest environment and the molecule itself. In other words, the diamagnetic shielding occurs. As a result the resonance signal of a given nucleus occurs in at a frequency different from those of isolated nucleus.

Depending on the rate of shielding each considered nucleus of the investigated molecule would absorb the electromagnetic radiation at certain frequency, which in turn depends on the chemical environment of the considered nucleus. Such change of the resonance frequency is called the chemical shift (δ) [107].

The γ at which the NMR signals appear depends on the frequency of the external magnetic field B_0 and then it depends on the instrument. Then, it is necessary to introduce the unique relative scale (δ-scale) measured in ppm (parts-per-million, 10^{-6}). The signal of protons in tetramethylsilan ($Si(CH_3)_4$) is accepted as 0, and the relative chemical shift is calculated as:

$$\delta = (\nu_{sample} - \nu_{Si(CH_3)_4}) / \nu_{instrument} \qquad \textbf{Equation 30}$$

For instance, in an instrument of 400 MHz the difference between the absorption frequencies of the protons in tetramethylsilan and investigated sample would be 800 Hz, then the value of the chemical shift of these protons is calculated $\frac{800}{400*10^6}$ = 2 ppm.

In the present work we applied solid-state ^{29}Si MAS (Magic angle spinning) NMR spectroscopy as a complementary tool in study of distribution of aluminium atoms in LTA-5.

2.3.2 Magic Angle Spinning

In solid-state NMR the samples are usually represented in a powder form,in such systems the nuclei experience anisotropic interactions, which broaden the NMR signal preventing the observation of the signals corresponding to different species. Some of these effects can be partially suppressed by introducing an artificial movement of the sample by rotating it around an axis which forms the angle equal to 54°44′ with the external magnetic field. This angle is called 'magic angle'.

This method is known as Magic Angle Spinning [108]. However, this method only works when the sample is spinning at the frequency comparable with the widths of the line which can be tens or hundreds kHz. Nowadays, MAS NMR probes usually can spin the sample at around 40 kHz.

2.3.3 Cross polarization (CP) method

In the present work we used cross polarization method to obtain the peaks with higher intensity and to identify nuclei close to ^{1}H.

In case of measurements done on low abundant nuclei such as ^{29}Si, ^{13}C, ^{15}N etc. the signal/noise ratio is small. In order to strengthen the signal of such nuclei it is applied cross polarization. This experiment is based on ther magnetization transfer from nuclei with high polarization (usually, ^{1}H) to nuclei with low polarization through the dipole-dipole interaction, which causes the increase of intensity of the signal and so increase of the signal/noise ratio [109].

2.3.4 NMR in study of zeolites

Solid-state NMR is widely used in characterization of zeolites, as they contain a number of the active nuclei such as ^{29}Si, ^{27}Al and ^{1}H.

Examples of ^{29}Si and ^{27}Al MAS NMR spectra of zeolites are shown in **Figures 21** and **22** respectively [110].

^{29}Si MAS NMR provides information about the local environment of each silicon atom in the zeolite framework. These atoms are connected to other silicon or aluminium atoms via oxygen bridges. The types of silicon atoms are defined as Qn , where n is the number of silicon in the first coordination sphere through the oxygen.

The peak located at around -112 ppm is attributed to the silicon atoms which have 4 other Si atoms in their coordination sphere. The peak found at -107 ppm corresponds to the silicon atoms with 1 Al and 3 other Si atoms in their neighboring coordination sphere and so on, up to the peak located at around -90 ppm corresponding to silicon atoms of Q0 type with 0 Si and 4 Al atoms. The spectrum shown in Figure 2 corresponds to a LTA type zeolite with Si/Al ratio 2, this means that the aluminium content in this samples is very high. In this spectrum the peaks corresponding to Q0 and Q1 are relatively intense. However, since the content of aluminium atoms is relatively low, the peak corresponding to the Q_0 is either absent at all or its intensity is very low, and the peak corresponding to

Q4 is more intense in comparison to other peaks.

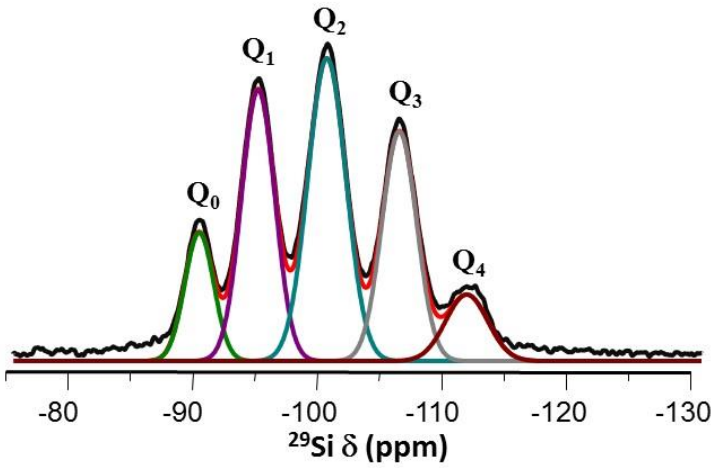

taken from [110]

Figure 21. ^{29}Si MAS NMR spectra of LTA-2 zeolite

Figure 22 shows the ^{27}Al MAS NMR spectra of samples of two LTA zeolites with Si/Al ratio 2 and 5. The chemical shifts are broadened due to the quadrupolar nature of ^{27}Al nuclei, but their position provides important information about the coordination state of aluminium atoms. Aluminium atoms located in the framework of the zeolite has a coordination number 4 (i. e. it is tetrahedrally coordinated) and its chemical shift is found in the region from 50 to 65 ppm depending on the environment.

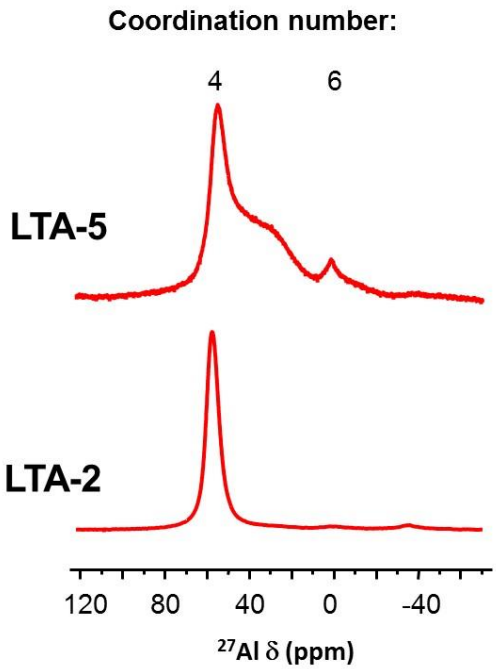

taken from [110]

Figure 22. ^{27}Al MAS NMR spectra of LTA-5 and LTA-2 zeolites

The atoms with octahedral coordination (i. e. coordination number 6) appear at the chemical shift is found at around 0 ppm. As it can be seen from the spectra shown in **Figure 21**, the sample of LTA-2 doesn't contain any impurities related to the presence of extra-framework aluminium atoms and the spectrum consists one peak that corresponds to tetrahedrally coordinated aluminium atoms, while the spectrum measured for the sample of LTA-5 contains also the peak at around 0 ppm with relatively small intensity. This means that the sample of LTA-5 contains low amount of extra-framework aluminium atoms.

2.3.5 Experimental details of NMR experiments

In the present work solid-state MAS NMR spectra were recorded with a Bruker AV 400 WB spectrometer. The samples of LTA with Si/Al ratio 5 and 40 have been previously dehydrated at 400° C and encapsulated in vacuum into the glass inserts. Then, the glass inserts were fitted into 7 mm rotors and were spun at 5 kHz in a Bruker BL7 probe. The data acquired on the AV400 NMR spectrometer were automatically transferred to a special NMR data server. The spectra were referred to tetramethylsilane (TMS) and were simulated with the DMFIT program that is designed to help in viewing the NMR spectra, including solid state NMR [111].

In case of ^{29}Si NMR measurements the relative populations of the Si(nSi) environments expressed in % were determined from the areas of the individual peaks used in the simulation of the experimental ^{29}Si spectrum.

Then, the Si/Al framework ratio of the zeolites was calculated using the expression:

$\frac{\mathrm{Si}}{\mathrm{Al}} = \frac{\sum_{n=0}^{n=4} I_{Si(nAl)}}{\sum_{n=0}^{n=4} \frac{n}{4} I_{Si(nAl)}}$, where n is a number of aluminium atoms, $I_{Si(nAl)}$ is the area of the peak corresponding to Si with n Al atoms in its neighboring coordination sphere.

2.4 Preparation of samples

The samples studied in this thesis have been synthesized by Susana Valencia from the Instituto de Tecnología Química U.P.V.-C.S.I.C. Universidad Politecnica de Valencia (Spain).

Since neutron scattering experiments require a use of samples with high level of purity, a special synthesis strategy has been applied to produce the samples of LTA-40 and LTA-5 studied in this thesis.

2.4.1 Synthesis of LTA-40

First, the Organic Structure Directing Agent (OSDA) used in this synthesis was obtained by direct amine quaternization of the commercially available julolidine: 2,3,6,7-tetrahydro-1H,5H-benzo[ij]quinolizine, from Sigma-Aldrich, using methyl-iodide as alkylating agent, yielding to 4-methyl-2,3,6,7-tetrahydro-1H,5H-pirido[3,2,1-ij]quinolinium as iodide salt. Then, this was transformed into the hydroxide form by contacting an aqueous solution with a strong anionic SBR resin for 12 h at room temperature under continuous gentle mechanical stirring. The LTA-40 zeolites was synthesized in fluoride medium from a gel with the following composition:

$SiO_2 : 0.01Al_2O_3 : 0.25OSDAOH : 0.25TMAOH : 0.5HF : 3H_2O$,

where OSDAOH is 4-methyl-2,3,6,7-tetrahydro-1H,5H-pirido-[3,2,1-ij] quinolinium hydroxide, TMAOH is tetramethylammonium hydroxide (25 wt % aqueous solution from Sigma- Aldrich). The gel was prepared by hydrolyzing tetraethylorthosilicate (TEOS, from Merck) in an aqueous solution of OSDAOH and TMAOH. Then the appropriate amount of aluminum isopropoxide (AIP, from Sigma-Aldrich) was added and the mixture was kept under stirring until the ethanol and 2- propanol formed upon hydrolysis of TEOS and AIP and the appropriate excess of water were evaporated to reach the gel composition given above. After that, an aqueous solution of HF (50%) was added and, finally, the seeds were incorporated as a suspension of pure silica LTA zeolite (ITQ-29) in water to reach 15% of the total silica. The mixture was introduced in a Teflon-lined stainless autoclave and heated at 125 °C for 3 days under rotation at 60 rpm.

After this time, the autoclave was cooled down, and the mixture was filtered, washed with water, dried at 100 °C, and finally calcined under air at 973 K. The resulting solid was identified as pure zeolite LTA by means of X-ray diffraction as it is shown in **Figure 23**.

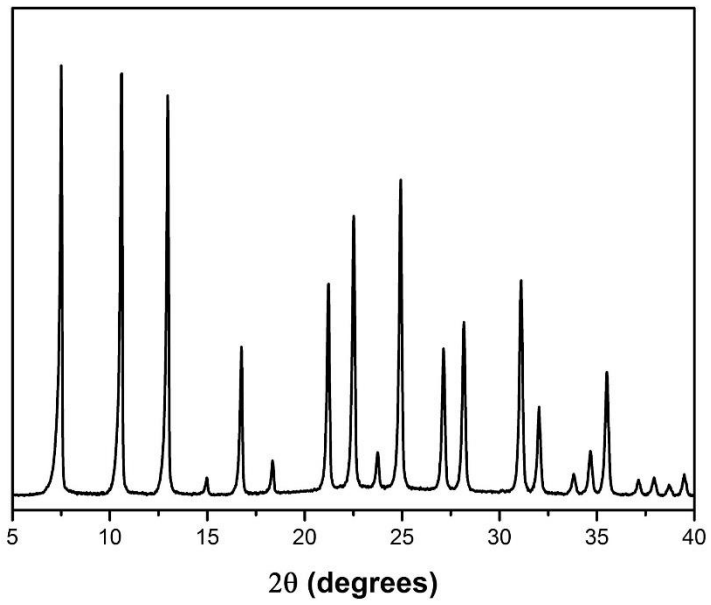

taken from [112]

Figure 23. XRD pattern of the calcined LTA-40 sample

Then, it was concluded that, by applying the synthesis strategy explained above, it has been synthesized a highly crystalline zeolite sample of LTA with a Si/Al close to 40 without defects in its structure, well suited for neutron scattering studies.

2.4.2 Synthesis of LTA-5

LTA zeolite with Si/Al ratio of 5 was synthesized according to the procedure described previously [113] using colloidal silica (Ludox AS-40) as the source of silica, Al sec-butoxide as the aluminium source and diethyl-dimethylammonium (DEDMAOH), tetraethylammonium (TEAOH), and tetramethylammonium (TMACl) as organic structure directing agents from a gel of the following composition:

SiO_2: 0.05 Al_2O_3: 0.30 TEAOH: 0.20 DEDMAOH: 0.05 TMACl: 0.05 NaCl: 17 H_2O

The crystallization was carried out at 373 K for 20 days and the zeolite obtained was further calcined at 823 K for removing the occluded organic material. Finally, it was submitted twice to ion exchange treatments with NH_4Cl followed by calcination at 773 K in order to exchange the Na cations by protons. The integrity of the sample was checked by means of X-ray diffraction (**Figure 24)** and micropore volume and surface area determination. As can be seen in the figure, the structural integrity of the zeolite was preserved upon organic removal by calcination followed by ion exchange.

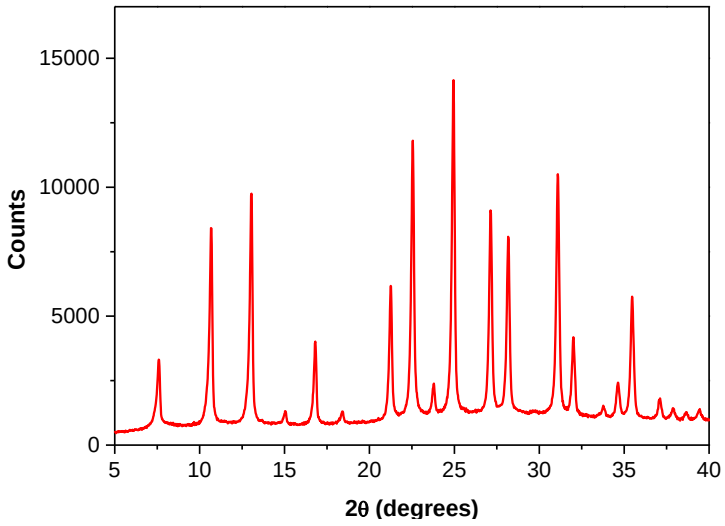

taken from [114]

Figure 24. X-ray diffraction pattern of the LTA-5 zeolite obtained after calcination and ionic exchange

On the other side, the micropore volume and surface area values obtained from the N_2 adsorption isotherm at 77 K measured in a Micromeritics ASAP 2010 instrument corresponded to 0.29 cm^3/g and 650 m^2/g, respectively, confirming the good crystallinity of the sample.

Finally, the chemical composition of the zeolite was determined by ICP on a Varian 715-ES ICP-Optical Emission Spectrometer giving a Si/Al ratio of 5.1 and no significant amount of Na was detected in the analysis.

Chapter 3

Inelastic Neutron Scattering Study on the Location of Brønsted Acid Sites in High Silica LTA Zeolite

This chapter is dedicated to the combine INS and computational study of Brønsted acidity in LTA-40 zeolite.

Proton containing zeolites are of a great interest for the catalysis and adsorption in both fundamental science and industrial application. It is known that the adsorptive and catalytic activity of zeolites depends on their acidity, which in turns depends on such

factors like the total number of acid sites, their individual strength, and their individual location.

Usually the location of acid sites in zeolites can be distinguished in two ways. Chemically, acid sites can be assigned as either Brønsted sites (≡Si-O(H)-Al≡) or terminal silanol goups (≡Si-OH). While structurally the acid sites can be distinguished either by the type of oxygen atoms to which this proton is attached (such types of oxygen atoms is called crystallographic position, usually indicated as OiH, where i=1, 2, 3…etc.) or by the mid-range environment such as the size of the cavity where the proton is located. For this study we chose LTA, since it has one of the simplest zeolite topologies which contain only three possible crystallographic positions (O1H, O2H and O3H) and only one possible crystallographic position of T atoms (T1), therefore in this zeolite may exist minimum possible locations of H atoms for such a Si/Al ratio.

The methods widely used in characterization of acidity of zeolites are IR and NMR spectroscopies (see 1.1). NMR technique allows to estimate the total number of acid sites, but it does not allow to assign unequivocally the location of each centre. On the other hand IR spectroscopy only gives information about stretching bands since bending modes (which are sensitive to local environment) of the acid sites overlap with strong bands of the zeolites framework.

Since, the goal of this study is to perform a structural analysis of LTA-40 in order establish in which crystallographic position the acid site are located, we applied an alternative approach based on the combination of the Inelastic neutron scattering with DFT periodic calculations.

We have shown that the combination of an extremely high quality of the sample and the sensitivity of the instrument together with periodic DFT calculations allows for the first time to detect with high precision the most favorable location of the acid sites in LTA-

40 containing only ½ of hydrogen atom per unit cell. Finally, with this study we show that the use of INS opens new possibilities for acid characterization of zeolite catalysts.

3.1 Computational models of LTA-40

LTA contains large (α-cage) cavities whose space is highlighted by violet sphere, and small (sodalite) cavities, which space is highlighted by red sphere (see **Figure 25 a)** and **b)**). It is one of the simplest zeolite frameworks, with a small unit cell and three crystallographically different oxygens, where O1H and O3H point to a 8T-ring at the intersection between two α-cages, while O2H points to a 6T-ring at the intersection between the α-cage and the sodalite cavity.

The unit cell of LTA has the formula $Si_{(24-x)}Al_xO_{48}H_x$. In order to have a Si/Al close to the experimental (Si/Al = 40), we performed calculations on a supercell 2×1×1, containing one isolated Brønsted site, this structure has a formula $Si_{47}AlO_{96}H$. The proton is bonded to either O1, O2 or O3 position such as O1H and O3H point toward the large cavity while O2H vibrates close to the small cavity. The resulting models will be called LTA_47_OxH (where x = 1−3). This gives a Si/Al ratio equal to 47 which is close to the experimental value. Therefore, we performed periodic DFT calculation on a double unit cell of LTA locating the proton either into O1H, O2H or O3H position. Furthermore, we compared calculated spectra with experimental INS spectrum measured for the sample of LTA-40.

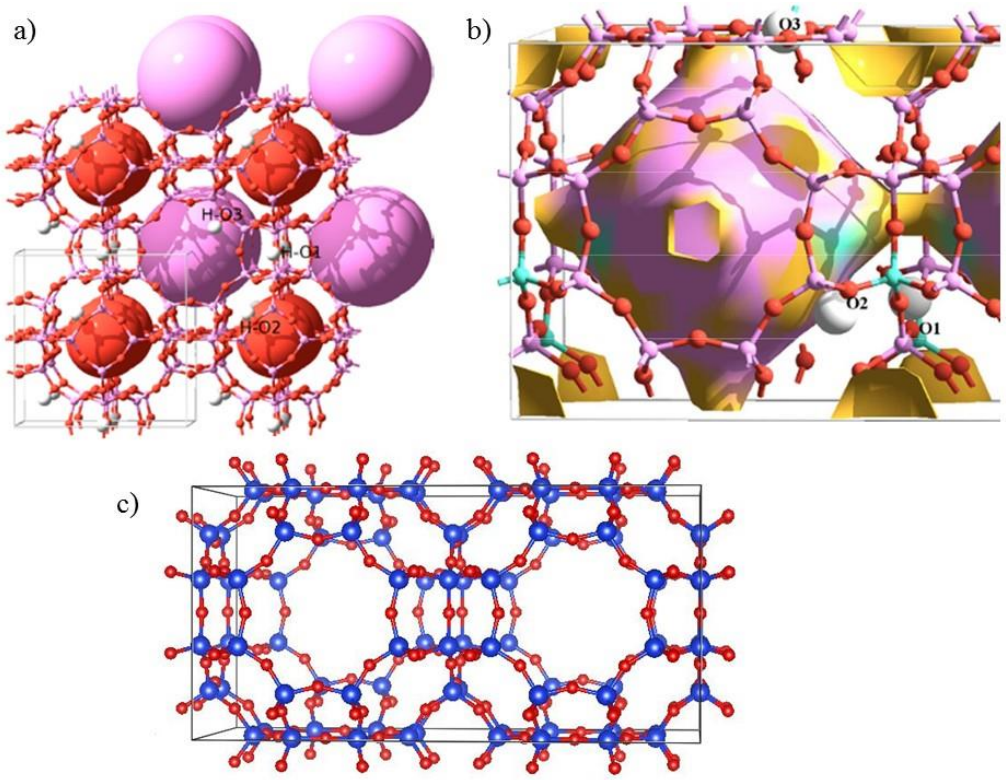

taken from [112]

Figure 25 a) and b) LTA zeolite with the micropore having large and small cavities. LTA contains 3 possible acid sites, distinguished by the type of oxygen (O1, O2, O3) to which the proton (highlighted as white ball) is attached, forming the SiOHAl Brønsted acid sites. O1H and O3H point toward the large cavity while O2H vibrates close to the small cavity, c) supercell 2×1×1 of LTA

3.2 Comparison between experimental INS and theoretical DFT results

Figure 26 shows the comparison of the experimental INS spectrum of LTA_40 with the calculated neutron spectra (LTA_47_O1H, LTA_47_O2H, and LTA_47_O3H) including the fundamental vibrations.

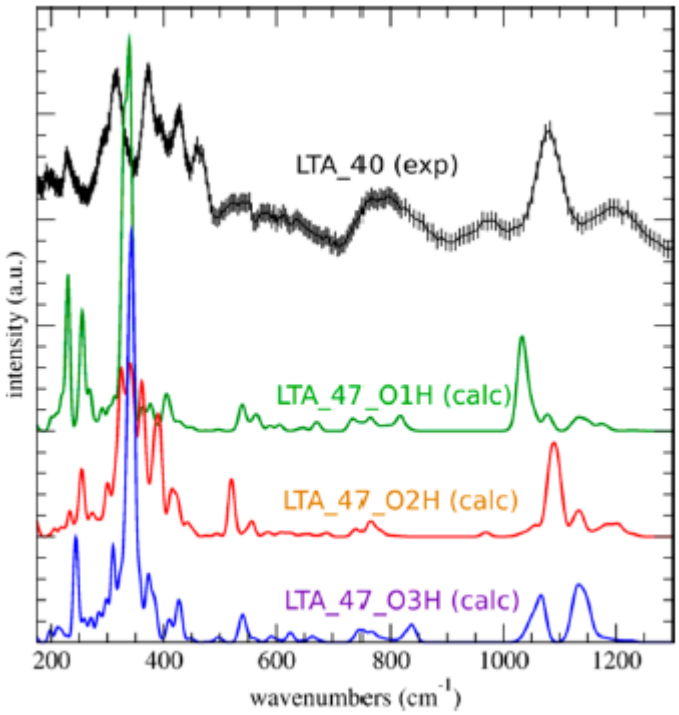

taken from [112]

Figure 26. Comparison between experimental INS spectra of LTA_40 and theoretical neutron spectra presented by fundamental vibrations calculated by periodic DFT for O1H, O2H, and O3H models of LTA_47

It can be seen that the calculated LTA_47_O2H model reproduces the experimental results more accurately than other models. An agreement between calculated and experimental spectra has been estimated by subtraction and relative comparison.

By analyzing the in-plane region of the presented spectra which is found at the frequencies from 1000 to 1200 cm^{-1} there can be emphasized the following: in case of the model LTA_47_O1H the peaks corresponding to SiOH in-plane bending reproduce the shape of the corresponding zone of the experimental spectrum, however, they are shifted to the lower frequencies. The spectrum calculated for LTA_47_O3H model contains two peaks of approximately equal intensities in the in-plane region which is not in agreement with the experimental spectrum. In case of LTA_47_O2H the in-plane region reproduces accurately the experimental result.

In the out-of-plane region of the experimental spectrum found at the frequencies from 273 to 450 cm^{-1} there can be seen a group of bands of a high intensities which is theoretically reproduced only by the spectrum obtained for LTA_47_O2H model, while the spectra calculated for LTA_47_O1H and LTA_47_O3H contain one intense peak and several peaks of a much lower intensity.

Furthermore, it can be seen that three computational models give clearly different INS spectra, and therefore it is reasonable to suggest that the sample of LTA-40 does not contain an appreciable number of protons located at O1H or O3H. As far as the spectrum calculated for the LTA_47_O2H model is confirmed to be the one that reproduces better the experimental spectrum, a detailed assignment of the bands present in the experimental spectrum can done by vibrational frequency analysis of calculated spectrum of LTA_47_O2H model.

3.3 Frequency analysis of the vibrational bands

The frequency analysis of the vibrational bands calculated for the O2H model allows us to identify the corresponding vibrational modes. The mode assignments and calculated frequencies are presented in **Table 3**.

Table 3. Vibrational modes of LTA_47_O2H as calculated from periodic DFT (DMol3/PBE)

Calculated frequency (cm^{-1})	Vibrational modes	Peak in the experimental INS spectrum (cm^{-1})
255	Zeolite framework	228
300	Zeolite framework + SiOH out-of-plane bending	296
325	SiOH out-of-plane bending	315
341	SiOH out-of-plane bending	
360	Zeolite framework + SiOH out-of-plane bending	373
390	Zeolite framework + SiOH out-of-plane bending	393
415	Zeolite framework + SiOH out-of-plane bending	429
441	SiOH out-of-plane bending	459
520	Al-O stretching (H riding mode)	552
557	Zeolite framework	
675	Zeolite framework	775
687	Zeolite framework	
735	Zeolite framework	
969	SiOH in-plane bending + Si-O stretching	963
1058	SiOH in-plane bending + Si-O stretching	1083
1084	SiOH in-plane bending	
1132	SiOH in-plane bending + Si-O stretching	---
1183	SiOH in-plane bending + Si-O stretching	1188
1199	SiOH in-plane bending + Si-O stretching	

We can note that two intense peaks appear at 325 and 341 cm^{-1}, attributed to the SiOH out-of-plane bending mode. An intense peak at 1084 cm^{-1} and a less intense at 1132 cm^{-1} are due to SiOH in-plane bending modes, in agreement with previous findings.

Hence, from previous INS studies, it is known that for RHO zeolite [58] the vibrations found at 1150 and 1060 cm^{-1} are attributed to the in-plane and out-plane SiOH bending modes respectively, but such study gave no assignment to a peak at 360 cm^{-1}. We obtain from the calculations a peak at 360 cm^{-1} (373 cm^{-1} in the experimental spectrum) which we assign to framework vibrations plus out-of-plane Si(or Al)OH bending. Quantum-chemical calculations by Sauer et al. [59] gave an out-of-plane Si(or Al)OH bending at 420 cm^{-1}, which appears at 415 cm^{-1} in our calculations, and at 429 cm^{-1} in the experimental spectrum. Therefore, it was obtained a good agreement between our study and the study of Sauer.

A peak found at 550 cm^{-1} in experimental and at 520 cm^{-1} in the calculated INS spectrum corresponds to the so-called ‘riding mode’ of a hydrogen atom attached to the oxygen atom which in its turn is bonded to a corresponding aluminium atom, such type of peak is caused by a Al-O stretching vibration, that is why this band is observed by INS which is sensitive to vibrations involving hydrogen atoms. Other peaks of low intensity found in the region from 550 to 800 cm^{-1} correspond to the vibrations of zeolitic framework. The peaks of lower intensity found at 255 and 300 cm^{-1} in the calculated and 228 and 296 cm^{-1} in the experimental INS spectra correspondingly are attributed to either framework vibrations or SiOH out-of-plane combined with framework vibrations.

In the study of faujasite zeolite by Jacobs et al. [60] the in-plane SiOH bending was detected at 1052 cm^{-1}, with a shoulder at 1169 cm^{-1}, and in our calculated LTA_47_O2H spectrum we obtain the intense in-plane SiOH bending at 1084 cm^{-1}, with a shoulder at 1132 cm^{-1}. The general features are similar to those observed in this study and the observed differences are due to the structural zeolite differences, supporting our view

that such differences may allow the assignation of proton locations. The experimental spectrum cannot be accurately described by fundamental vibrations as it contains additional bands which correspond to overtones and combinations of several orders, as it was aleready explained in 2.1.5.5. A multiphonon analysis of the calculated spectra should be done in order to obtain the shape of the spectra which would describe more accurately the experimental spectrum.

3.4 Multiphonon analysis

A broad band appears experimentally centered at 775 cm^{-1}, which initially could not be reproduced in the calculated neutron spectrum (see **Figure 26**). This is due to the fact that the calculated neutron spectra in **Figure 26** included only the fundamental bands. By including the first overtone, and not only the fundamental vibrations, it is possible to reproduce the broad band that appears at 775 cm^{-1} in the experimental spectrum, and at around 700 cm^{-1} in the calculated spectrum (see **Figure 27**).

This band corresponds to the first overtone of the out-of-plane SiOH bending, whose fundamental frequencies are at 325 and 341 cm^{-1}. This kind of band usually appears at a double frequency of the fundamental mode to which it corresponds and its intensity is lower than the intensity of the corresponding peak of fundamental vibrations. The origin of the discrepancy between the experimental (775 cm^{-1}) and calculated (700 cm^{-1}) frequency of this band (~ 75 cm^{-1}) is probably due to the error of the calculated fundamental frequencies in the low energy range (between 300 and 500 cm^{-1}). In the case of this band, the discrepancy is less important than the fact that we can justify its origin, as a first overtone of bands related to the SiOH out-of-plane bending.

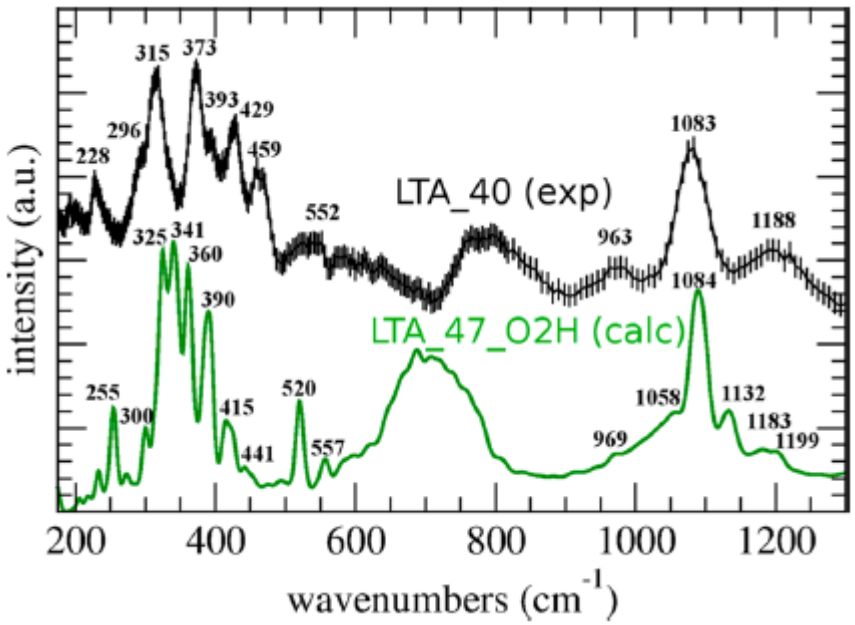

taken from [112]

Figure 27. Comparison between experimental INS spectra obtained for LTA_40 and DMol3/PBE calculated neutron spectra obtained for the O2H model of LTA_47 including the fundamental frequencies and the first overtone

The comparison between the experimental spectra of LTA-40 and computational neutron spectra obtained for LTA_47_O2H model including overtones is presented in **Figure 27** and shows an accurate description of the experimental results.

From the results presented above, it can be seen that the agreement between the model LTA_47_O2H and the experiment is better than that in **Figure 26**. Moreover, it can also be seen that the inclusion of the overtones in the other models (LTA_47_O1H and LTA_47_O3H), as shown in **Figure 28**, does not change this conclusion that the LTA_47_O2H is the model that gives the spectrum more similar to the experimental as

the broad band attributed to the first overtone of SiOH out-of-plane bending mode is reproduced accurately only by the spectrum calculated for the model LTA_47_O2H.

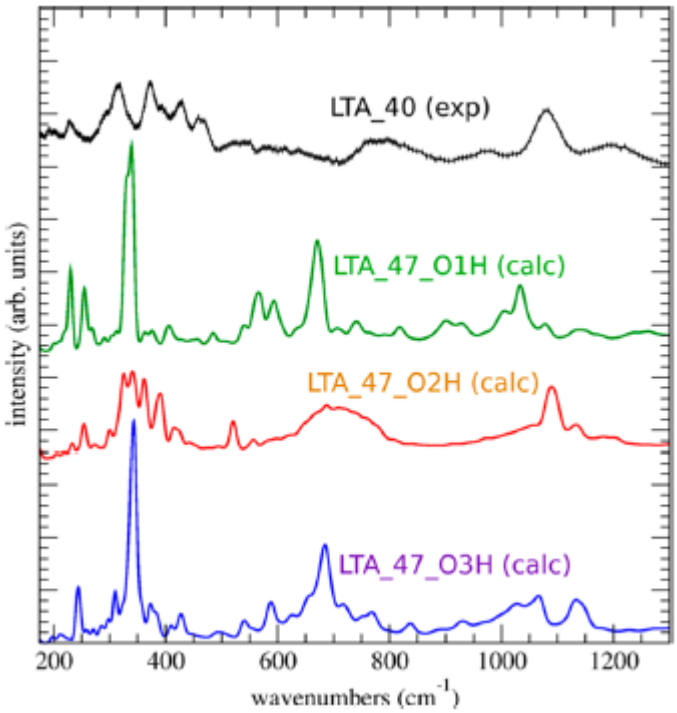

taken from [112]

Figure 28. Comparison between experimental INS spectra of LTA_40 and DMol3/PBE calculated neutron spectra (fundamental vibration and first overtone) for O1H, O2H and O3H models of LTA_47

Furthermore, the possible presence of a low number of other protons different from those of O2H type has been considered. In this particular case, it is somehow an advantage that the spectra of the LTA_47_OxH (x = 1−3) models are quite different to each other. If some acid sites of the O1H and/or O3H types would be present, we would expect

(according to **Figure 28**), among others, a peak at 1030 cm−1 (corresponding to O1H) and/or a doublet at 1060 and 1140 (corresponding to O3H). These peaks seem to be absent in the INS spectrum, but we cannot preclude that a small amount, below ∼10%, of O1H and/or O3H centers are present, in a way that these peak features do not appear clearly in the INS spectrum.

3.5 Periodic DFT energies

Moreover, the periodic DFT calculations also allow to obtain the relative energies of the three unit cells LTA_47_OxH (x=1-3) which can be calculated for each model by subtracting the lowest value among total energies (which is found to be the one of LTA_47_O2, equal to -55321453.6 kJ/mol) from the values of total energy of each of the models ($E_{relative}$(LTA_47_OxH) = E_{total}(LTA_47_OxH) - (-55321453.6)). The relative energies can be used in order to estimate the relative stabilities of 3 models (see third column of **Table 4**). According to this data the model LTA_47_O2H can be considered the most stable.

Table 4. Periodic DFT (DMol3/PBE) calculated energies for models LTA_47_OxH

Model	E_{total} (kJ/mol)	$E_{relative}$ (kJ/mol)	ZPVE (kJ/mol)	$ZPVE_{relative}$ (kJ/mol)	$E_{relative-corr}$ (kJ/mol)
LTA_47_O1H	-55321440.1	13.5	1430.7	2.4	15.9
LTA_47_O2H	-55321453.6	0	1428.3	0	0
LTA_47_O3H	-55321426.2	27.3	1429.7	1.4	28.7

However, zero-point vibrational energy (ZPVE) is not included in the calculated total energy and, hence, in the relative energies of models LTA_47_OxH. ZPVE represents

the energy of the system at T = 0 K and it should be considered in order to convert the total electronic energies obtained from *ab initio* quantum mechanical studies into 0 K enthalpies. The corresponding values of ZPVE for the models LTA_47_OxH are presented in the fourth column of **Table 4**. We calculated the relative ZPVE in the similar way we calculated the relative total energies (see fifth column of **Table 4**). Then, we added the corresponding relative ZPVE to the values of relative total energies Thus, we get the corrected values of relative energies of the models LTA_47_OxH (see sixth column of **Table 4**). These do not change qualitatively the results, and O2H continues to be the most stable location. Hence, LTA_47_O2H is the one with lowest energy and this could be rationalized taking into account that O2H is the proton vibrating inside the smallest ring (6T-ring), while the others (O1H and O3H) vibrate inside 8T-rings. Vibration in a smaller ring leads to smaller O---H distances and hence stronger H-bond stabilizing interactions, which justifies the lower energy of LTA_47_O2H.

It is likely that the major presence of O2H protons in the LTA_40 sample is related to this being the most stable position. In many occasions the proton location depends on how the organic template employed in the synthesis located in the zeolite cavity, but given the symmetry of the LTA cavity (α-cage) it is likely that any oxygen location (O1, O2, O3) can be accessible to the proton of the charged template, and we can assume that, a priori, any of the three proton sites (O1H, O2H, O3H) could be a possible outcome of the zeolite calcination process, where the charged template is removed from the micropore, leaving the proton as a zeolite Brønsted site. Under this condition, that all proton sites seem equally probable, it may hold the energetic argument, so that the energetically preferred proton location (O2H) is the most populated in the LTA_40 sample.

3.6 ^{29}Si NMR and Infrared characterization of high silica LTA (LTA-40)

The spectrum of the sample of LTA-40 measured by solid state ^{29}Si MAS NMR is shown in **Figure 29**.

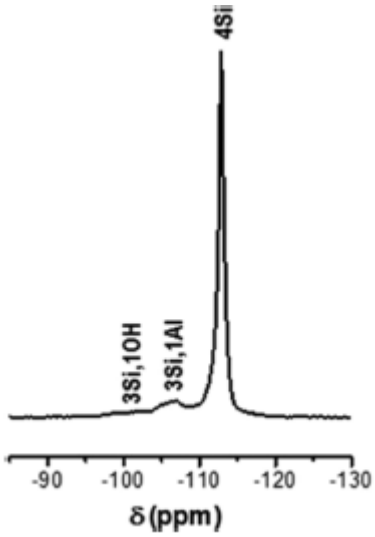

Figure 29. ^{29}Si MAS NMR spectrum of LTA-40 calcined (measured by Vidal-Moya, J.A.; Blasco, T.; Rey, F.; Valencia, S. Instituto de Tecnología Química (UPV-CSIC))

The quantitative analysis of ^{29}Si MAS NMR spectrum of the LTA-40 sample gives a Si/Al ratio of 32, very close to that obtained by chemical analysis (Si/Al = 40). The presence of silanol groups (extra framework OH groups) is hardly seen in the ^{29}Si MAS NMR spectrum, indicating that it is a nearly defect-free Al-containing sample.

The IR spectrum of zeolite LTA-40 at the stretching hydroxyl region, where the silanol and the Brønsted groups vibrate, is shown in **Figure 30**.

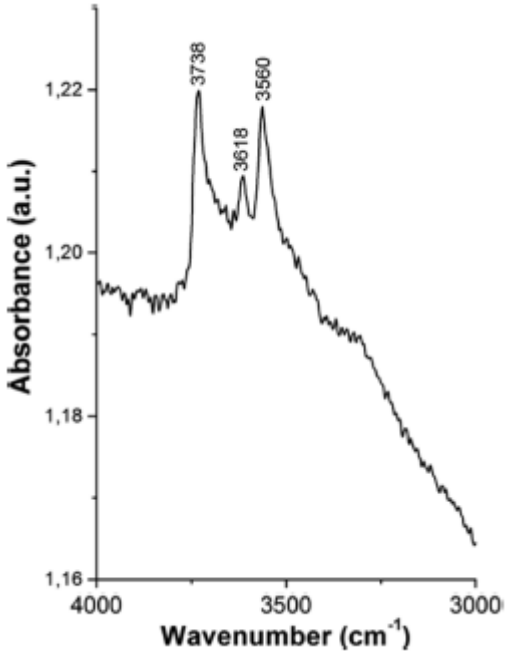

Figure 30. Stretching hydroxyl region of the IR spectrum of the outgassed LTA-40 sample at 673 K for 12 hours under high vacuum (better than 10^{-6} mbar) (measured by Rey, F.; Valencia, S.; Instituto de Tecnología Química (UPV-CSIC))

From **Figure 30**, it can be seen the presence of three main bands, one at a higher wavenumber (3738 cm^{-1}) assigned to silanol groups, while the weak band at 3618 and more intensive one at 3560 cm^{-1} are attributed to Brønsted acid sites pointing toward large α-cages and small sodalite cages respectively.

It is generally believed that, on a given zeolite, acid sites in small cavities show smaller frequencies than those in large cavities. Although this is not always followed [31] in the case of LTA, this is very likely to happen due to the presence of two well-defined cavities (α and sodalite) of different sizes. The computational results presented in the following subsection confirm this hypothesis. We suppose that the formation of silanol groups

appears during the grinding of the sample for preparing the self-supported wafer used for IR measurements, and this is the reason why a strong band appears at 3738 cm^{-1}. However, the band of silanol groups (marked as 3Si, 1OH in **Figure 29**) is practically negligible in the ^{29}Si NMR spectrum, in which the sample did not need grinding. Hence, this confirms that the silanols appear due to the grinding of the sample. The INS experiment was performed with a sample without grinding and hence without an appreciable amount of silanol groups.

3.7 Comparison of the calculated OH-stretching frequencies with experimental Infrared results

Periodic DFT calculations performed for the models LTA_47_OxH (x=1-3) also give the OH-stretching vibrations. The three calculations give the following results presented in **Figure 31**.

In case of LTA_47_O1H the corresponding OH-stretching peak was found at 3600 cm^{-1}, while in case of LTA_47_O2H and LTA_47_O3H this peak appears 3533 and 3587 cm^{-1} respectively. As it was already explained in 2.1.5.5, the influence of high values of Q and the Debye-Waller factor results in decrease of resolution of the peaks at high-frequency region of the INS spectrum, thus the peaks corresponding to OH-stretching vibrations cannot be observed by INS. However, the calculated results from the **Figure 31** can be compared with infrared findings. The experimental IR spectrum (see **Figure 30**) gives two bands: a band of high intensity found at 3560 cm^{-1} and a band of low intensity found at 3618 cm^{-1}. We suppose that the intense band appearing at 3560 cm^{-1} is attributed to the O2H proton (LTA_47_O2H) stretching vibration, whose calculated value is 3533 cm^{-1}, displaced only by 27 cm^{-1} from the experimental value. It is also interesting to note that this band has high intensity, as it corresponds to our conclusion that most of the acid centers correspond to the O2H sites.

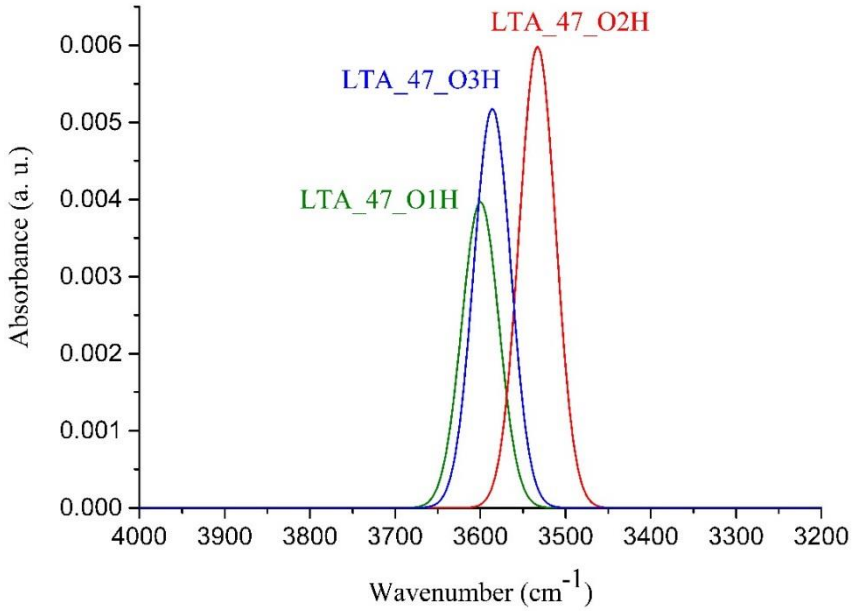

Figure 31. DMol3/PBE calculated stretching frequencies of fundamental vibrations for models LTA_47_OxH

Moreover, the weak band that appears at 3618 cm^{-1} in the experimental IR spectrum (see **Figure 30**) could be attributed to O1H protons, whose calculated stretching frequency is found 3600 cm^{-1}, displaced only by 18 cm^{-1} from the experimental value, and in agreement with a similar underestimation of the other O-H stretching frequency at O2H. According to this, the IR experiment would indicate a small number of O1H centers in addition to the large majority of centers at the O2H position. O3H centers, vibrating at 3587 cm^{-1} could also be responsible of the IR band observed at 3618 cm^{-1}. It is not possible to quantify the relative abundance from the infrared spectrum since it is not a quantitative technique for this task. From the comparison between the INS results and the calculated neutron spectra (Figure), the calculated peaks of O1H and O3H at

1033 cm^{-1}, and the doublet at 1060 and 1140 cm^{-1} respectively, do not appear in the experimental INS spectrum, suggesting that the O1H or O3H centers, if present, are a small number.

3.8 Additional study of possible crystallographic positions of the acid sites LTA-40

In addition we subsequently performed a periodic DFT (CASTEP/PBEsol) study in order to confirm the conclusion based on DMol3 study.

Comparison of experimental INS spectrum of LTA-40 with calculated spectra obtained for LTA_47_OxH models of LTA-40 by CASTEP is presented in **Figure 31**. We calculated HDOS of fundamental vibrations using DFT data form CASTEP and we applied the resolution of 3% for theoretical spectra to be equal to the resolution of the instrument.

Apart from the computational methodology applied, the difference between calculated fundamental vibrations of the models LTA_47_OxH presented in **Figure 26** and **Figure 32** correspondingly is the following: in the DMol3 study (**Figure 26**) the fundamental vibrations were extracted from the DMol3 output by using aClimax software and in case of CASTEP study the corresponding fundamental vibrations have been extracted from the output by calculating hydrogen partial density of states, $gH(\omega)$, with a corresponding script implemented in LAMP [115] software.

As it is can be seen from **Figure 32**, in case of CASTEP the analysis of calculated fundamental vibrations is not efficient for defining which of the models better reproduces experimental results. The multiphonon study is required.

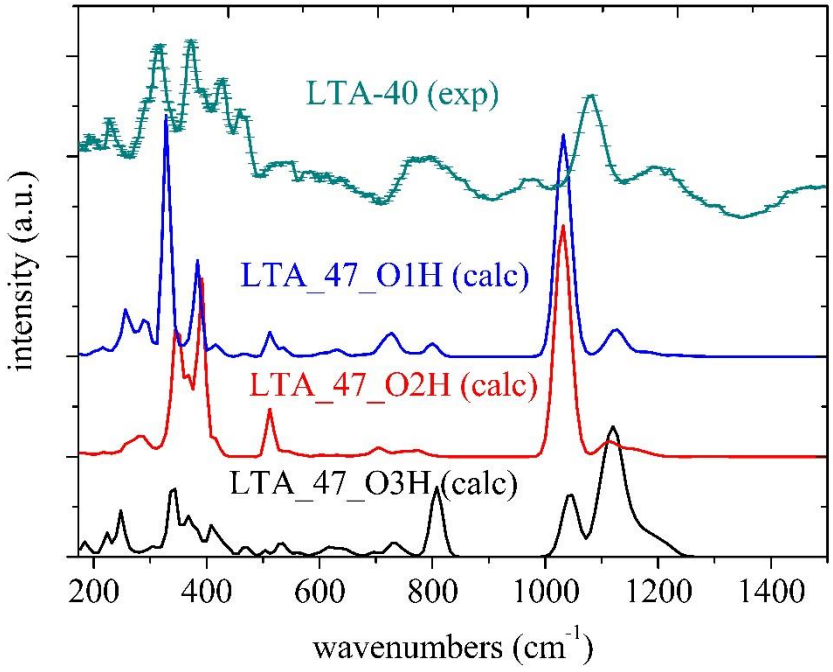

Figure 32. Comparison of experimental INS spectrum of LTA-40 with HDOS fundamental vibrations calculated for different models of LTA-40 by CASTEP/PBEsol with a resolution of 3%

Figure 33 shows the comparison between the experimental INS spectrum of LTA-40 and calculated spectra of LTA_47_OxH models including fundamental vibrations, first overtone and second order combinations. As well as the fundamentals, the spectra including multiphonons appear different from those presented in **Figure 28** of DMol3 study, this is due to not only the differences between computational methodology (DMol3 and CASTE), but also because of the differences between the algorithm of extraction of the multiphonons used in aClimax and Mantid software correspondingly.

If we compare **Figures 28** and **33**, we can conclude that in case of LTA-40 the multiphonons obtained by DMol3/aClimax methodology better reproduce the

experimental INS spectrum than those obtained by CASTEP/Mantid, however, by analyzing the spectra presented in **Figure 33**, we can also conclude that the spectrum calculated for LTA_47_O2H model reproduces experimental spectrum better than spectra calculated for LTA_47_O1H and LTA_47_O3H models which confirms the conclusion based on DMol3 study.

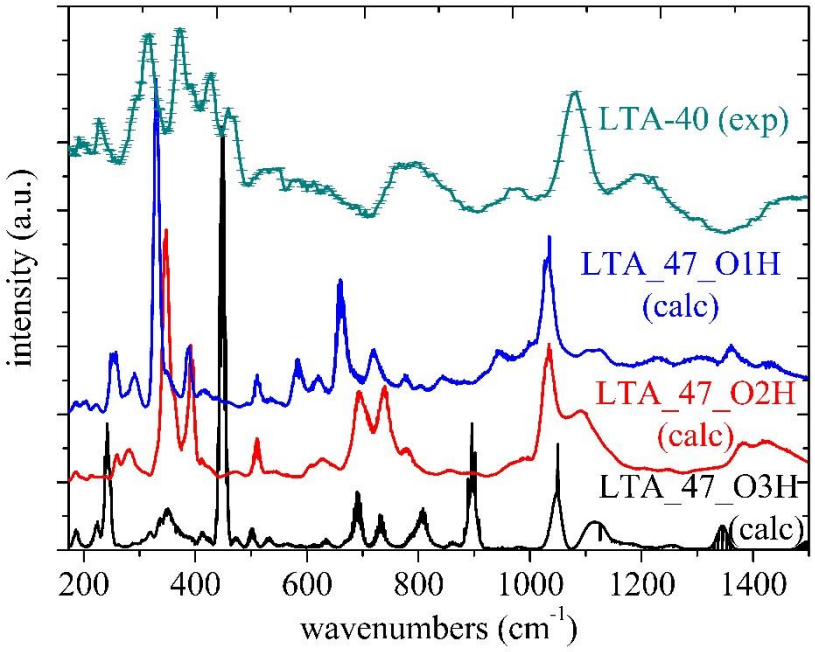

Figure 33. Comparison between experimental INS spectrum obtained for LTA-40 and periodic DFT-calculated neutron spectra obtained by CASTEP/PBEsol for the LTA_47_OxH models of LTA-40 using the Mantid software with a resolution of 3%, including fundamental frequencies, first overtone with second order combinations, and the total calculated spectrum.

3.9 Conclusions of the Inelastic Neutron Scattering Study on the Location of Brønsted Acid Sites in High Silica LTA Zeolite

For this study we have chosen a structurally simple material, for which a synthesis in fluoride media (yielding an essentially defect-free zeolite) was possible, and this procedure is general and can be applied to other zeolites. We have shown that the combination of a high quality of zeolite sample, and high sensitivity of the instrument, as well as periodic DFT calculations allows for the first time to detect with high precision the acid sites of LTA with Si/Al = 40 and obtain information about their position. It has been found that the most probable location of the Brønsted acid sites in the LTA- 40 sample considered in this study is O2H. Since the OH bending bands cannot be observed by IR spectroscopy and are more sensitive to the local environment than OH stretching vibrations, the use of INS has allowed us to locate the acid sites of LTA zeolite. The accurate determination of the location of the acid sites will depend on how different are the peaks of each acid site, but the high sensitivity of the INS instrument employed seems sufficient for almost any zeolite.

Chapter 4

Inelastic Neutron Scattering Study of the Aluminum and Brønsted Site Location in Aluminosilicate LTA Zeolites

This chapter is dedicated to the combine INS, NMR and computational study of Brønsted acidity in LTA-5 zeolite.

By having successfully applied the combination of high sensitivity of the neutron spectrometer, as well as periodic DFT calculations, we have detected with high precision the location of the acid sites in LTA-40 which contains only ½ of a hydrogen atoms in the unit cell. In contrast to the unit cell of LTA-40 which contains hydrogen atoms far from each other, the unit cell of LTA-5 contains 4 hydrogen atoms, which are located closer to each other. In this case the main factor that will define the acidy is a distribution of aluminium atoms in the framework of zeolite, which in its turn subsequently defines the possible locations of the acid sites. However, finding the distribution of aluminum atoms in a zeolitic framework still remains a challenging task since silicon and aluminium atoms are not accurately distinguishable by usual X-ray techniques due to small difference between their atomic numbers. Neither powder neutron diffraction analysis can be applied [53] since it is not able to give the precise location of the acid sites.

Nowadays, the most popular technique which is used to define the distribution of aluminium atoms in zeolites is ^{29}Si NMR spectroscopy. One of the most important studies was performed by Lippmaa and Engelhardt [35]. This work presents the results of high-resolution ^{29}Si NMR studies of synthetic zeolites A, X, Y and of a series of natural zeolite minerals with different structures and Si/Al ratios. It has been shown that generally the ^{29}Si NMR spectra of simple zeolites may show a maximum of 5 peaks with a good resolution that correspond to the five different types of silicon atoms presented in the framework of a zeolite depending on their local environment. The first type indicated as Q_0 corresponds to the silicon atom that contains 4 aluminum, i.e. Si (0 Si), atoms in its neighboring coordination sphere, Q_1 indicates the silicon atom with 1 silicon and 3 aluminum atoms, Si (1 Si), and then up to Q_4 corresponding to the silicon atom with 0 aluminum atoms, i.e. Si (4 Si), in its neighboring sphere. This type of analysis is able to describe the local environment of each silicon atom in further combination with the numerical methods or computational modeling, it can provide rough representation of the distribution of aluminium atoms in the framework of zeolites. Nevertheless, this

method does not allow to fully define the distribution of aluminum atoms in zeolitic frameworks. For the purpose of this work we define that the aluminium distribution is only certainly determined when a model of the structure containing the location of all the atoms in the unit cell can be proposed that is compatible with the observations of NMR and other techniques. In the present work we applied a different approach that allowed us to propose a fully determined aluminium distribution of LTA-5, and once the distribution of aluminium atoms is known, there are four possible locations for each Brønsted site.

Different unit cell models were created, which are compatible with the distribution of Si atoms (Q_n, n = 0-4) in LTA zeolite with Si/Al ratio 5 obtained by means of ^{29}Si NMR. This was done using our own software specifically designed [116]. Then, the combination of INS and DFT calculations allowed us to certainly determine the most probable distribution of aluminum atoms in the zeolite framework. By knowing this and applying the restriction rules regarding the geometry discussed in this chapter, it is possible to find the most probable locations of the acid sites in LTA-5 zeolite.

4.1 ^{29}Si MAS NMR Characterization of LTA-5

Experimental results obtained from the ^{29}Si MAS NMR of LTA-5 are shown in **Figure 34**. As it can be seen, the spectrum contains four peaks that correspond to different types of silicon atoms (Q_1, Q_2, Q_3, and Q_4), depending on the number of Si (and, hence, Al) atoms in their first neighboring coordination sphere. This classification of peaks obtained by ^{29}Si MAS NMR have been introduced in work of Lippmma et al. [35] and was explained in **Chapter 1** of this thesis.

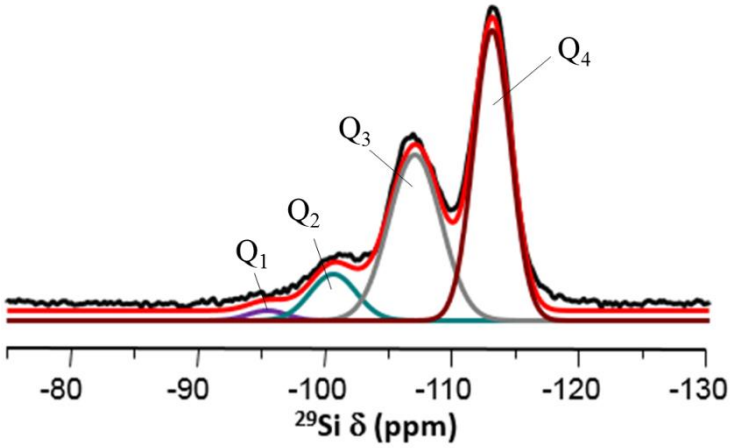

taken from [114]

Figure 34. ^{29}Si MAS NMR spectra of LTA-5 zeolite

As it can be seen from **Figure 34**, the peaks corresponding to different types of silicon atoms have different intensities. It was shown that the area under the resonance signal is proportional to the number of atoms giving this signal. For instance, the peak of the lowest intensity corresponds to silicon atoms of type Q_1 and, hence, its content in the sample of LTA-5 is the lowest. Furthermore, according to the intensities and thus the areas of the peaks the content of silicon atoms of different types increases in the following raw: Q_1, Q_2, Q_3, and Q_4.

Electronic integrator which is implemented in the NMR spectrometer automatically depicts the cascade curve. Thus, the relation between heights of the steps in the curve shows the relation between the number of different types of silicon atoms presented in the sample.

The results of a quantitative analysis of the spectrum presented by **Figure 34** is shown in **Table 5**.

First, the relative populations of the Si(nSi) environments expressed in % were determined as the relation between the area of the corresponding peak to a sum of areas of all the peaks of the spectrum according to the following formula:

$$Q_n = \frac{I_{Si(nSi)}}{\sum_0^4 I_{Si(nSi)}} * 100$$ **Equation 32**

In the equation (32) $I_{Si(nSi)}$ is attributed to the area of the peak corresponding to a silicon of type n and $\sum_0^4 I_{Si(nSi)}$ corresponds to the sum of the areas of all the peaks that appear in the NMR spectrum (see **Figure 34**).

The resulting content (%) of each type of silicon atom is presented in the second column of **Table 5**.

Table 5. Content of different types of Si atoms in LTA-5 zeolite (taken from [114])

	Q_n (%)	**Number of Si atoms per $Si_{40}Al_8O_{96}H_8$ unit cell ($N(Si)_n$)**
Q_0	0	0
Q_1	1.8	0.7
Q_2	10.9	4.4
Q_3	41.5	16.6
Q_4	45.8	18.3

taken from [114]

Second, since further in the computational study we are going to consider a double unit cell of LTA-5, we calculated the number of Si atoms (see third column of **Table 5**) of each type in the double unit cell of LTA-5 using the formula:

$$N(Si)_n = \frac{Q_n}{100} * N(Si)_{total} \qquad \textbf{Equation 33}$$

where $N(Si)_{total}$ is the total number of silicon atoms in the double unit cell of LTA-5 (which is eaqual to 40) and Q_n corresponds to the type of silicon atom Si(nSi) with n=0-4.

4.2 Computational models of Al/H distributions in LTA-5

Similarly to the study of LTA-40 we used a double unit cell of LTA to build computational models which is presented by **Figure 35**.

The framework of LTA contains rings which in their turn may contain 4, 6, and 8 T-atoms (where T is either Si or Al). It has a large cavity of a diameter of 11.4 Å, which is surrounded by eight sodalite cages connected by their square faces in a cubic structure.

As it was already mentioned, the unit cell of LTA contains 24 T-atoms and, as it was mentioned above, has the following formula $Si_{(24-x)}Al_xO_{48}H_x$. Therefore, in order to have a Si/Al ratio close to the experimental value (Si/Al = 5), we performed our calculations on a 2 × 1 × 1 supercell, containing eight aluminum and Brønsted sites (x = 8), resulting in the cell having a formula $Si_{40}Al_8O_{96}H_8$.

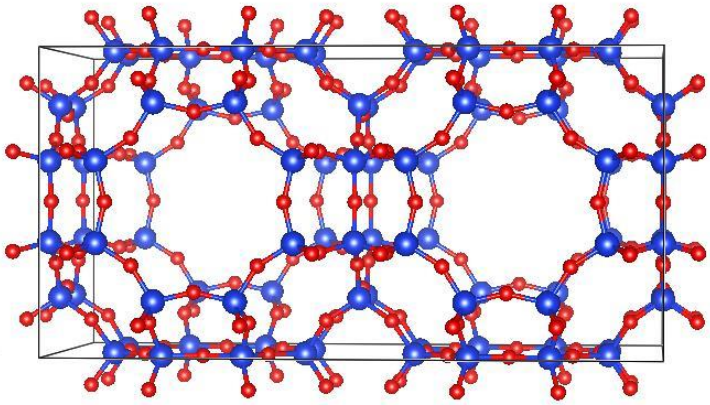

taken from [114]

Figure 35. Framework of LTA zeolite showing a 2 × 1 × 1 unit cell containing 48 T-atoms

To obtain different unit cell models of $Si_{40}Al_8O_{96}H_8$ compatible with the distribution of silicon atoms as shown in **Table 5**, a modified version of zeoTsites was employed [116, 117]. The software can generate a large number of unit cells containing the desired number of aluminium atoms (obeying the Lowenstein rule) as well as the corresponding Brønsted sites, and it calculates the resulting population of the different types of $Si(Q_n)$. One thousand unit cells were generated, with those containing neighboring Brønsted sites (−OH−Si−OH−) being removed as they led to artificially strong electrostatic repulsion. Nine unit cells with Q_n distributions very similar to the experimental data (see **Table 6**) were selected for the subsequent periodic DFT calculations. Each of these models (hereafter called **d1−d9**) consists of a unit cell of LTA-5 with a particular distribution of aluminium and hydrogen atoms.

Table 6. Number of different types of Si atoms (Q_n) obtained in selected computationally-generated Al and H distributions (d1-d9) of $Si_{40}Al_8O_{96}H_8$ unit cells

model	Q_0	Q_1	Q_2	Q_3	Q_4
exp	**0**	**0.7**	**4.4**	**16.6**	**18.3**
d1	0	0	7	18	15
d2	1	3	1	17	18
d3	0	0	7	18	15
d4	0	1	6	17	16
d5	0	0	6	20	14
d6	1	2	3	16	18
d7	0	1	6	17	16
d8	0	0	4	24	12
d9	0	2	5	16	17

Taken from [114]

From **Table 6** it follows that the investigated sample of LTA-5 does not contain silicon atoms that are bonded to four aluminium atoms, it also contain 0.7 silicon atoms which are bonded to three aluminium and 1 other silicon atoms, 4.4 silicon atoms with two other silicon and two aluminium atoms in their first neighboring coordination sphere, 16.6 silicon atoms with three other silicon and one aluminium and 18.3 silicon atoms with 4 bonded to four other silicon atoms.

The structures of models **d1-d9** are presented in **Figures 36-44**, respectively. In these models silicon, aluminium, oxygen and hydrogen atoms are represented by blue, violet, red and white balls correspondingly.

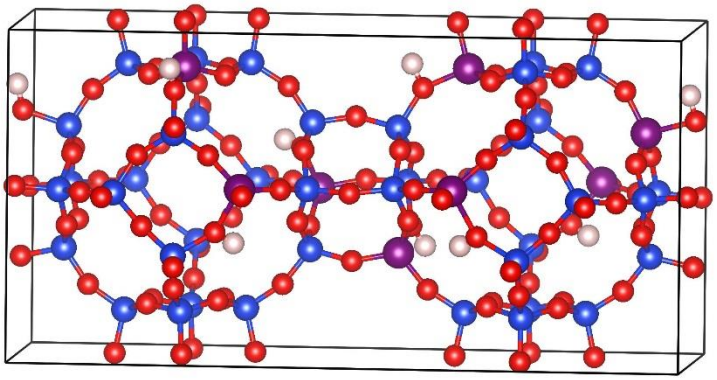

Figure 36. Structure of model d1

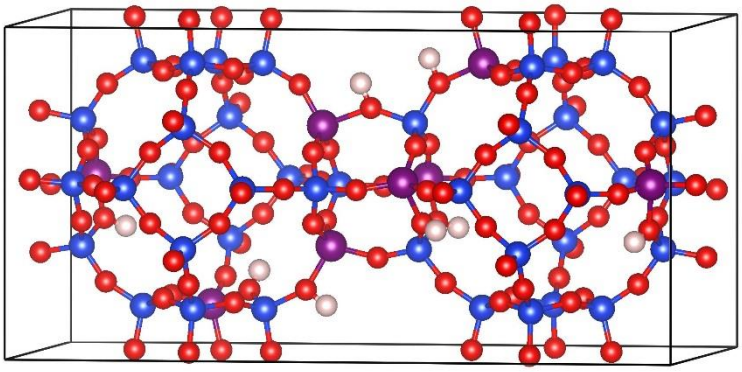

Figure 37. Structure of model d2

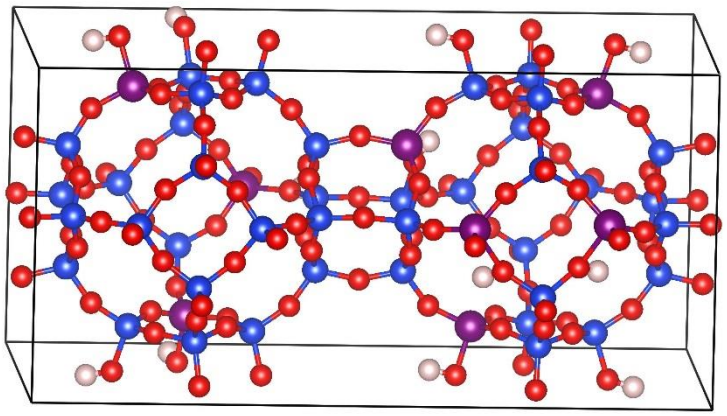

Figure 38. Structure of model d3

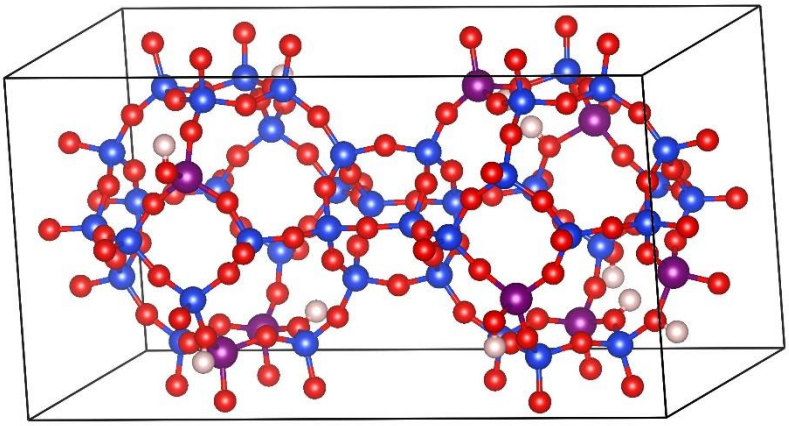

Figure 39. Structure of model d4

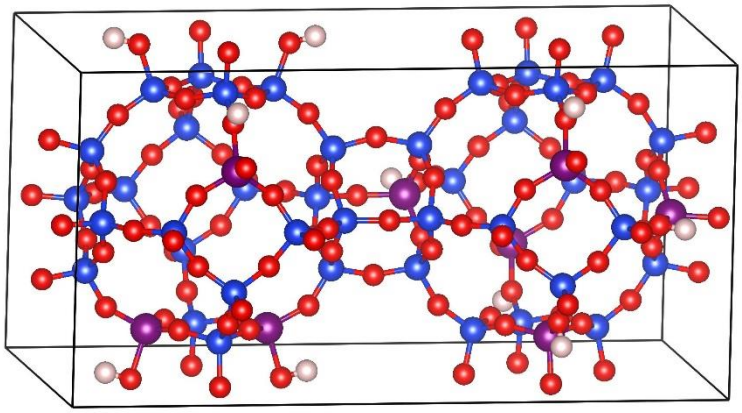

Figure 40. Structure of model d5

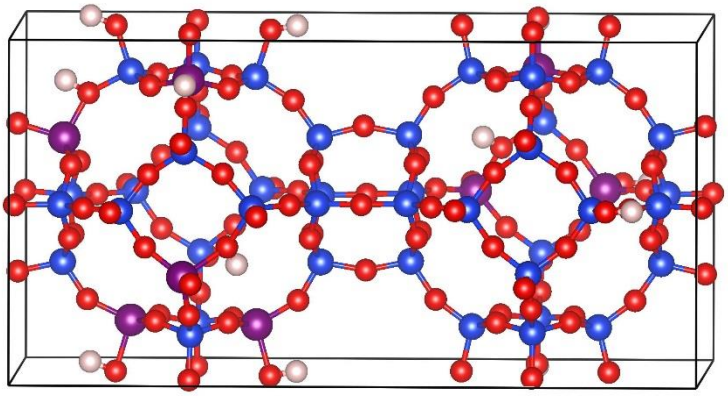

Figure 41. Structure of model d6

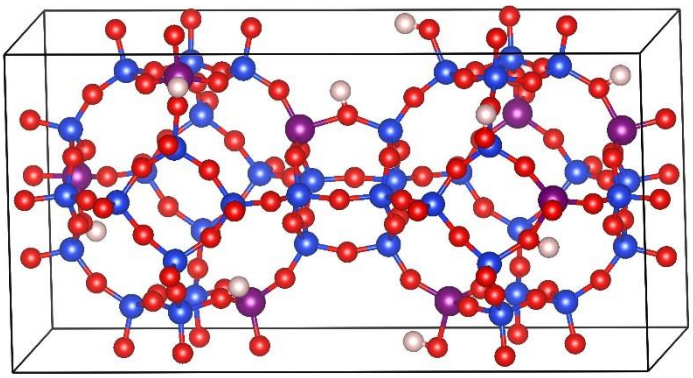

Figure 42. Structure of model d7

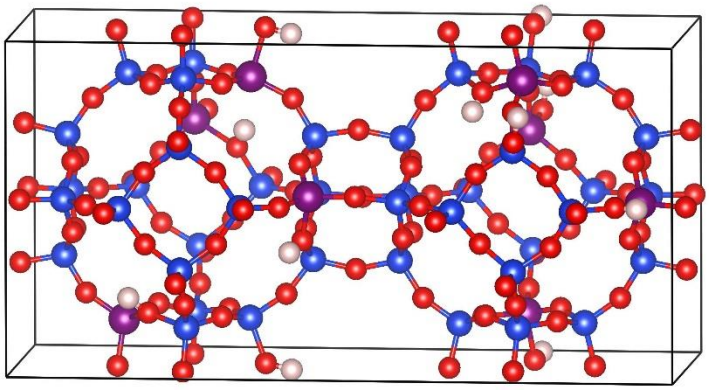

Figure 43. Structure of model d8

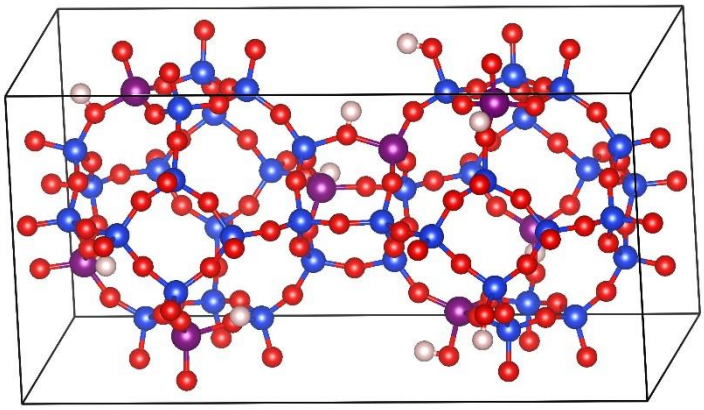

Figure 44. Structure of model d9

Each of the models contains 8 hydrogen atoms which are distributed along the cell in different ways such as these hydrogen atoms can point either toward 6T or 8T-rings (see **Table 7**).

Table 7. Number of hydrogen atoms pointing towards 6T and 8T-rings in models d1-d9

Model	Number of H atoms pointing towards 6T-ring	Number of H atoms pointing towards 8T-ring
d1	7	1
d2	5	3
d3	5	3
d4	8	0
d5	5	3
d6	6	2
d7	6	2
d8	6	2
d9	4	4

Even though models **d2**, **d3** and **d5** contain the same number of hydrogen atoms pointing to 6T and 8T rings (5 and 3 correspondingly), as well as models **d6**, **d7** and **d8** (6 and 2 correspondingly), the distribution of aluminium atoms and thus hydrogen atoms in these models is different.

In consequence, we performed a periodic DFT calculations for models **d1**-**d9** and compared computational results with experimental INS data.

4.3 Comparison between experimental INS and theoretical DFT results

The comparison between the experimental INS spectrum, GDOS(ω), of LTA-5 and the hydrogen partial density of states, $g_H(\omega)$, obtained from DFT calculations performed for models d1-d9 is presented in **Figure 45a**.

Similarly to LTA-40, the spectrum of LTA-5 contains two main groups of vibrational bands: the first one in the region between 210 and 660 cm^{-1} that corresponds to out-of-plane vibrational modes, and the second between 950 and 1260 cm^{-1}, attributed to the in-plane bending vibrations. A detailed assignation of peaks will be performed below, after a suitable unit cell of LTA-5 is proposed.

It can be seen that different computational models (d1−d9) give different INS spectra, showing that the calculated spectrum is very sensitive to the aluminium and proton distributions. The subsequent task is to determine which of the calculated spectra better reproduces the experimental spectrum.

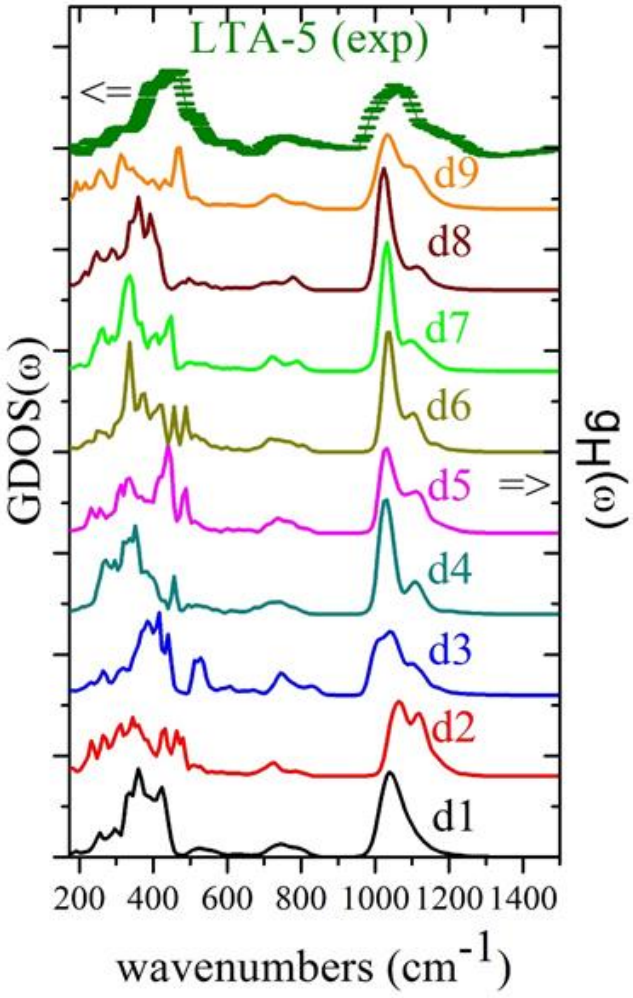

taken from [114]

Figure 45a. Comparison between the experimental INS spectrum of LTA-5 and the hydrogen partial density of states, $g_H(\omega)$, of the fundamental vibrations calculated by periodic DFT for the models d1−d9 with a resolution of 3%

First, by performing a simple visual analysis, we can exclude models that contain obvious dissimilarities with the experimental spectrum. Therefore, we try to identify as "unlikely" those vibrational features that appear in the calculated spectra and do not appear in the experimental spectrum. This task can be carried out by using only the calculated normal vibrational modes and analyzing the type of vibrations regarding the location where the protons are vibrating. Such an analysis of the normal vibrational modes of the **d1− d9** models allows the identification of general trends as to which types of protons produce peaks of high intensity in the calculated INS spectra.

Figure 45b shows a replot of **Figure 45a** comparing experimental INS spectrum of LTA-5 and the hydrogen partial density of states of the fundamental vibrations calculated by periodic DFT for **d1**-**d9** models with resolution 3 %.

It was found that the peaks found in the out-of-plane bending region (210-500 cm^{-1}) correspond to either protons pointing towards 6T-rings (those marked with triangles) or protons vibrating in 8T-rings (which are marked with a squares). Some modes correspond to those which include some protons vibrating in 6T-rings and some in 8T-rings at the same time. These peaks are marked with both symbols.

In order to simplify the analysis we also indicated the main bands found in the experimental INS spectrum (see **Figure 45b**). Regarding the out-of-plane region of the experimental INS spectra there can be found two peaks of mayor intensities found at 396 and 446 cm^{-1} and a group of peaks of lower intensity found in the region from 234 to 396 cm^{-1}.

The spectrum calculated for **d1** model does not contain evident dissimilarities with the experimental spectrum, hence, it should be considered in more details below.

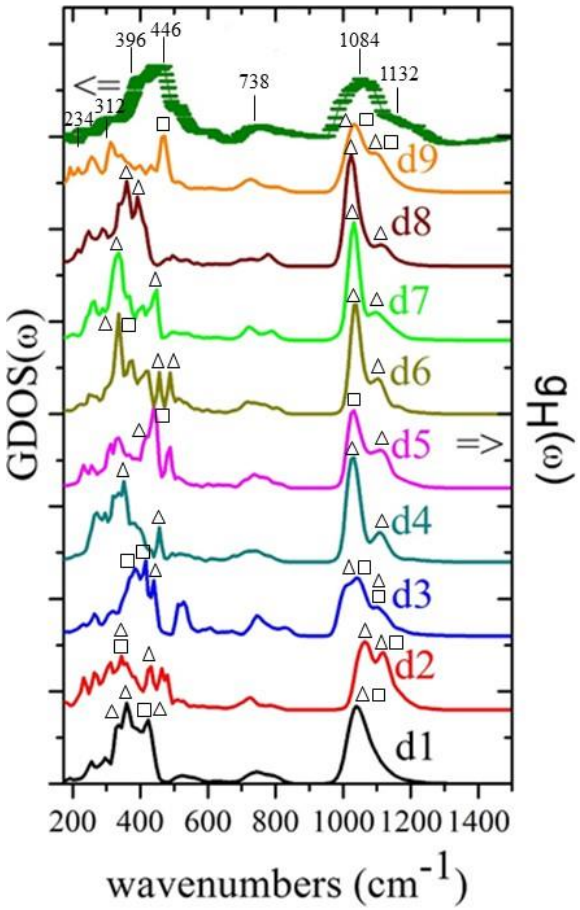

taken from [114]

Figure 45b. Replot of Figure 45a comparing experimental INS spectrum of LTA-5 and the hydrogen partial density of states of the fundamental vibrations calculated by CASTEP/PBEsol for d1-d9 models with resolution 3 %, including the comparison main peaks in experimental and computational spectra (taken from [114]). Modes that correspond to protons vibrating in 6T-rings are marked with triangles, protons vibrating in in 8T-rings are marked with squares, modes that corresponds to some protons vibrating in 6T and other in 8T-rings are marked by both triangles and squares

At the same time, in the computed for **d2** model spectrum there are several peaks of low intensity corresponding to SiOH out-of-plane vibrations. The most intense peaks of this region are found at 431 cm^{-1} attributed to the vibrations of hydrogen atoms pointing towards 6T and 8T rings and at 462 cm^{-1} of a hydrogen atoms pointing towards 6T rings correspondingly. Low intensities of these peaks can be explained by analyzing the structure of model d2 (see **Figure 37**): it contains 4 aluminium atoms in the double-four-ring (D4R), hence, aluminium atoms and so protons are located too close to each other reducing the amplitude and therefore the intensity of the corresponding SiOH vibrations. This is in disagreement with the experimental result and, thus, model **d2** can be excluded.

The spectrum calculated for **d3** model does not contain evident dissimilarities with the experimental spectrum, hence, it should be considered in more details below.

Furthermore, the spectrum calculated for **d4** model contains in its out-of-plane region a group of intense peaks with the peak of highest intensity found at 352 cm^{-1} corresponding to the SiOH out-of-plane bending of the hydrogens pointing towards 6T-ring, another peak of lower intensity also corresponds to the SiOH out-of-plane bending of the hydrogens pointing towards 6T-ring. This is in disagreement with experimental spectrum which allows us to exclude model **d4**.

Similarly to the case of **d1** and **d3**, the spectrum calculated for **d5** model does not contain evident dissimilarities with the experimental spectrum, and therefore, it should be also considered in more details below.

The spectrum calculated for model **d6** contains a group of peaks at the region around 450 cm^{-1} (one at 454 and another at 489 cm^{-1}) corresponding to the SiOH out-of-plane bendings of the hydrogen atoms pointing towards 6T-rings, however, the intensity of these peaks is lower than the intensity of the corresponding peaks in the experimental spectrum and in addition to that the spectrum corresponding to **d6** model contains the

peak of highest intensity at 336 cm^{-1} which is attributed to the SiOH out-of-plane bendings of the hydrogen atoms pointing towards 6T and 8T-rings which is in disagreement with the experimental result. Moreover, it can be seen that the general shape of the spectrum does not correspond to the experimental.

Similarly to that, the spectrum computed for the model **d7** contains a less intense peak at 433 cm^{-1} and the most intensive peak at 333 cm^{-1}, both corresponding to the SiOH out-of-plane bending modes of the hydrogen atoms pointing towards 6T-rings. This is in disagreement with the experimental result and, therefore, models **d6** and **d7** can be also excluded.

In case of **d8** model, there were found two intense peaks at 361 and 393 cm^{-1}, both attributed to the SiOH out-of-plane bendings of the hydrogen atoms pointing towards 6T rings, and no peaks appear at the region of 446 cm^{-1} (the most intensive peak in the experimental spectrum). Hence, we can be also exclude model **d8**.

At the same time the spectrum calculated for **d9** model contains only one intense peak at 471 cm^{-1} corresponding to the SiOH out-of-plane bending modes of the hydrogen atoms pointing towards 8T rings which is also in disagreement with experimental spectrum.

Thus, we have eliminated models **d2**, **d4**, **d6**, **d7**, **d8** and **d9**, and, hence, we can conclude that the models that better reproduce the experimental results are **d1**, **d3**, and **d5**. This is also in agreement with the result obtained by numerical procedure of finding similarity between two spectra based on a recent work by Hoffman et al. [118] (see subsection 4.7 below). From this, it is possible to quantitatively determine the correspondence of our simulated spectra with the experimental result, using the similarity index. Once the best aluminum and proton distributions have been identified (**d1**, **d3**, and **d5**), we try to find

whether they have in common with the experimental spectrum certain vibrational features that can be assessed as "likely".

In general, the analysis indicates that high intensities in the out-of-plane bending region (210−500 cm^{-1}) are due to isolated protons vibrating in rings (either 6-rings or 8-rings) without other protons present in the ring. This happens not only in the best models (**d1**, **d3**, and **d5**) but also in d6, d7, and d8. On the contrary, distributions, such as **d2**, **d4**, and **d9**, with the spectra that do not have intense peaks in the region where most intense peaks of the experimental spectrum of LTA-5 are located (**d2**, **d4**, and **d9**) contain a larger number of rings with more than one proton, and we identify this as "unlikely" to be present in the sample of LTA-5.

Regarding the in-plane bending mode region, **d1** shows a broad band in the region of 1050 cm^{-1}, due to two vibrational bands very close in energy, 1048 and 1070 cm^{-1}, that correspond to hydrogen atoms in 6T-ring and 8T-ring respectively. In the **d5** model, these bands are well separated in energy (1082 and 1132 cm^{-1} for hydrogens in 8T-ring and 6T-ring respectively) leading to a better agreement with the experimental spectrum. The in-plane bending mode region of the spectrum calculated for **d3** model is similar to those of **d5** model, nevertheless, in this case the peaks are not so well separated as in case of **d5**.

Finally, by taking into account only fundamental vibrations of the spectra calculated for d1, d3 and d5 models, we cannot come to a definite conclusion which of the models better reproduces the experimental results and multiphonon analysis is required.

4.4 Multiphonon analysis

The calculated INS spectrum of model **d5** including fundamental frequencies and first overtone with second-order combinations is presented in **Figure 46** and shows an even

better agreement with the experimental spectrum than the previous calculation that included only fundamental vibrations.

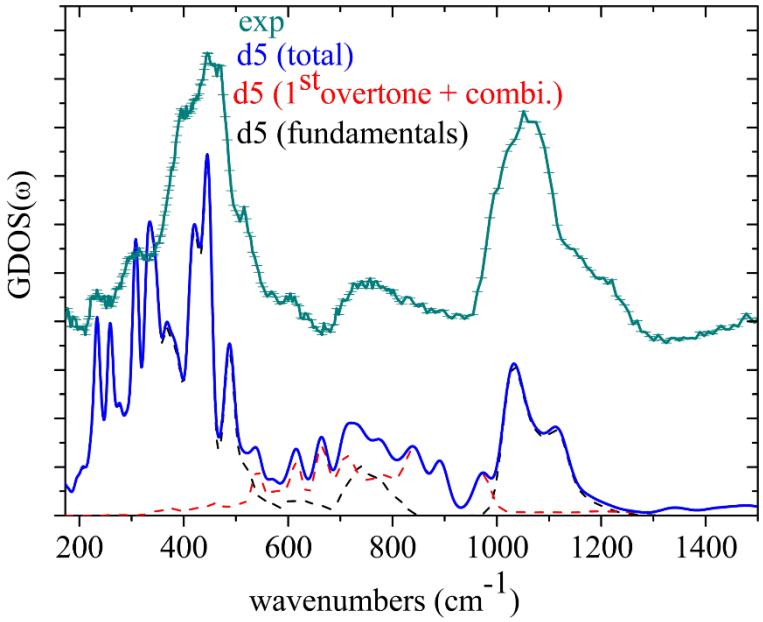

taken [114]

Figure 46. Comparison between experimental INS spectrum obtained for LTA-5 and CASTEP/PBEsol calculated neutron spectra obtained for the d5 model of LTA-5 using the Mantid software with a resolution of 3%, including fundamental frequencies, first overtone with second order combinations, and the total calculated spectrum

A similar multiphonon calculation for **d3** and **d1** are presented by **Figure 47**. Unlike the case of the **d5** model where the multiphonon analysis confirmed the agreement with the experimental INS spectrum, in the case of **d1** and **d3** we observe that the broad band at 700-850 cm^{-1}, corresponding to the first overtone of the out-of-plane vibrations gives a too large intensity.

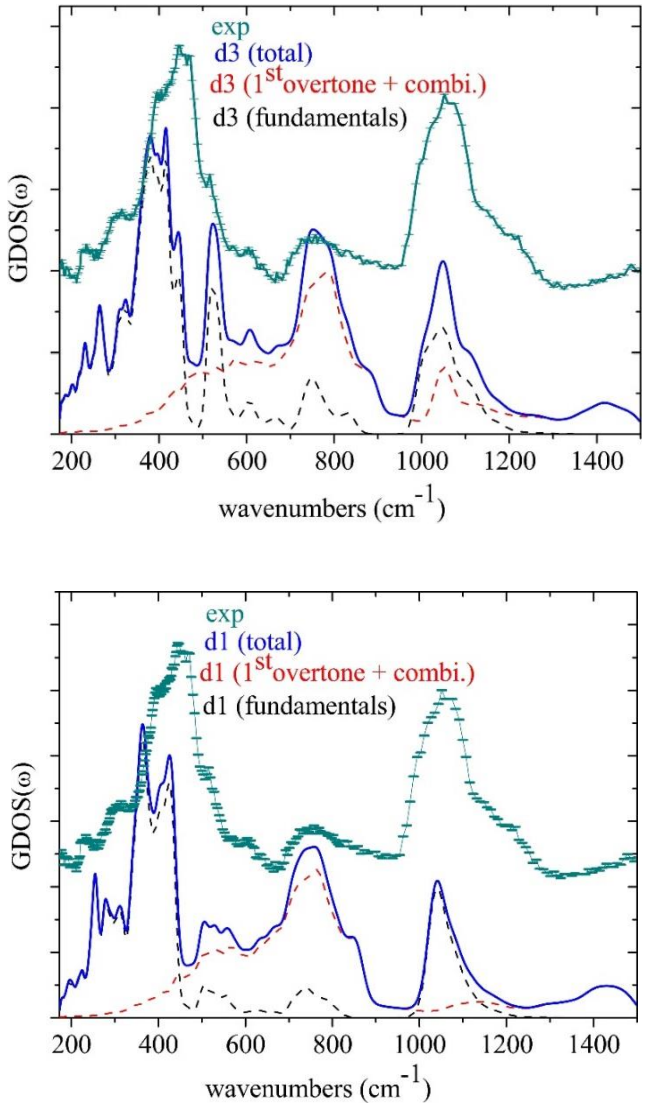

taken from [114]

Figure 47. Comparison between experimental INS spectrum and CASTEP/PBEsol calculated neutron spectra of d3 (top) and d1 (bottom) models of LTA-5 with Mantid software with resolution 3%, including fundamental frequencies, first overtone with second order combinations, and total calculated spectrum

On the other hand, the relatively small intensity of the band at 950-1260 cm^{-1}, attributed to the in-plane bending modes, does not increase (as would be expected in order to match the experimental INS spectrum) when taking into account the multiphonon approach.

Furthermore, the theoretical assignment of the bands of the INS spectrum of LTA-5 can be done by the vibrational analysis of the modes of the model **d5** of LTA-5 as it has been concluded that the computational spectrum of this model reproduces better the experimental results.

4.5 Frequency analysis of the vibrational bands in stable Al distribution of LTA-5

A selection of the normal mode vibrational analysis (calculated by CASTEP/PBEsol) for the **d5** model is shown in **Table 8**, containing the frequencies and the components of the vibrations.

The two intense peaks found at 396 and 446 cm^{-1} correspond to the SiOH out-of-plane bending vibration attributed to the hydrogen atoms pointing towards either 6T or 8T-rings (see **Figure 45**). Another two peaks, at 1084 and 1132 cm^{-1} are attributed to the in-plane bending mode. The broad peak at 738 cm^{-1} corresponds to the riding mode of the hydrogen atom which also overlaps with a broad band found at 700-850 cm^{-1}, assigned to the first overtone of the out-of-plane fundamental vibrations. Moreover, less intense peaks found at 234 and 312 cm^{-1} correspond to the SiOH out-of-plane bending combined with vibrations of zeolitic framework.

In addition to that, in order to check the feasibility or unfeasibility of the resulting models and support the results presented above the analysis of the aluminum distributions models d1-d9 has been performed.

Table 8. Vibrational modes of d5 calculated by CASTEP/PBEsol

Vibrational modes	Peak in the experimental INS spectrum (cm^{-1})	Calculated Frequency (cm^{-1})
Zeolite framework + SiOH out-of-plane bending	234	233
Zeolite framework + SiOH out-of-plane bending		255
Zeolite framework + SiOH out-of-plane bending	312	313
Zeolite framework + SiOH out-of-plane bending		328
SiOH out-of-plane bending		335
SiOH out-of-plane bending	396	417
SiOH out-of-plane bending	446	443
SiOH out-of-plane bending		484
O-H riding	738	738
SiOH in-plane bending	1084	1029
SiOH in-plane bending	1132	1116

taken from [114]

4.6 Analysis of the Al and H distributions in models d1-d9 of LTA-5

It is known that the presence of aluminum atoms located close to each other in zeolitic framework reduces the stability of the structure due to the electrostatic interactions. The

relative feasibility of models **d1-d9** (see **Figures 36-44**) has been roughly estimated considering several criteria presented below.

4.6.1 Aluminium in double-four rings

First, the number of aluminum atoms in double-four-rings (D4R) of each model has been calculated (see **Table 9**).

Table 9. Number of double-four-rings (D4R) containing 0-4 Al in models d1-d9 of LTA-5. The 2×1×1 unit cell of LTA contains 6 D4R. Analysis made with zeoTsites software

Number of D4R containing 0-4 Al atoms					
model	**0 Al**	**1 Al**	**2 Al**	**3 Al**	**4 Al**
d1	0	4	2	0	0
d2	2	2	1	0	1
d3	1	3	1	1	0
d4	1	3	1	1	0
d5	0	4	2	0	0
d6	1	3	1	1	0
d7	1	2	3	0	0
d8	0	4	2	0	0
d9	1	2	3	0	0

taken from [114]

The presence of more than two aluminum atoms in D4R reduces the stability of the model due to the electrostatic interactions caused by the aluminium atoms located close to each other. Models **d3**, **d4** and **d6** have D4R with 3 aluminium atoms, and model **d2** contains a D4R with 4 aluminium. This suggests that the models **d1**, **d5**, **d7**, **d8** and **d9** can be considered as more feasible than **d2**, **d3**, **d4** and **d6**, as these models only contain double-four rings with maximum 2 aluminium atoms.

4.6.2 Proton content of 8T-rings

The number of 8T-rings containing two protons has also been calculated (see **Table 10**), showing that distributions **d1**, **d5**, **d6**, **d7** and **d8** can be considered as more feasible by having 0 8T-rings with two protons and, hence, not containing Brønsted sites that are located too close to each other, while each of the models **d2**, **d3** and **d4** contain one 8T-ring with two protons and model **d9** contains two 8T-rings with two protons. Another

important feature is the distribution of Brønsted sites in either 6T-rings or 8T-rings. **Table 10** allows to obtain this information by indicating the number of protons in 8T-rings. And, accordingly, taking into account that the total number of protons is 8, the number of protons in 6T-rings can be obtained straightforwardly. Considering that 8T-rings that contain only one proton tend to give intense peaks in the INS spectrum, the number of such 8T-rings would reach a value of: 3 (in models **d1**, **d3**, **d8**), 4 (in **d7**), 5 (in **d6**) and 6 (in **d5**). In total there are 6 8T-rings in the 2×1×1 unit cell of LTA.

Table 10. Location of Brønsted sites in 8-rings in d1-d9 models of LTA-5

model	d1	d2	d3	d4	d5	d6	d7	d8	d9
Number of 8T-rings containing 2 H	0	1	1	1	0	0	0	0	2
Number of H in 8T-rings	3	4	5	4	6	5	4	3	6

taken from [114]

4.6.3 Aluminum content of 6T-rings

Then, it has been analyzed the number of aluminium atoms in each of the 6T-rings of the double-unit cell of LTA-5 (see **Table 11**).

In total there are 16 6T-rings in the double-unit cell of LTA-5, which may contain 0, 1 or 2 aluminium atoms (6T-rings cannot contain more than two aluminium atoms due to the Lowenstein rule). Although it could be thought that the presence of two aluminium atoms in 6T-ring may reduce the stability of the models, but probably this is not the case, since, the models with more 6T-rings containing two aluminium atoms, such as **d6**, **d1**, **d2**, and **d3**, of which **d1** and **d3** are considered to be good candidates given their calculated INS spectra being similar to the experimental.

Table 11. Number of 6-rings containing 0, 1 or 2 Al atoms in models d1-d9 of LTA-5. The 2×1×1 unit cell of LTA contains 16 6-rings

Number of 6-rings			
model	**0 Al**	**1 Al**	**2 Al**
d1	4	8	4
d2	4	8	4
d3	4	8	4
d4	3	10	3
d5	3	10	3
d6	5	6	5
d7	3	10	3
d8	3	10	3
d9	3	10	3

taken from [114]

4.6.4 Al-Al and H-H close distances

The last criterion employed is the average minimum distance between Al-Al and H-H atoms in models **d1-d9** (see **Table 12**). This can be obtained by calculating the closest Al-Al and H-H distance for each of the 8 aluminium atoms in the model, and taking the average value. A feasible (or more probable) Al distribution will contain the Al atoms as far as possible, in this case the electrostatic interactions are more balanced giving more stabilized configuration.

Table 12. Average minimum distance between Al-Al and H-H atoms in models d1-d9 of LTA-5

model	Average minimum distance between Al atoms (Å)	Average minimum distance between H atoms (Å)	Two smallest H-H distances (Å)
d1	5.2	5.9	5.4, 5.5
d2	4.9	5.1	4.3, 4.9
d3	5.2	5.1	4.4, 4.9
d4	5.1	5.0	4.4, 4.5
d5	5.5	5.8	5.4, 5.5
d6	4.8	5.4	4.6, 5.2
d7	4.9	6.1	4.8, 5.4
d8	5.6	5.3	4.7, 4.8
d9	4.7	4.9	3.3, 4.3

taken from [114]

The average minimum distance between aluminium atoms is larger in **d5** and **d8** models, giving 5.5 and 5.6 Å, respectively, while for the rest of the models this value varies from 4.7 to 5.2 Å. However none of the values seem small enough so as to be considered not feasible. Regarding the minimum H-H distance, **d1**, **d5** and **d7** would be the most feasible, but, with the exception of **d9** (containing a H-H distance of 3.3 Å), all the distributions seem feasible.

If we take into account two smallest distances, **d5** and **d1** would give the highest values and, hence, can be considered as most feasible models.

It can be concluded that overall, the criteria presented above help to extract a general conclusion that none of the distributions, except perhaps **d9**, with an H-H distance of 3.3 Å, and **d2** containing a D4R with 4 aluminium atoms, seems to present unreasonable features in their chemical structure that may lead to unfeasibility or instability. This is a direct consequence of having forced the Al distributions to match the Q_n distributions of

the experimental ^{29}Si NMR spectrum of the LTA-5 sample. From a very high occurrence of feasible distributions (all **d1**-**d9** except, perhaps, **d2** and/or **d9**), the analysis of the similitude to the experimental INS spectrum (which has been performed in the Subsection 4.3) can be considered the sufficient condition to clarify which of the models would be able to reproduce the features of the LTA-5 sample. Moreover, taking into account all the structural criteria discussed above, it can be concluded that **d5** is the most feasible model, since the analysis shows that this model does not contain regions where aluminium atoms are more concentrated, but rather aluminium atoms are uniformly distributed in the crystal, with most of the 6T-rings containing less than two aluminium atoms, 8T-rings containing no more than one proton, and no D4R containing more than two aluminium atoms. This finding confirm our previous conclusion.

4.7 Mathematical comparison of experimental and calculated INS spectra

In the Subsection 2.3.2 we did a simple visual analysis in order to exclude the theoretical models that contain obvious discrepancies with the experimental INS spectrum and choose the models that can be considered as those that can describe better the experimental data.

In case of LTA-40 we did such visual analysis for 3 models and it was easy to perform. While in the study of LTA-5 we had to deal with 9 models and, hence, it was more difficult to compare the calculated and experimental spectra by a simple visual analysis. Moreover, in case of applying such a strategy for the systems that require larger number of models it no longer can be considered as purely objective. Thus, in order to confirm the conclusions made in the Subsection 2.3.2 we also perform a mathematical comparison of the corresponding peaks in computational and the experimental spectra.

According to a recent work by Hoffman et al. [118], we have followed a computational procedure to evaluate the similarity between two spectra. This was done to quantitatively determine the correspondence of our simulated spectra with the experimental result, using the similarity index, which evaluates the correlation between two functions:

$$\text{similarity}_{(1,2)} = \frac{\sum_{\forall \nu_i} I_1(\nu_i) * I_2(\nu_i)}{\sqrt{\sum_{\forall \nu_i} I_1^2(\nu_i) * \sum_{\forall \nu_i} I_2^2(\nu_i)}} \qquad \textbf{Equation 34}$$

Here $I_1(\nu)$ and $I_2(\nu)$ represent the intensities of the simulated and experimental spectrum, respectively, at frequency ν, where the equation above implies a constant Δν for the intervals between any two successive frequencies ν_i and ν_{i+1}. A similarity value of zero means absolutely no correspondence between both spectra, while a value of one indicates that the spectra are identical. As the peaks in an INS spectrum are narrow, comparison of the simulated and experimental spectrum should be done using the same frequency scale and with narrow intervals between successive frequencies. In our case we have performed the comparison in the 200-1400 cm^{-1} range, using intervals of $\Delta\nu$ = 1 cm^{-1}. Before using the equation above it is necessary to determine the correct scaling factor for the intensities, which has been done by normalizing the area of the two spectra to be compared.

From the results obtained (see **Table 13**), it follows that **d5** model is the most similar to the experimental spectrum with the similarity factor equal to 0.885. Other models such as **d3**, **d9**, **d2** and **d1** are also similar to the experimental (similarity above 0.8), but among them we would neglect **d2** and **d9** based on the analysis of models performed in Section 4.6. It has to be said, however, that the mathematical function of similarity does not reflect important factors such as the reproduction of certain important experimental frequencies.

Table 13. Similarity between the experimental and calculated (models d1-d9) INS spectra of LTA-5. Left table: ordered by models. Right table: ordered by decreasing similarity

Al distrib.	similarity
d1	0.806
d2	0.816
d3	0.870
d4	0.693
d5	0.885
d6	0.783
d7	0.723
d8	0.704
d9	0.828

Al distrib.	similarity
d5	0.885
d3	0.870
d9	0.828
d2	0.816
d1	0.806
d6	0.783
d7	0.723
d8	0.704
d4	0.693

taken from [114]

For instance, the spectrum of **d1**, in spite of being 'worse' than **d9** and **d2** according to the respective similarities, it is probably a 'better' (than **d9** and **d2**) spectrum as it has a good agreement with the peaks in the 210-500 cm^{-1} region (see **Figure 45 a)**), the worse agreement of the model **d1** can be explained by discrepancies in the in-plane bending zone, as two in-plane bending modes in experimental spectrum overlap in the spectrum calculated for d1 model forming one peak. Hence, **d3** and **d1** should follow **d5** in our short list of final distributions that meet all the requirements explained in this study.

4.8 Is the calculated INS spectrum method-dependent? CASTEP vs. DMol3

Apart from CASTEP study we performed a DFT calculations for models d1-d9 by using DMol3 code applying HCTH and PBE functionals. We compared the experimental INS

spectrum of LTA-5 with the hydrogen partial density of states, gH(ω), of the fundamental vibrations calculated by periodic DFT with a resolution of 3%.

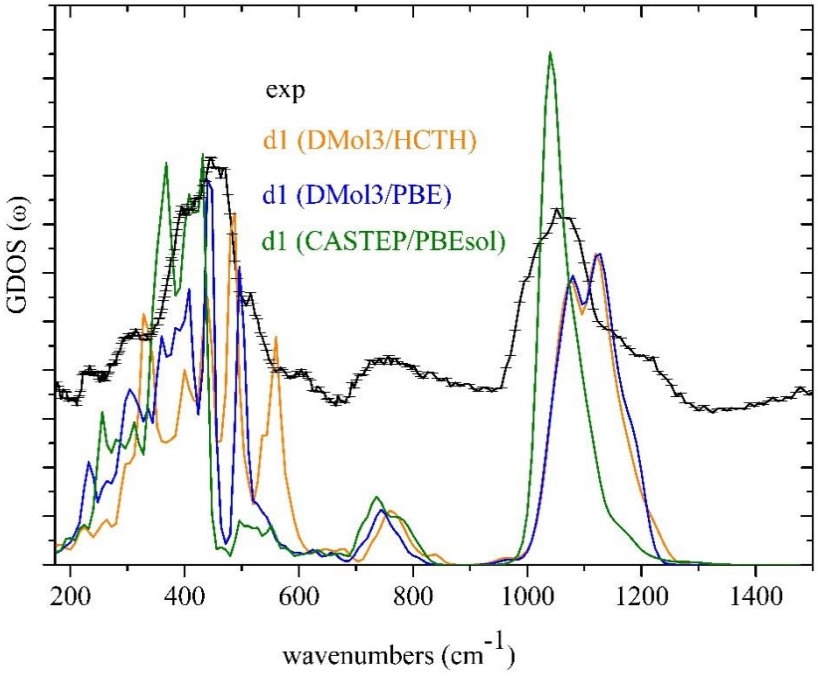

Figure 48. Comparison between the experimental INS spectrum of LTA-5 and fundamental vibrations calculated with DMol3 (HCTH, PBE and PBEsol functionals) for the model d1

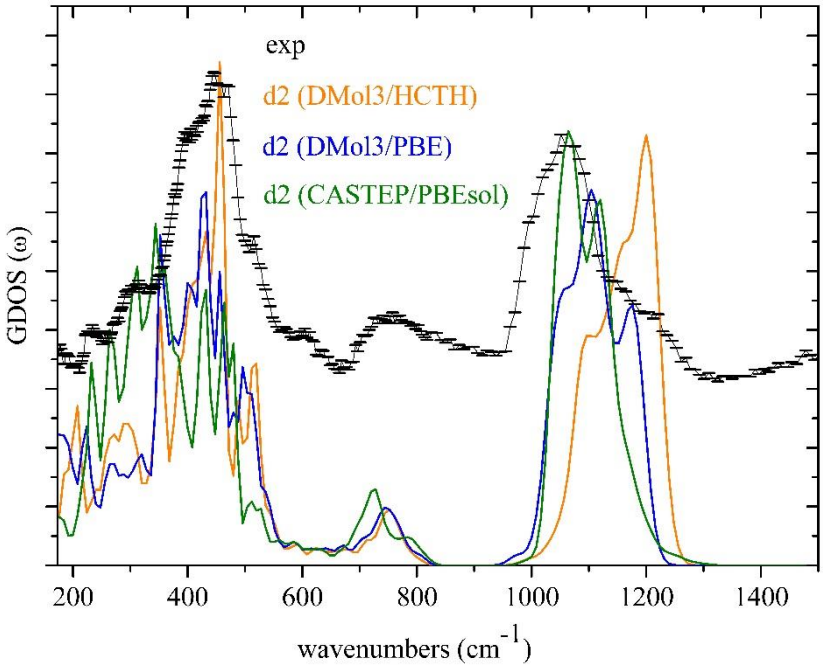

Figure 49. Comparison between the experimental INS spectrum of LTA-5 and fundamental vibrations calculated with DMol3 (HCTH, PBE and PBEsol functionals) for the model d2

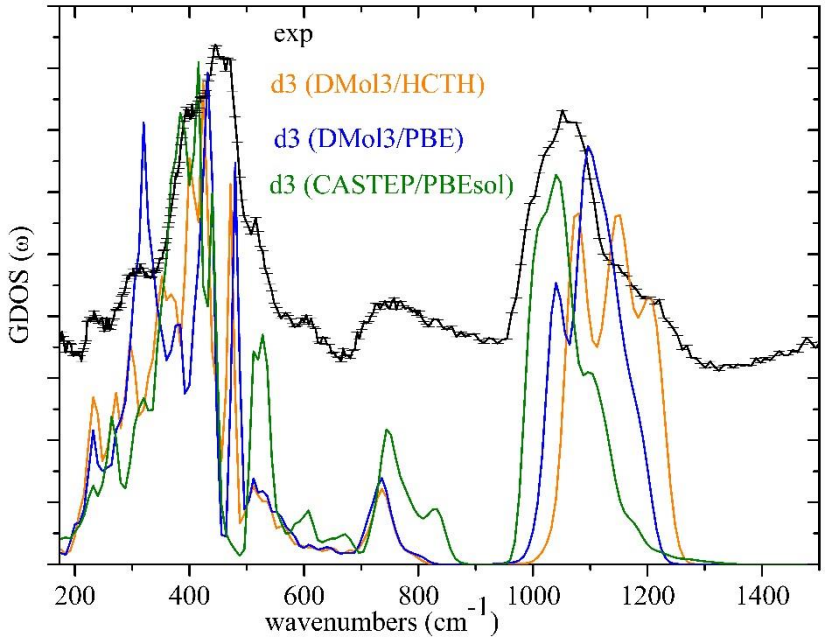

Figure 50. Comparison between the experimental INS spectrum of LTA-5 and fundamental vibrations calculated with DMol3 (HCTH, PBE and PBEsol functionals) for the model d3

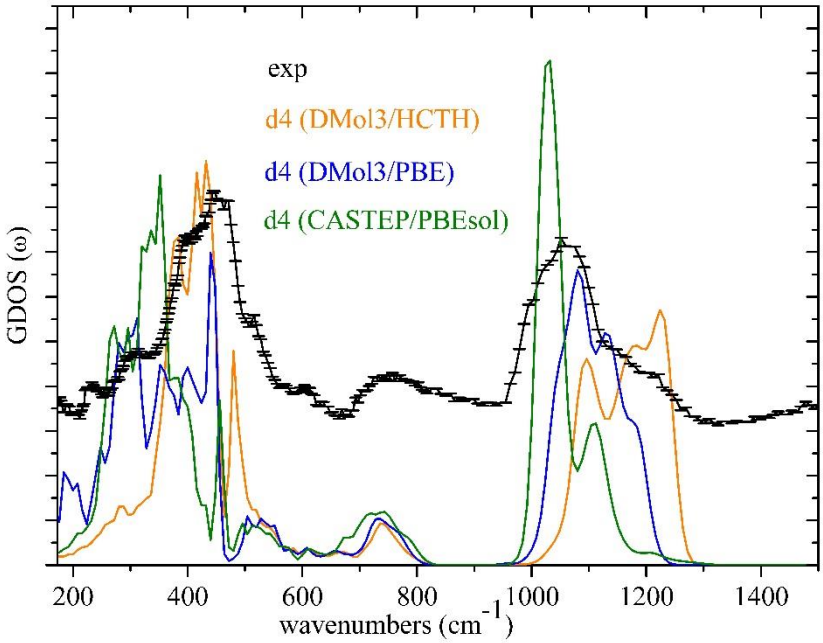

Figure 51. Comparison between the experimental INS spectrum of LTA-5 and fundamental vibrations calculated with DMol3 (HCTH, PBE and PBEsol functionals) for the model d4

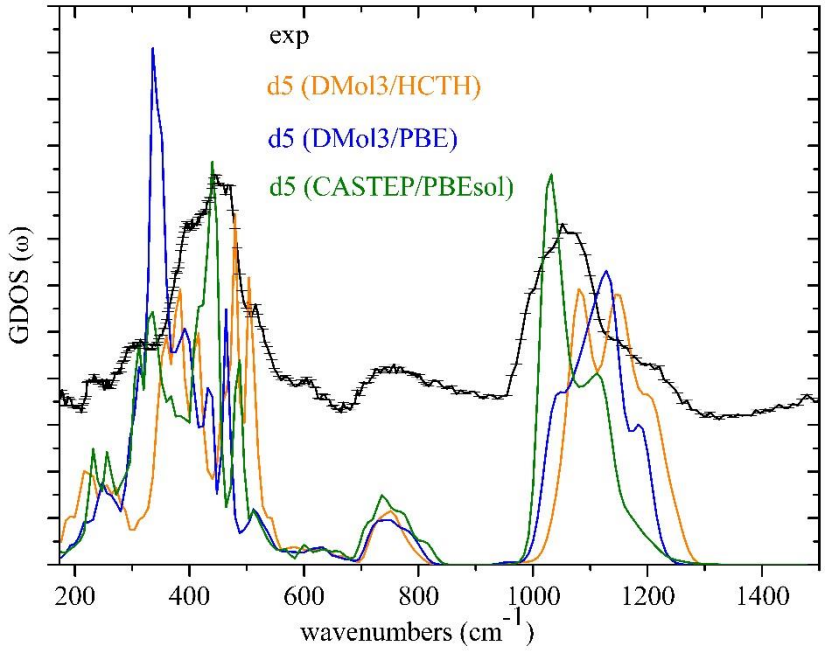

Figure 52. Comparison between the experimental INS spectrum of LTA-5 and fundamental vibrations calculated with DMol3 (HCTH, PBE and PBEsol functionals) for the model d5

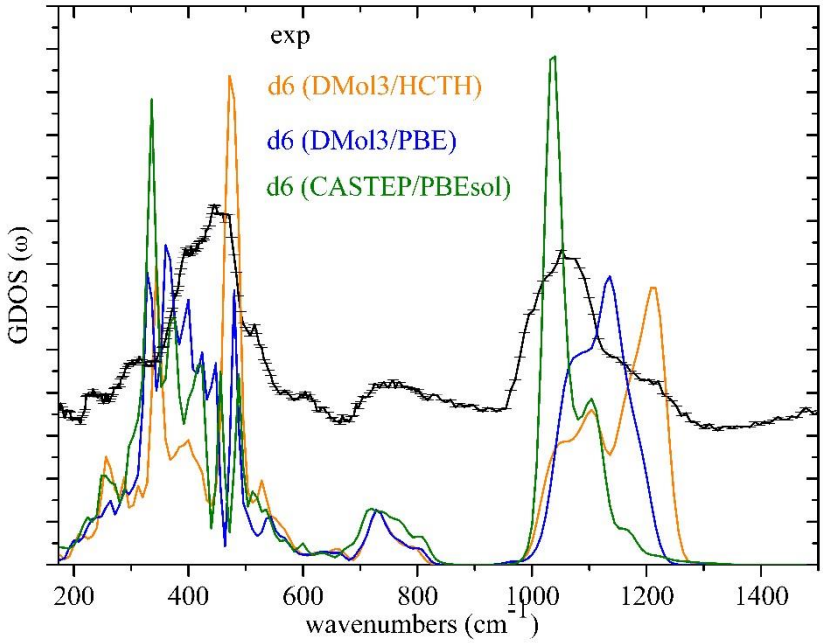

Figure 53. Comparison between the experimental INS spectrum of LTA-5 and fundamental vibrations calculated with DMol3 (HCTH, PBE and PBEsol functionals) for the model d6

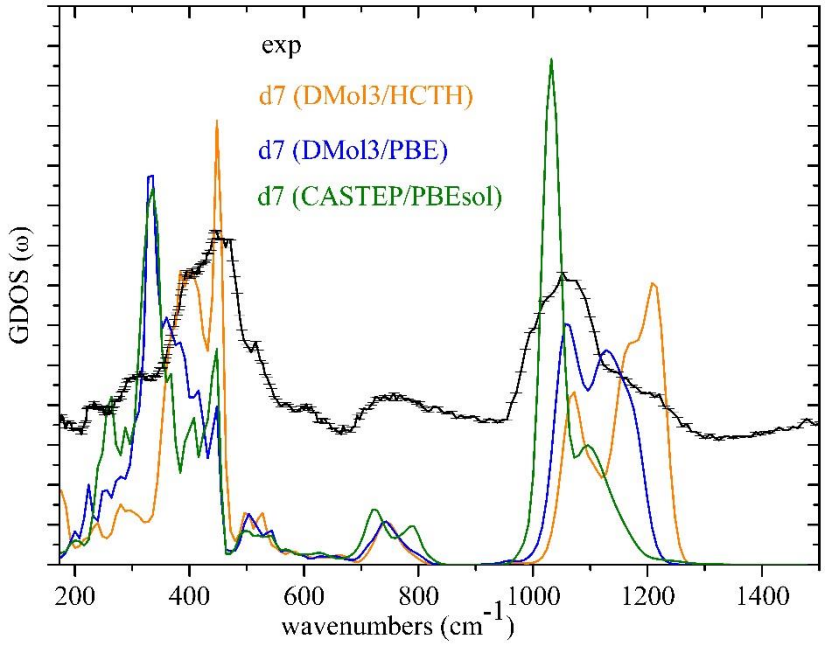

Figure 54. Comparison between the experimental INS spectrum of LTA-5 and fundamental vibrations calculated with DMol3 (HCTH, PBE and PBEsol functionals) for the model d7

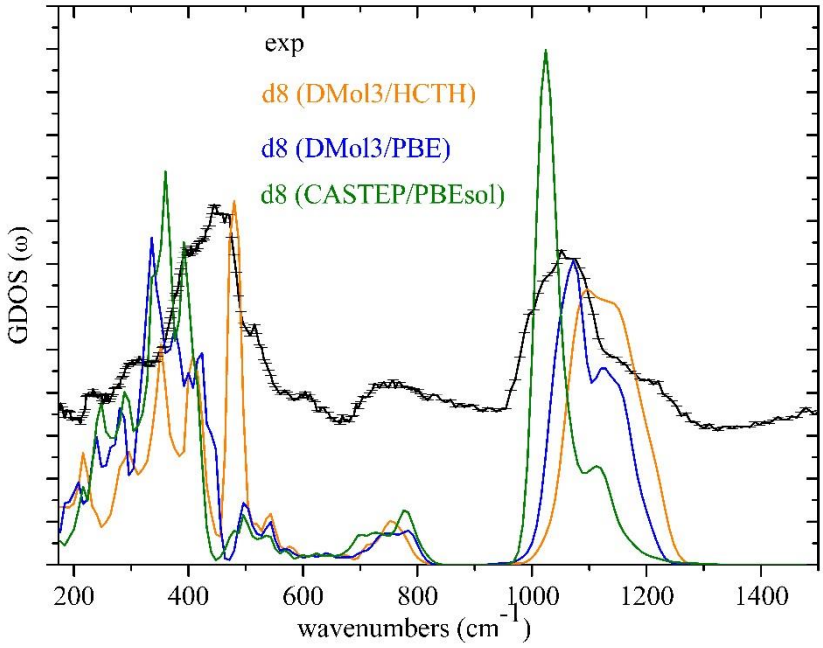

Figure 55. Comparison between the experimental INS spectrum of LTA-5 and fundamental vibrations calculated with DMol3 (HCTH, PBE and PBEsol functionals) for the model d8

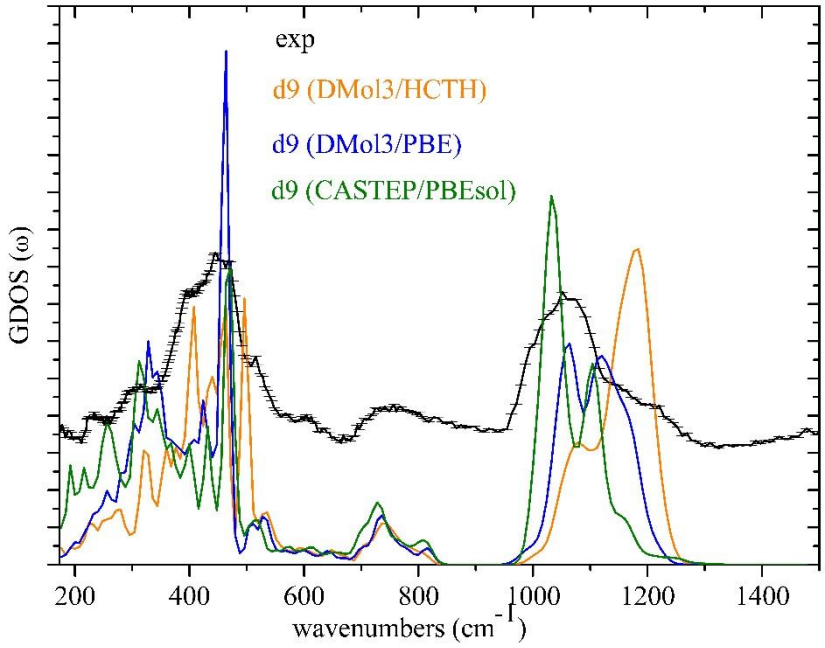

Figure 56. Comparison between the experimental INS spectrum of LTA-5 and fundamental vibrations calculated with Dmol3 (HCTH, PBE and PBEsol functionals) for the model d9

As it can be seen from **Figures 48-56**, in most of the cases results obtained by using DMol3/HCTH exchange-correlation functional are not in a good agreement with those obtained by DMol3/PBE. The best agreement between the results obtained by two different functional used in DMol3 have been observed for **d2** and **d3** models but the spectra attributed to **d2** model reproduce better experimental results among all models.

In consequence, we analyzed the geometry of the optimized structures of models **d1-d9** obtained by DMol3 with HCTH and PBE functionals, it has been found that the resulting structures contained significant distortions, we came to the conclusion that this is caused by the fact that DMol3 provides inefficient cell optimization procedure which consists in a set of parallel optimization processes requiring high computational cost. Therefore, DMol3 is efficient in studies of the systems which initial models have cell parameters

similar to experimental (such as LTA-40, which contain only ½ of a hydrogen atom per unit cell), in this case the calculations can be performed without cell optimization procedure. Hence, LTA-5 unit cell contains 4 hydrogen atoms, cell optimization procedure should be performed and results presented above can be considered as reliable enough to predict the model which describes better the experimental data.

Moreover, from **Figures 48-56** it can be seen that the spectra obtained by CASTEP/PBEsol are significantly different from those obtained by DMol3 calculations: according to CASTEP/PBEsol the model that better reproduces the experimental results is found to be **d5**, while the spectra calculated for this model by DMol3 are not in agreement with experimental INS spectrum. The reason of it is explained in the paragraph presented above.

From the results presented in this section, we can conclude that the calculated INS spectra are method-dependent, since the choice of the method not efficient for the system under a study leads to the unfeasible conclusions.

4.9 Conclusions of the Inelastic Neutron Scattering Study of the Aluminum and Brønsted Site Location in Aluminosilicate LTA Zeolites

In the present work, we propose a new general approach based on a combination of ^{29}Si NMR, INS, and DFT calculations that allows finding suitable distributions of aluminum and hydrogen in the Brønsted acid sites of zeolites with intermediate or high Si/Al ratios. The assignation of peaks to particular vibrations allows the establishment of rules that the probable distributions tend to fulfill such that intense peaks in the out-of-plane bending region (210−500 cm^{-1}) are due to protons vibrating without neighbor protons in the same ring. From a subset of nine unit cells with specific Al and H distributions that accurately reproduce the experimental ^{29}Si NMR spectrum of LTA-5, three distributions (labeled d5, **d3**, and **d1**), and in particular one of them (**d5**), reproduce an INS spectrum

that is almost identical to that calculated numerically using a procedure to compare spectra. Further, the specific peaks of the d5 distributions are very close to those of the experimental INS spectrum, and the corresponding features of the corresponding protons are chemically and structurally reasonably in terms of the zeolite properties. The extension of this approach to other zeolites is straightforward, although it will face the inherent complexity of zeolites containing a large number of nonequivalent T-sites. The estimation of the ^{29}Si NMR spectrum can be carried out in a reasonable amount of time, however the subsequent INS measurements will require certain amount of sample of high purity (~ 200 mg), which leads to difficulties in synthesis and difficulties in getting sufficient beamtime at the neutron facilities, since INS is not a standard laboratory experimental technique. In addition to that, the periodic DFT calculations of the selected Al distributions will be the lengthy part of the study.

Chapter 5

General conclusions

This thesis presents the results on characterization of Brønsted acid sites in LTA-40 and LTA-5 zeolites. For the study of this thesis we have selected one of the simplest zeolite topologies described in the literature, LTA, which contains only three possible crystallographic oxygen sites (assigned as O1, O2 and O3) and only one T site.

Characterization of zeolite acidity is typically performed by infrared (IR) and nuclear magnetic resonance (NMR) techniques, which allow to estimate the total number of acid sites and local environment of each of the Si atoms in the framework but do not allow to assign explicitly the location of each acid center. However, since these techniques give a very valuable information, they have been used in the present study as complementary techniques in combination with INS.

Prior to this study the proton locations in zeolite samples have only been found in several particular cases. First, it was suggested that in zeolites containing two types of cavities, infrared spectroscopy gives two distinct OH-stretching bands, at higher frequency for protons vibrating in large cavities, and at lower frequency for protons vibrating in small cavities [30]. However, further studies showed that this correlation is not followed in general [31]. ^{29}Si NMR spectroscopy is able to define the approximate abundance of aluminium atoms distributed as Si(nAl) with n=0-4, but it does not allow to find the location of aluminium or hydrogen atoms. Thus, until the present moment, finding the

distribution of aluminum atoms and protons in a zeolitic framework remains a challenging task.

The location of each of the acid sites and, hence, their local environment in the micropores of zeolite is one of the mayor features that define the overall catalytic activity of a given zeolite. The location of the acid sites in zeolites can be characterized by analyzing the OH-stretching and Si(or Al)OH bending modes, since differences in local environment of each of the hydrogen atoms result in variation of frequencies at which OH-stretching and bending bands appear in the spectra. Prior to this moment it has been shown that bending modes are more sensitive to the structure and composition (and, hence, location of the acid sites) of the zeolites than the stretching modes [57]. However, bending modes cannot be directly measured by IR, due to the fact that the spectral region where these modes are situated is dominated by intense vibrations of the zeolitic framework [54-56]. In this study we applied INS in order to measure the bending modes appearing in LTA with different Si/Al ratio.

Besides, in this thesis it was shown that the combination of a high quality of zeolite sample, and high sensitivity of the instrument together with periodic DFT calculations allows for the first time to detect with high precision the acid sites of LTA Si/Al = 40 and obtain information about their position. It has been found that the most probable location of the Brønsted acid sites in our LTA-40 sample is O2H. From previous studies [59] it was known that the peak found at 420 cm^{-1} corresponds to the SiOHAl out-of-plane bending mode in zeolites. In our study of LTA-40 it was found that this peak appears at 415 cm^{-1} in the calculations, and at 429 cm^{-1} in the experimental spectrum, hence, in very good agreement. However, none of the previous INS studies gave an assignment to a peak at 360 cm^{-1}. In this study we obtained from the calculations a peak at 360 cm^{-1} (373 cm^{-1} in the experimental spectrum) which we assign to framework vibrations plus out-of-plane SiOHAl bending. Moreover, in literature [60] the in-plane SiOH bending in HY zeolite (faujasite) was detected at 1052 cm^{-1} and in our calculated

LTA_47_O2H spectrum we obtain an intense peak corresponding to the in-plane SiOH bending at 1084 cm^{-1}. At the same time this peak appears at 1083 cm^{-1} in the experimental INS spectrum measured for sample of LTA-40.

Furthermore, we propose a new general approach based on a combination of INS, ^{29}Si NMR, INS and periodic DFT calculations that allows to define the distributions of aluminum and hydrogen in the Brønsted acid sites in zeolites with intermediate or high Si/Al ratios. We generated 9 models of LTA-5 with distributions of aluminium atoms compatible with ^{29}Si NMR data and, then compared the experimental INS spectrum with calculated spectra. We found the most probable distribution of aluminium atoms and acid sites corresponding to the model with calculated spectrum that better reproduces the experimental results.

In general, INS does not give the answer whether protons are located in large or small cavity. However, in case of LTA-40, O2H position that was found to be the most favorable corresponds to the protons vibrating in the small cavity. In case of LTA-5 we obtain the most probable distribution of aluminium and hydrogen atoms within the zeolitic framework, these protons may vibrate either in 6T or 8T rings. We believe there are no specific spectral features that allow to differentiate (by intensity or frequency) if a given peak belongs to a proton vibrating (SiOH out-of-plane bending) in either 6T-ring or 8T-ring.

We cannot consider the energies of models used in the study of LTA-5 as a significant criterion in estimating the relative stabilities of the models, since the obtained values are very similar. This is a direct consequence of having forced the Al distributions to match the Q_n distributions of the experimental ^{29}Si NMR spectrum of the LTA-5 sample and, therefore, geometric restrictions can be considered as more feasible criteria, since it is known that the presence of aluminum atoms located close to each other in zeolitic framework reduces the stability of the structure due to the electrostatic interactions.

Moreover, we got one or two optimum Al distributions which reproduce the INS spectrum of LTA-5 with good accuracy, as a consequence of the elimination of somehow unlikely Al distributions. This results in a precise solution that answers with full accuracy the question about the Al distribution of LTA-5. Unlike other studies in the literature, we give CIF file(s) with the fully detailed Al distribution.

The extension of the approach presented in this thesis can be applied straightforwardly to other zeolites of any Al content. However, we should note that the zeolite considered in this study LTA contains only on T crystallographic position, while in case of zeolites whose frameworks contain nonequivalent T-positions this procedure would face several difficulties. The study of such zeolites would require the consideration of a large number of models, since the number of possible suitable arrangements of Al and H also increases. At such conditions, the estimation of the ^{29}Si NMR spectrum can be carried out in a reasonable amount of time, however the subsequent INS measurements will lead to difficulties and periodic DFT calculations of the selected Al distributions may become a considerable computational hurdle.

Bibliography

[1] Cronstedt, A. F. “Natural zeolite and minerals,” Svenska Vetenskaps Akademiens Handlingar Stockholm. 1756, 17, 120.

[2] Colella, C.; Gualtieri, A.F. Cronstedt’s zeolite. Microporous Mesoporous Mater., 2007, 105, 213-221.

[3] Baerlocher, C.; Meier, W.M.; Olson, D. H.; Atlas of Zeolite Framework Types (formerly Atlas of Zeolite Structure Types), Elsevier, Amsterdam (2001).

[4] http://www.iza-structure.org/databases

[5] St. Claire-Deville, H.; Reproduction de la levyne. Comptes Rendus, 1862, 54, 324–327.

[6] Jackson, D.D.; Wegmann, E.; Bartow, E. Water softening by filtration through artificial zeolite. Journal (American Water Works Association), 1916, 3, No. 2, 423-433.

[7] DeSilva, F.J., Essentials of Ion Exchange. 25th Annual WQA Conference March 17, 1999

[8] Gottardi, G., Mineralogy and crystal chemistry of zeolites, in Natural Zeolites, Occurrence, Properties, Use, edited by L. B. Sand and F. A. Mumpton, pp. 31–44, Pergamon, New York, 1976

[9] Scott, J.; Guang, D.; Naeramitmarnsuk, K.; Thabuot, M.; Amal, R. Zeolite synthesis from coal fly ash for the removal of lead ions from aqueous solution. J. Chem. Technol. Biotechnol., 2001, 77, 63–69.

[10] Querol, X.; Alastuey, A.; Moreno, N.; Alvarez, A.E.; Garcia-Sanchez, A.; Cam, J.; Ayora, C.; Simon, M. Immobilization of heavy metals in polluted soils by the addition of zeolitic material synthesized from coal fly ash. Chemosphere., 2006, 62, 171–180.

[11] Barrer, R.M. Separating Hydrocarbons. 1942, US Patent 2306610.

[12] Barrer, R.M. Separating hydrocarbons. 1942, British Patent 548905.

[13] Masters, A. F.; Maschmayer, T. Zeolites – From curiosity to cornerstone. Microporous and Mesoporous materials, 2011, 142, 423-438.

[14] Karmen Margeta, Nataša Zabukovec Logar, Mario Šiljeg and Anamarija Farkas (2013). Natural Zeolites in Water Treatment – How Effective is Their Use, Water Treatment, Dr. Walid Elshorbagy (Ed.), InTech, DOI: 10.5772/50738. Available from: https://www.intechopen.com/books/water-treatment/natural-zeolites-in-water-treatment-how-effective-is-their-use

[15] Ackley, M. W.; Rege, S.U.; Saxena, H. Application of natural zeolites in the purification and separation of gases. Microporous and Mesoporous Materials. Microporous and Mesoporous Materials, 2003, 61, 25–42.

[16] Jia, W.; Murad, S. Separation of gas mixtures using a range of zeolite membranes: A molecular-dynamics study. The Journal of Chemical Physics, 2005, 122, 234708.

[17] Applebaum, S. B. Characteristic properties of zeolites for water softening. Journal (American Water Works Association), 1925, 13, 213-220.

[18] Cleaning Up with Chemistry: Investigating the Action of Zeolite in Laundry Detergent J. Chem. Educ., 1999, 76 (10), 1416A.

[19] Frederick, A. M. La roca magica: Uses of natural zeolites in agriculture and industry. PNAS, 1999, 96 (7), 3463-3470.

[20] Johan, E.; Yamada, T.; Munthali, M. W.; Kabwadza-Corner, P.; Aono, H.; Matsue, N. Natural Zeolites as Potential Materials for Decontamination of Radioactive Cesium. Procedia Environmental Sciences, 2015, 28, 52-56.

[21] Sharikova, L.K.; Pluzhnikova, M.f.; Tsybulevskii, A.M. Mechanism of catalytic cracking of hydrocarbons on zeolites. Petrol. Chem. U.S.S.R, 1980, 20, 45-54.

[22] Beecher, R.; Voories, A. Hexane isomerization over a zeolite catalyst. I & E C product research and development, 1969, 8, 366-371.

[23] Wei, J.; Ge, Q.; Yao, R.; Wen, Z.; Fang, C.; Guo, L.; Xu, H.; Sun, J. Directly converting CO_2 into a gasoline fuel. Nature Communications, 2017, 8, 15174

[24] Primo, A.; Garcia, H. Zeolites as catalysts in oil refining. Chem. Soc. Rev., 2014, 43, 7548.

[25] Kazansky, V. B. Adsorbed carbocations as transition states in heterogeneous acid catalyzed transformations of hydrocarbons. Catalysis Today, 1999, 51, 419-434.

[26] Verboekend, D; Liao, Y.; Schutyser, W.; Sels, B.F. Alkylphenols to phenol and olefins by zeolite catalysis: a pathway to valorize raw and fossilized lignocellulose. Green Chem., 2016, 18**,** 297-306.

[27] Gerzeliev, I. M.; Myachin, S. I.; Tasueva, I. D.; Khadzhiev, S. N. Synthesis of ethylbenzene on zeolite catalysts. Petroleum Chemistry, 2009, 49, No 1, 59.

[28] Liu, G.; Wu, J.; Luo, H. Ammoximation of Cyclohexanone to Cyclohexanone Oxime Catalyzed by Titanium Silicalite-1 Zeolite in Three-phase System. Chinese Journal of Chemical Engineering, 2012, 20 (5), 889–894.

[29] Starokon, V. E.; Parfenov, M. P.; Pirutko, L. V.; Soshnikov, I. E.; Panov, G. I. Epoxidation of ethylene by anion radicals of α-oxygen on the surface of FeZSM-5 zeolite. J. Catal., 2014, 309, 453-459.

[30] Jacobs, P. A.; Mortier, W. J. An Attempt to Rationalize Stretching Frequencies of Lattice Hydroxyl Groups in Hydrogen-Zeolites. Zeolites, 1982, 2 (3), 226–230.

[31] Lewis, D. W.; Sastre, G. Rationalisation of the IR Stretching Frequencies of Bronsted Acid Centres in Microporous Solids. Chem. Commun., 1999, 4, 349–350.

[32] Jacobs, P.A.; Uytterhoeven, J.B. Assignment of the Hydroxyl Bands in the Infrared Spectra of Zeolites X and Y. J. Chem. Soc., Faraday Trans. 1**,** 1973, 69, 359-372.

[33] Sierka, M.; Eichler, U.; Datka, J.; Sauer, J. Heterogeneity of Bronsted Acidic Sites in Faujasite Type Zeolites due to Aluminum Content and Framework Structure. J. Phys. Chem. B, 1998, 102, 6397–6404.

[34] Brunner, E. ^{1}H MAS NMR investigations on the proton distribution in H-Y zeolites. Elsevier Science Publishers B.V. Microporous Materials, 1993, 1, 431-435.

[35] Lippmaa, E.; Maegi, M.; Samoson, A.; Engelhardt, G.; Grimmer, A.R. Structural studies of silicates by solid-state high-resolution silicon-29 NMR J. Am. Chem. Soc., 1980, 102, 4889.

[36] Klinowski, J.; Ramdas, S.; Thomas, J. M.; Fyfe, C. A.; Hartmann, J. S. High resolution ^{29}Si NMR, of dealuminated Y-zeolites. J. Chem. Soc., Farad. Trans., 1983, 78, 1025.

[37] Sastre, G.; Katada, N.; Niwa, M. Computational Study of Bronsted Acidity of Mordenite. Effect of the Electric Field on the Infrared OH Stretching Frequencies. J. Phys. Chem. C, 2010, 114 (36), 15424–15431.

[38] O'Malley, P.J.; Dwyer, J. An ab Initio Quantum Chemical Investigation on the Effect of the Magnitude of the T-O-T Angle on the Brønsted Acid Characteristics of Zeolites. J. Phys. Chem., 1988, 92, 3005-3007.

[39] Tamele, M. W.; Chemistry of the surface and the cracking catalyst activity of alumina-silica. Discuss Faraday Soc., 1950, 8, 270.

[40] Walling, C. The Acid Strength of Surfaces. J. Am. Chem. Soc., 1950, 72, 3, 1164-1168.

[41] Corma, A. Inorganic Solid Acids and Their Use in Acid-Catalyzed Hydrocarbon Reactions. Chem. Rev., 1995, 95 (3), 559–614.

[42] Hunger, B.; Heuchel, M.; Clark, L. A.; Snurr, R. Q. Characterization of Acidic OH Groups in Zeolites of Different Types: An Interpretation of NH_3-TPD Results in the Light of Confinement Effects. J. Phys. Chem. B, 2002, 106 (15), 3882–3889.

[43] Brändle, M.; Sauer, J. Acidity Differences between Inorganic Solids Induced by Their Framework Structure. A Combined Quantum Mechanics/Molecular Mechanics ab Initio Study on Zeolites J. Am. Chem. Soc., 1998, 120, 1556–1570.

[44] Lee, C.; Parrillo, D. J.; Gorte, R. J.; Farneth, W. E. Relationship between Differential Heats of Adsorption and Brønsted Acid Strengths of Acidic Zeolites: H-ZSM-5 and H-Mordenite. J. Am. Chem. Soc., 1996, 118 (13), 3262–3268.

[45] Mitani, Y.; Tsutsumi, K.; Takahashi, H. Direct Measurement of the Interaction Energy between Solids and Gases. X. Acidic Properties of Hydroxyl Sites of H–Y Zeolite Determined by High-temperature Calorimetry. Bull Chern Soc Jpn, 1983, 56, 1917.

[46] Simperler, A.; Bell, R.G.; Foster, M. D.; Gray, A.E.; Lewis, D.W.; Anderson, M. W. Probing the Acid Strength of Brønsted Acidic Zeolites with Acetonitrile: An Atomistic and Quantum Chemical Study. J. Phys. Chem. B, 2004, 108 (22), 7152-7161.

[47] Sauer, J. Brønsted activity of two-dimensional zeolites compared to bulk materials. Faraday Discuss., 2016, 188, 227-234.

[48] Senchenya, I. N.; Garrone, E.; Ugliengo, P.; An ab initio study of terminal SiOH and bridging Si(OH)Al groups in zeolites and their interaction with carbon monoxide. Journal of molecular structure (Theochem), 1996, 368, 93-110.

[49] Datka, J.; Geerlings, P.; Mortier, W.; Jacobs, P. Influence of the Overall Composition on Zeolite Properties. 1. The Framework: An Infrared Spectroscopic and Quantum Chemical Study. J. Phys. Chem., 1985, 89, 3483-3488.

[50] Datka, J.; Broclawik, E.; Gil, B. IR Spectroscopic Studies and Quantum Chemical Calculations Concerning the O-H Dissociation Energies in Zeolites NaHX and NaHY. J. Phys. Chem. 1994, 98, 5622-6626.

[51] Grajciar, L.; Arean, C. O.; Pulido, A.; Nachtigal, P. Periodic DFT investigation of the effect of aluminium content on the properties of the acid zeolite H-FER. Phys. Chem. Chem. Phys., 2010, 12, 1497–1506.

[52] Datka, J.; Gil, B.; Kubacka, A. Acid properties of NaH-mordenites: Infrared spectroscopic studies of ammonia sorption. Zeolites, 1995, 15, 501-506.

[53] Campbell, B. J.; Cheetham, A. K.; Vogt, T.; Carluccio, L.; Parker, W. O.; Flego, C.; Millini, R. The determination of Brønsted acid sites in zeolite ERS-7 by neutron and X-ray powder diffraction. J. Phys. Chem. B, 2001, 105, 1947-1955.

[54] Flanigen, E. M.; Khatami, H.; Szymanski, A. Infrared Structural Studies of Zeolite Frameworks. A. Adv. Chem. Ser. 101, Am. Chem. Soc. Washington, DC, 201, 1971.

[55] Flanigen, E. M. Structural analysis by Infrared spectroscopy in J. A. Rabo. Zeolite Chemistry and Catalysis, ACS Monograph 171, Am. Chem. Soc. Washington, DC, 1976, 80.

[56] van Santen, R. A.; Vogel, D. L. Lattice dynamics of zeolites. Adv. Solid-state Chem., 1989, 1, 151-224.

[57] Kustov, L.M.; Borokov, V. Yu.; Kazansky, V.B. Spectra of Hydroxyl Groups in Zeolites in the Near-Infrared Region. J. Catal., 1981, 72, 149.

[58] Wax, M. J.; Cavanagh, R. R.; Rush, J. J.; Stucky, G. D.; Abrams, L.; Corbin, D. R. A Neutron Scatterlng Study of Zeolite Rho. J. Phys. Chem., 1986, 90, 532−534.

[59] Sauer, J. Acidic sites in heterogeneous catalysis: structure, properties and activity. J. Mol. Catal., 1989, 54, 312-323.

[60] Jacobs, W. P. J. H.; Jobic, H.; van Wolput, J. H. M. C.; van Santen, R.A. Fourier transform infrared and inelastic neutron scattering study of HY zeolites. Zeolites, 1992, 12, 315-319.

[61] Jacobs, W. P. J. H.; Jobic, H.; van Wolput, J. H. M. C.; van Santen, R.A. A vibrational study of the OH and OD bending modes of the Brønsted acid sites in zeolite. Zeolites, 1994, 14, 117-125.

[62] Jobic, H. Observation of the Fundamental Bending Vibrations of Hydroxyl Groups in HNa-Y Zeolite by Neutron Inelastic Scattering. J. Catal., 1991, 131, 289-293.

[63] Jobic, H.; Smirnov K.S.; Bougeard, D.; Inelastic neutron scattering spectra of zeolite frameworks – experiment and modeling. Chem. Phys. Lett., 2001, 344, 147-153.

[64] Chadwick, J. The Existence of a Neutron. Proc. R. Soc. Lond. A, 1932, 136, 692-708.

[65] Weinstock, R. Inelastic Scattering of Slow Neutrons. Phys. Rev., 1944, 65, 1.

[66] https://www.nobelprize.org/nobel_prizes/physics/laureates/1994/

[67] https://www.nist.gov/ncnr

[68] Miller, Jr., George Tyler (2002). Living in the Environment: Principles, Connections, and Solutions (12th Edition). Belmont: The Thomson Corporation. p. 345. ISBN 0-534-37697-5.

[69] https://intranet.ill.eu/

[70] Squires, G. L. Introduction to the Theory of Thermal Neutron Scattering. Cambridge University Press, Cambridge, 2012.

[71] Schober, H. An introduction to the theory of nuclear neutron scattering in condensed matter. J. Neutron Res., 2014, 17, 109–357.

[72] P. C. H. Mitchell, S. F. Parker, A. J. Ramirez-Cuesta, John Tomkinson. Vibrational Spectroscopy with Neutrons With Applications in Chemistry, Biology, Materials Science and Catalysis. World Scientific Publishing Co. Pte. Ltd., Singapore, 2005.

[73] Neutron Scattering: A Primer, by Roger Pynn taken from: http://www.lansce.lanl.gov

[74] Shirane G., Shapiro S. M. and Tranquada J. M 2002 Neutron Scattering with a Triple-Axis Spectrometer, (Cambridge: Cambridge University Press).

[75] http://www.ill.eu/

[76] Jiménez-Ruiz, M.; Ivanov, A. LAGRANGE - the new neutron vibrational spectrometer at the ILL. J. Phys.: Conf. Ser., 2014, 549, 1742-6596.

[77] Parker, S. F.; Ramirez-Cuesta, A. J.; Albers, P. W.; Lennon, D. The use of direct geometry spectrometers in molecular spectroscopy. J. Phys.: Conf. Ser., 2014, 554, 1742-6596.

[78] Lipkin, H. "Physics of Debye-Waller Factors", Cornell University Library, 2004.

[79] Crowell, B. "4. Force and Motion". Newtonian Physics. ISBN 0-9704670-1-X. Archived from the original on 16 February 2007.

[80] Moore, W. J., Physical Chemistry, 4th Ed., Printice-Hall: Englewood Cliffs, NJ, 1972, Chapter 17, Sec. 14., pp 775-776.

[81] Wilson, Jr., E. B.; Decius, J. C.; Cross, P. C., Molecular vibrations; the theory of infrared and Raman vibrational spectra, McGraw-Hill, New York, 1955.

[82] Zielinski, T.; Harvey, E.; Sweeney, R.; Hanson, D. Quantum States of Atoms and Molecules. J. Chem. Educ., 2005, 82 (12), 1880.

[83] Capelle, K.; A bird's-eye view of density-functional theory, https://arxiv.org/abs/cond-mat/0211443

[84] Hohenberg, P.; Kohn, W. Inhomogeneous Electron Gas. Phys. Rev.. 1964, B 136, 864.

[85] Kohn, W; Sham, L. J.; Self-Consistent Equations Including Exchange and Correlation Effects. Phys. Rev. 1965, 140, A1133.

[86] Vosko, S. J.; Wilk, L.; Nusair, M. Accurate spin-dependent electron liquid correlation energies for local spin density calculations: a critical analysis**.** Can. J. Phys., 1980, 58, 1200.

[87] Perdew, J. P.; Burke, K; Ernzerhof, M. Generalized Gradient Approximation Made Simple. Phys. Rev. Lett., 1996, 77, 3865.

[88] Perdew, J. P.; Burke, K; Ernzerhof, M. Generalized Gradient Approximation Made Simple. Phys. Rev. Lett. 1997, 78, 1396(Erratum).

[89] Burke research group http://dft.uci.edu/research.php

[90] Perdew, J.; Ruzsinszky, A.; Csonka, G. I.; Vydrov, O. A.; Scuseria, G. E.; Constantin, L. A.; Zhou, X.; Burke, K.; Restoring the Density-Gradient Expansion for Exchange in Solids and Surfaces; Phys. Rev. Lett., 2008, 100, 136406.

[91] Tkatchenko, A.; Scheffler, M. Accurate Molecular Van Der Waals Interactions from Ground-State Electron Density and Free-Atom Reference Data. Phys. Rev. Lett., 2009, 102, 073005.

[92] Al-Saidi, W. A.; Voora, V. K.; Jordan, K. D. An Assessment of the vdW-TS Method for Extended Systems. J. Chem. Theory Comput., 2012, 8, 1503-1513.

[93] Fischer, M.; Angel, R. J. Accurate structures and energetics of neutral-framework zeotypes from dispersion-corrected DFT calculations. J. Chem. Phys., 2017, 146, 174111.

[94] Boese, D. A; Handy, N. C. A new parametrization of exchange-correlation generalized gradient approximation functionals. J. Chem. Phys., 2001, 114 (13), 5497-5503

[95] Curtiss, A. L.; Ragavachari, K.; Trucks, G.W.; Pople, J. A. Gaussian-2 theory for molecular energies of first- and second-row compounds. J. Chem. Phys., 1991, 94, 7221.

[96] Becke, A. D. Density-functional exchange-energy approximation with correct asymptotic behavior. Phys. Rev. A, 1988, 38, 3098.

[97] Materials Studio 6.1. Dassault Systèmes BIOVIA, San Diego 2018.

[98] Delley, B. From molecules to solids with the DMol3 approach. J. Chem. Phys, 2000, 113, 7756.

[99] Clark, S. J.; Segall, M. D.; Pickard, C. J.; Hasnip, P. J.; Probert, M. J.; Refson, K.; Payne, M. C. First principles methods using CASTEP. Z. Kristallogr. 2005, 220, 567-570.

[100] Kleinman, L.; Bylander, D. M. Efficacious form for model pseudopotentials. Phys, Rev. Lett., 1982, 48, 1425-1428.

[101] Vanderbilt, D. Soft self-consistent pseudopotentials in generalized eigenvalue formalism. Phys. Rev., 1990, B41, 7892-7895.

[102] http://dx.doi.org/10.5286/software/mantid

[103] Ramirez-Cuesta, A.J.; aCLIMAX 4. 0. 1., The new version of the software for analyzing and interpreting INS spectra. Computer Physics Communications, 2004, 157, 226-238.

[104] Kearley, G. J.; Tomkinson, J.; Penfold, J. New Constraints for Normal-Mode Analysis of Inelastic Neutron-Scattering Spectra: Application to the HF_2^-. Z. Phys. B - Condensed Matter, 1987, 69, 63-67.

[105] Sprawls, P. "Chapter 3: Nuclear Magnetic Resonance". Magnetic Resonance Imagine. Principles, Methods, and Techniques. Perry Sprawls. Online edition provided with open access by: http://www.sprawls.org

[106] NMR Periodic Table (http://triton.iqfr.csic.es)

[107] Keeler, J. "Chapter 2: NMR and energy levels" *(reprinted at* University of Cambridge*)*. Understanding NMR Spectroscopy. University of California, Irvine. Retrieved 2007-05-11.

[108] Hennel, J.W.; Klinowski, J. (2005). "Magic Angle Spinning: A Historical Perspective". In Jacek Klinowski. New techniques in solid-state NMR. Springer. pp. 1–14. doi*:*10.1007/b98646. ISBN 3-540-22168-9. (New techniques in solid-state NMR, p. 1, at Google Books).

[109] Leary G.J., Newman R.H. (1992) Cross Polarization/Magic Angle Spinning Nuclear Magnetic Resonance (CP/MAS NMR) Spectroscopy. In: Lin S.Y., Dence C.W. (eds) Methods in Lignin Chemistry. Springer Series in Wood Science. Springer, Berlin, Heidelberg

[110] Vidal-Moya, A.; Blasco, T.; Rey, F.; Valencia, S.; Corma, A. Characterization of LTA type zeolites with different Si/Al ratio. Poster session presented at: 16th International Zeolite Conference joint with the 7th International Mesostructured Materials Symposium. 2010 Jul 4-9; Sorrento, Italy

[111] Massiot, D.; Fayon, F.; Capron, M.; King, I.; Le Calvé, S.; Alonso, B.; Durand, J. O.; Bujoli, B.; Gan, Z.; Hoatson, G. Modelling one- and two-dimensional solid state NMR spectra. Magn. Reson. Chem., 2002, 40, 70-76.

[112] Lemishko, T.; Valencia, S.; Rey, F.; Jiménez-Ruiz, M.; Sastre, G. Inelastic Neutron Scattering Study on the Location of Brønsted Acid Sites in High Silica LTA Zeolite. J. Phys. Chem. C, 2016, 120 (43), 24904–24909.

[113] Moscoso, J. G.; Lewis, G. J.; Gisselquist, J. L.; Miller, M. A.; Rohde, L. M. UZM-16: a crystalline aluminosilicate zeolitic material. WO Patent 03/068679, 2003.

[114] Lemishko, T.; Jiménez-Ruiz, M.; Rey, F.; Blasco, T.; Vidal Moya, A.; Sastre, G. Inelastic Neutron Scattering Study of Aluminum and Brønsted Site Location in LTA-5 Zeolite. J. Phys. Chem. C, 2018, 122 (21), 11450–11454.

[115] https://www.ill.eu/users/support-labs-infrastructure/software-scientific-tools/lamp/

[116] Sastre, G.; Gale, J. D. ZeoTsites: A Code for Topological and Crystallographic Tetrahedral Sites Analysis in Zeolites and Zeotypes. Microporous Mesoporous Mater. 2001, 43, 27−40.

[117] Bermúdez, D.; Sastre, G. Calculation of Pore Diameters in Zeolites. Theor. Chem. Acc., 2017, 136, 116.

[118] Hoffman, A. E. J.; Vanduyfhuys, L.; Nevjestić, I.; Wieme, J.; Rogge, S. M. J.; Depauw, H.; Van Der Voort, P.; Vrielinck, H.; Van Speybroeck, V. Elucidating the Vibrational Fingerprint of the Flexible Metal-Organic Framework MIL-53(Al) Using a Combined Experimental/ Computational Approach. J. Phys. Chem. C, 2018, 122, 2734−2746.